UCRL-19004

cy. 2

FRACTURE TOUGHNESS OF PRECIPITATION HARDENING ALUMINUM ALLOYS

David Eugene Porter
(Ph. D. Thesis)

April 1969

AEC Contract No. W-7405-eng-48

LAWRENCE RADIATION LABORATORY
UNIVERSITY of CALIFORNIA BERKELEY

UCRL-19004

cy. 2

DISCLAIMER

TABLE OF CONTENTS

FRACTURE TOUGHNESS OF PRECIPITATION HARDENING ALUMINUM ALLOYS

David Eugene Porter

Inorganic Material Research Division, Lawrence Radiation Laboratory
Department of Materials Science and Engineering, College of Engineering
University of California, Berkeley, California

ABSTRACT

The mechanical properties of five high purity aluminum-zinc alloys (7 to 50% Zn) and four high purity aluminum-silver alloys (5 to 30% Ag) were investigated. Emphasis was placed on intergranular fracture. The properties were correlated with the microstructure and fractographic observations.

There were two basic intergranular fracture processes, a slow and a fast-crack growth process. Slow-crack growth occurred by microvoid coalescence, leaving a dull fracture surface. Fast-crack growth leaves a bright featureless surface. Of the alloys studied, only the aluminum-zinc alloys with 25% zinc or more in the maximum strength condition were found to fracture by a fast-crack growth process. Fast-crack growth was generally preceded by slow-crack growth. The latter process took place at lower stress intensity levels and if allowed to continue under a constant load it would lead to failure. Crack growth would continue under a constant load that was sufficient for initiation of the process as there was no mechanism to blunt the crack. The calculated value of the stress intensity factor for slow-crack growth, based on the energy dissipated in the plastic zone, was consistent with the measured value. Stress-wave emission records for the slow-crack growth process indicated that the process was discontinuous with the crack jumping along the grain-boundary from one grain-boundary node to another.

I. INTRODUCTION

Precipitation hardening aluminum alloys, such as Al-Zn, Al-Cu, and Al-Ag have a tendency to fail intergranularly under certain conditions.[1-5] Intergranular failure of these alloys generally occurs when they are aged to peak strength, thus limiting their utility. This mode of fracture is enhanced in corrosive environments; stress-corrosion cracking of aluminum alloys generally involves intergranular separation. Although there is a qualitative understanding of intergranular fracture the problem is not too well known quantitatively and this limits the development of better high strength aluminum alloys.* While binary aluminum alloys are not of commercial value they offer a basis for understanding of the fundamentals of the intergranular fracture process.

Many of the earlier investigations have been concerned with fracture at high temperatures where creep is important.[7-9] These investigations have fairly well characterized the macroscopic aspects of how intergranular cracks are formed and grow through grain-boundary sliding (see in particular the work of Chang and Grant[7]). Other investigations have been concerned with explaining room temperature intergranular fracture in terms of microstructure.[2-5,10,11] These investigations have characterized the microstructure by transmission electron microscopy and the slip behavior by surface replica studies. Intergranular fracture at ambient temperatures is generally attributed to either the existence of an embrittling layer of precipitate in the grain-boundary or a precipitate-free zone on either side of the grain-boundary.

In the solution treated condition and during the early stages of aging, the grains are softer than the grain-boundaries, because precipitation

*An understanding of important microstructural aspects of intergranular fracture has led to improved stress-corrosion properties of some aluminum alloys.[6]

starts first and advances more rapidly at the boundaries. In this condition, the grains deform in a more or less homogeneous manner and the fracture is generally transgranular. At peak strength, the grains have aged to maximum hardness but the grain-boundary regions are overaged. They contain coalesced precipitates and precipitate-free zones. In this state, plastic deformation is mainly accommodated by flow in the narrow soft region of the grain-boundary and the material fails along the weaker boundary layer. Further aging causes the grains to overage and soften to the extent that deformation becomes more homogeneous and transgranular failure again occurs. This simplified description serves to illustrate the nature of intergranular fracture in age hardening alloys.[10]

The microstructural aspects of intergranular fracture appear to be fairly well understood, although there has never been any extensive quantitative description of the process (excepting the case of stress-corrosion cracking). The concepts of fracture mechanics have been applied to a range of commerical high strength aluminum alloys, fracture toughness of these alloys is well documented[12-14] and correlated with the microscopic appearance of the fracture surfaces.[15] This has not been done for alloys exhibiting intergranular fracture.

The present investigation describes the fracture toughness of a number of aluminum-zinc and aluminum-silver alloys. These two binary systems were chosen for this investigation because they show well defined intergranular fracture over a wide range of heat treatments and strength levels. A second portion of this investigation correlates the fracture properties of these alloys with the metallography and fractography. The dynamics of crack growth were also investigated in order to determine whether the growth of an intergranular crack is continuous or discontinuous.

(One might expect that an intergranular crack would grow by a discontinuous process due to the change in crack direction at each grain intersection.)

The fracture toughness of aluminum alloys has been measured in several ways. The fracture mechanics approach, where the appropriate stress intensity factor is determined using a standard fracture specimen,[12-14] was used for this investigation.

II. EXPERIMENTAL PROCEDURE AND RESULTS

A. Materials

High purity alloys of aluminum zinc and aluminum silver were made from components of at least 99.99% purity. These alloys were melted in a baked out graphite crucible under a controlled atmosphere, then poured into a chilled copper mold. The aluminum-zinc alloys were melted under a slightly negative gage pressure of argon, while the aluminum silver alloys were melted under vacuum. The alloy ingots were homogenized for approximately 50 hours at 25 to 50°C below the solidus and hot rolled at 400°C to near final thickness. After hot rolling, the resulting strips were finish by cold rolling to the final thickness. Specimens were then cut with their tensile axis parallel to the rolling direction of the strips. The remaining material was used to chemical analysis. The analyses of the alloys are listed in Table 1. The numbers in the table will hereafter be used to identify the alloys.

B. Heat Treatments

The heat treating of all specimens was carried out in salt baths maintained at the required temperature. Aluminum-zinc alloys were solution treated for 60 min. at 425°C, quenched into ice water, and aged for the various times at 125°C. Aluminum-silver alloys were solution treated for 60 min at 525°C, quenched into ice water, and aged for various times at 225°C.

C. Mechanical Testing

1. Tensile Tests

Room temperature tensile tests were carried out to document the tensile properties of each alloy as a function of aging time, (called routine tensile tests in future discussions). These tests were made on the 1/2 in.

Table 1. Average Compostion and Chemical Analysis of Alloys Tested

Aluminum - Zinc Series

Melt. No.	%Zn	Atomic % Zn	%Cu	% Si	%Ca	%Cr	%Mn	%Fe	%C	$\%H_2$	$\%O_2$	%Al
22	6.83	2.9	0.002	< .01	0.002	0.001	0.003	0.2	0.0030	0.0035	0.060	Balance
23	12.86	5.8										
24	25.74	12.5										
25	36.84	19.4										
26	49.22	28.6	0.001	< .01				0.05	0.0060	0.0008	0.0065	

Aluminum - Silver Series

Melt. No	%Ag	Atomic % Ag	%Cu	%Si	%Ca	%Cr	%Mn	%Fe	%C	$\%H_2$	$\%O_2$	%Al
27	4.76	1.2	0.06	< 0.01				0.02	0.0045	0.0002	0.022	Balance
28	9.66	2.6										
29	20.11	5.9										
30	28.62	9.1		< 0.01		0.001		0.02	0.0080	0.001	0.032	

gage length specimen shown in Fig. 1(c). The specimens were nominally 1/16 in. thick. They were pulled at a strain rate of 0.39 in./in./min. Additional variables investigated were test temperature and strain rate.

2. Fracture Tests

Fracture tests corresponding to the routine tensile tests, were carried out using a single edge-notch or SEN fracture specimen. This SEN fracture specimen, shown in Fig. 1(b), was nominally 1/16 in. thick. Tests were made using a crosshead rate of 0.039 in/min. The stress intensity factor used for this specimen was that given by Katz et al.[16]

In addition to the routine tests, full instrumented fracture tests were carried out where more specific information was needed. These tests were made on nominally 1/8 in. thick material using the larger SEN specimen shown in Fig. 1(a). The stress intensity factor used in this case was given in by Srawley and Gross.[17]

All samples used in fracture testing were fatigue pre-cracked for a distance approximately equal to the specimen thickness. The fatigue pre-cracking was done by a tension-tension fatigue machine that was designed by the author. (This machine is to be described in a separate paper.)

The instrumentation for the large SEN specimens included a crack opening displacement (COD) gage to measure dynamic crack position and an accelerometer to measure stress-wave emission (SWE). The COD gage used was a double cantilever beam type gage[18] excited by a 2.7 V D.C. power supply. The output of this gage was fed into a strip chart recorder to obtain the gage movement with respect to time. Calibration of the gage was carried out by first plotting the gage displacement versus output to obtain the sensitivity. The gage was then placed on a specimen and the output

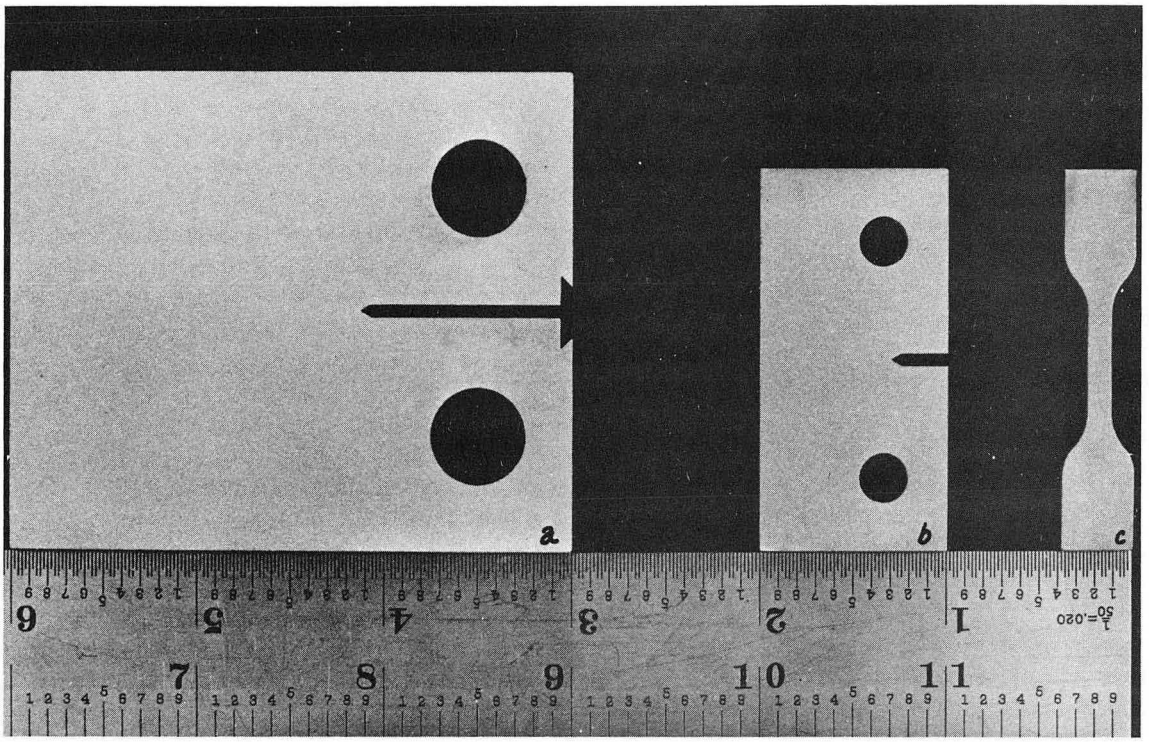

XBB 691-463

Fig. 1 Specimens used for mechanical tests.

(a) large fracture specimen used for instrumented tests.
(b) small fracture specimen used for routine testing.
(c) tensile specimen.

recorded as a function of load. Small loads were used to aviod plastic deformation at the tip of the crack. Gage output versus load curves for several different crack lengths were made. The ratio VBE/P versus a/w was plotted to complete the calibration, where

V = voltage

B = thickness in.

E = elastic modulus - psi

P = load - lbs

a = crack length - in.

w = specimen width - in.

Stress-wave emission studies were carried out using an Endevco calibrated accelerometer and charge amplifier. The amplifier output was filtered to eliminate mechanical and electrical noise, and then recorded on an oscillograph. Additional information on the SWE technique may be found in Refs. 19-21.

3. Results of Mechanical Tests

The results of an instrumented fracture tests of commerical 7079-T6 aluminum are given first to illustrate how a commerical material behaves. These results are shown in Figs. 2 and 3, and Table 2. In Fig. 3, and all similar figures, the vertical lines are timing lines that are 1 second apart. The numbers along side the timing lines at the top of the oscillogram refer to the approximate total number of seconds from the start of the tests. Once the time of an event is established, then the properties corresponding to the event can be found be referring to the appropriate figure or table. The first pop-in (No. 1) of Fig. 2 is a good example to illustrate the properties corresponding to an event. The pop-in occurred at 46.5 seconds. This corresponded to a stress wave in Fig. 3 which has saturated the recording system. The saturation condition

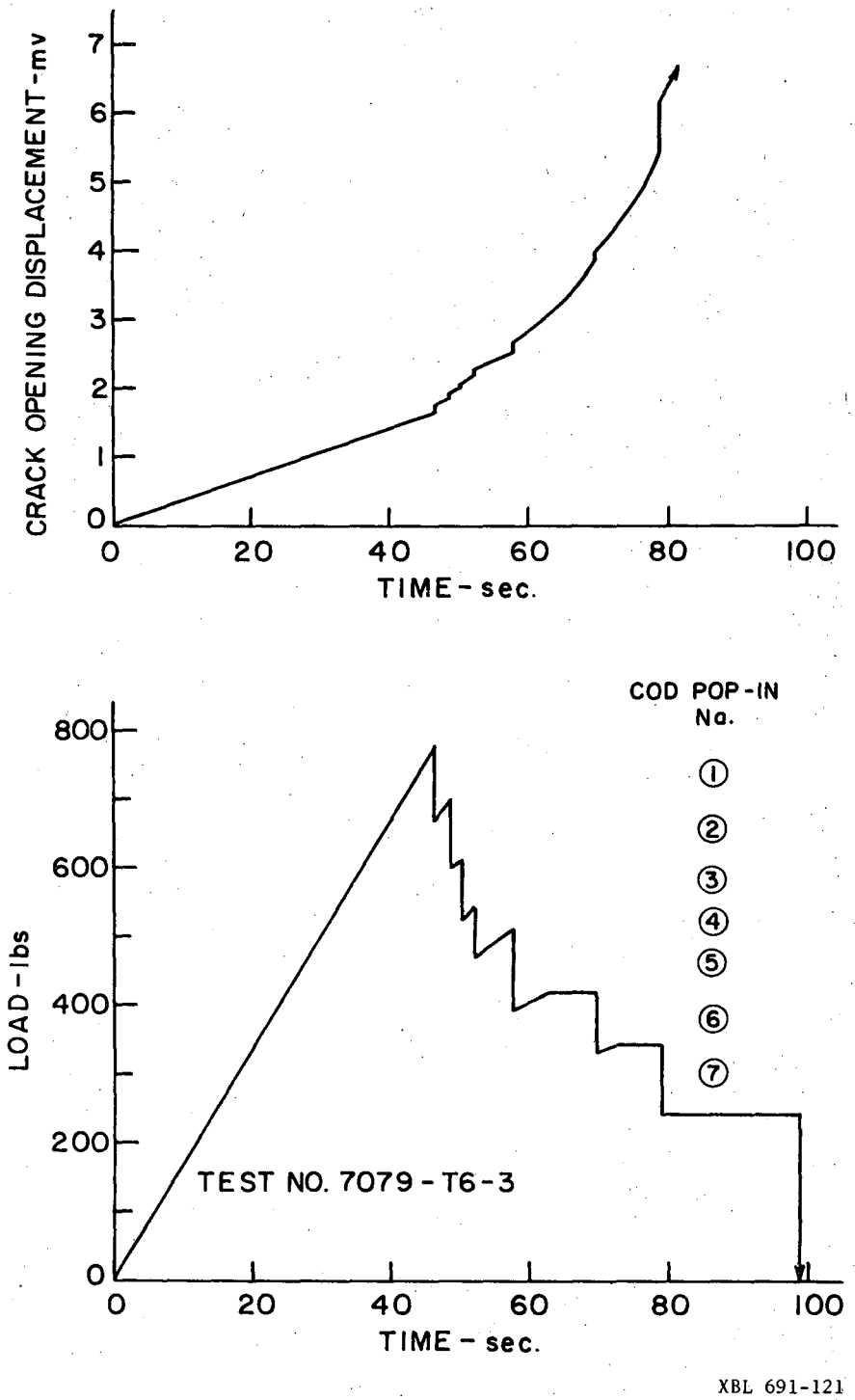

Fig. 2 The crack opening displacement gage output and load versus time records for .071 in. thick 7079-T6 aluminum large SEN fracture specimen.

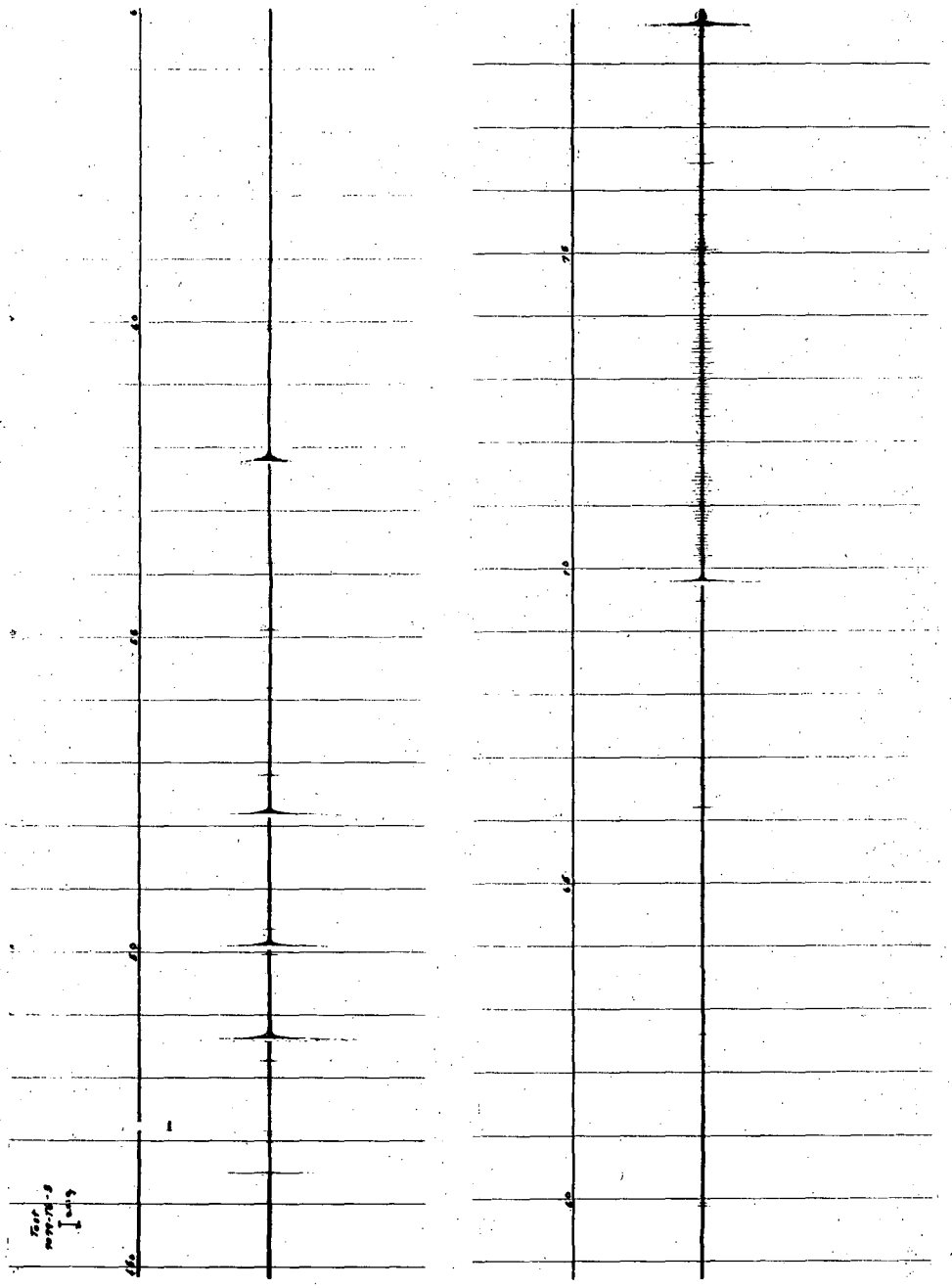

XBL 691-49

Fig. 3 Oscillogram of stress-waves corresponding to Fig. 2. The time lines are 1 sec. apart and the approximate total test time (secs.) is given along the top line.

TABLE 2. Stress-Wave and Crack Opening Displacement Analysis for Test No. 7079-T6-3.
a_o = 0.60 in. B = 0.071 in.

time, sec	COD No.	No. of SW	Amplitude of SW, g. accel.	L_o/L_f lbs.	a_o/a_f, in.	Δa, -in.	K_o/K_f, ksi $\sqrt{in}$
0-46.5							
46.5	1	3	off-scale to 47.50	780/667	.608/.738	.130	40.6/38.3
47.5		2	.004				
48.3		1	.012				
48.7	2	1	.157	694/600	.755/.88	.125	40.5/38.6
49.1		1	.024				
50.2	3	1	.193	612/524	.900/1.024	.124	40.1/38.0
50.3		1	.012				
50.6		2	.004				
52.2	4	1	.157	544/468	1.028/1.125	.097	39.6/37.1
52.8		1	.030				
53.6		1	.006				
54.3		1	.006				
55.2		1	.036				
56.3		1	.024				
57.7	5	1	.145	510/397	1.144/1.340	.196	41.3/39.7
59.8		2	.012				
62.6		1	.012				
66.3		1	.036				
69.5		1	.012				
69.7	6	1	.157	419/330	1.530/1.670	.140	54.6/54.2

TABLE 2 continued:

time, sec	COD No.	No. of SW	Amplitude of SW, g.accel.	L_o/L_f lbs.	a_o/a_f, in.	Δa, in.	K_o/K_f, ksi $\sqrt{in}$
70-71		23	< .012				
71-72		20	< .036				
72-73		23	< .048				
73-74		24	< .048				
74-75		25	< .012				
75-76		15	< .036				
76-77		4	< .006				
77-78		8	< .006				
78.5		2	.006				
78.7	7	1	.132	344/242	1.790/1.690	.160	70.3
		2	.012				

was evident because of the absence of the normal exponential decay of the wave and the fineness of the line following the wave. Table 2 shows that the stress intensity (K) for the initiation of the crack growth was 40.6 ksi $\sqrt{in.}$ The crack had jumped 0.130 in. during the pop-in.

The mechanical properties of aluminum-zinc alloys are given in Figs. 4 to 7 and Tables 3 to 10.* Similarly the results for aluminum-silver alloys are given in Figs. 18 to 27 and Tables 11 to 14.*

Attention is drawn to the fact that the results of the routine fracture tests are based on the original fatigue crack length and the maximum load. The instrumented fracture tests showed that in certain cases there was considerable slow crack growth before the maximum load was reached. Also, in certain cases the point of maximum load coincided with a change in fracture surface appearance. The stress intensity factor in these cases was recalculated for the routine tests so as to be based on the point of transition and the maximum load. The values achieved in this way tend to be higher than values calculated from the instrumented tests. More will be said about this problem in the discussion.

---

*The column marked "n" refers to the work hardening exponent, when the work hardening of a material is assumed to obey a power law $\sigma = k\ \epsilon^n$ where

σ = stress
k = strength coefficient
ϵ = true strain.

In the column marked "%TF" are estimates of the percentage of the fracture area which is transgranular, determined with a stereo-microscope.

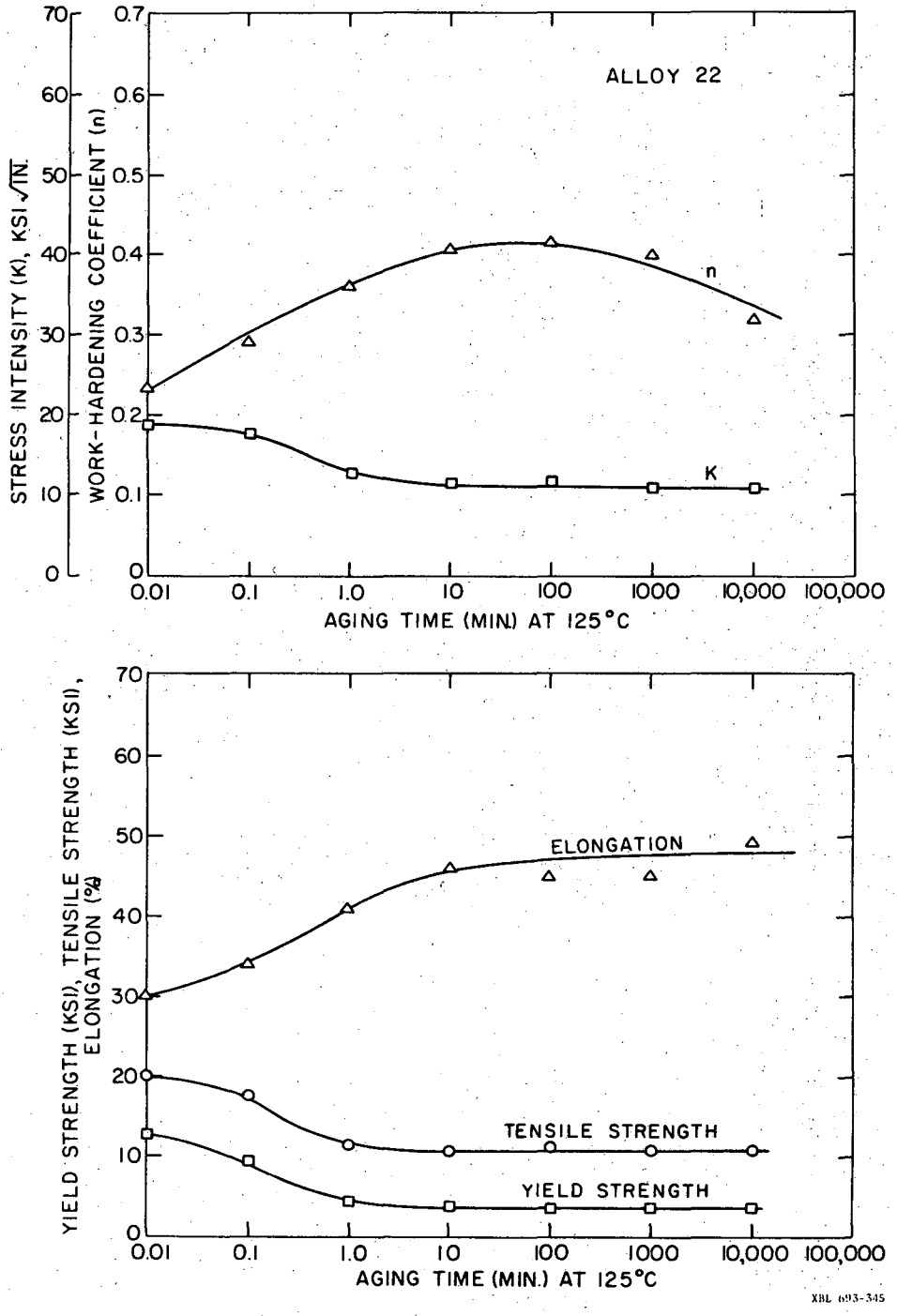

Fig. 4 The mechanical properties of alloy 22 (Al-6.8% Zn) as a function of aging time at 125°C.

Table 3. Mechanical Properties of Alloy 22 (Al - 6.8% Zn).
Solution Treated for 60 min. at 425°C, Quenched in Ice Water, and Aged at 125°C.

				Tensile Properties					Fracture Properties				
Test No.	t, in.	Aging time, min.	Test temp, °C	$\dot{\epsilon}$, 1/min.	Elong, %	YS, ksi	UTS, ksi	N	Test No.	CHS†, cm/min.	K, ksi$\sqrt{in}$	K/YS, $\sqrt{in}$.	% TF‡
148	.0625	0	RT	.39	31	12.9	20.1	.23	323	.1	19.9		
149	.0625	0	RT	.39	28	12.9	19.8	.24	324	.1	17.5		
Average					29.5	12.9	19.95	.235			18.7	1.45	90
498	.125	0	RT	.39	37	14.1	22.6	.23					
499	.125	0	RT	.39	40	13.9	22.3	.24					
Average					38.5	14.0	22.45	.235					
414	.0625	0	LN_2	.39	39	15.0	34.6	.38					
415	.0625	0	LN_2	.0039	35	14.0	33.2	.35					
Average													
146	.0625	.1	RT	.39	31	9.2	17.2	.29	321	.1	15.3		
147	.0625	.1	RT	.39	37	9.7	18.0	.29	322	.1	20.2		
Average					34	9.45	17.6	29			17.75	1.88	98
150	.0625	1	RT	.39	43	4.6	11.9	.36	325	.1	12.5		
151	.0625	1	RT	.39	39	4.3	10.9	.36	326	.1	12.8		
Average					41	4.45	11.4	.36			12.65	2.82	99
152	.0625	10	RT	.39	39	3.8	10.5	.40	327	.1	11.3		
153	.0625	10	RT	.39	52	4.0	11.1	.41	328	.1	11.0		
Average					45.5	3.9	10.8	.405			11.15	2.87	99
154	.0625	100	RT	.39	39	3.7	10.6	.41	329	.1	11.8		
155	.0625	100	RT	.39	51	3.5	11.6	.42	330	.1	11.2		
Average					45	3.6	11.1	.415			11.5	3.20	100
166	.0625	1000	RT	.39	48	4.3	11.0	.36	331	.1	10.4		
167	.0625	1000	RT	.39	39	3.4	10.7	.44	332	.1	11.4		
Average					44.5	3.85	10.85	.40			10.9	2.80	100
500	.125	1000	RT	.39	60	3.1	11.1	.40					
501	.125	1000	RT	.39	57	3.9	11.3	.35					
Average					58.5	3.5	11.2	.375					
378	.0625	10,000	RT	.39	-	3.5	10.5	-	396	.1	10.5		
379	.0625	10,000	RT	.39	49	3.5	11.1	.32	397	.1	11.1		
Average					49	3.5	10.8	.32			10.8	3.09	100

† CHS = Crosshead Speed

‡ TF = Transgranular Fracture

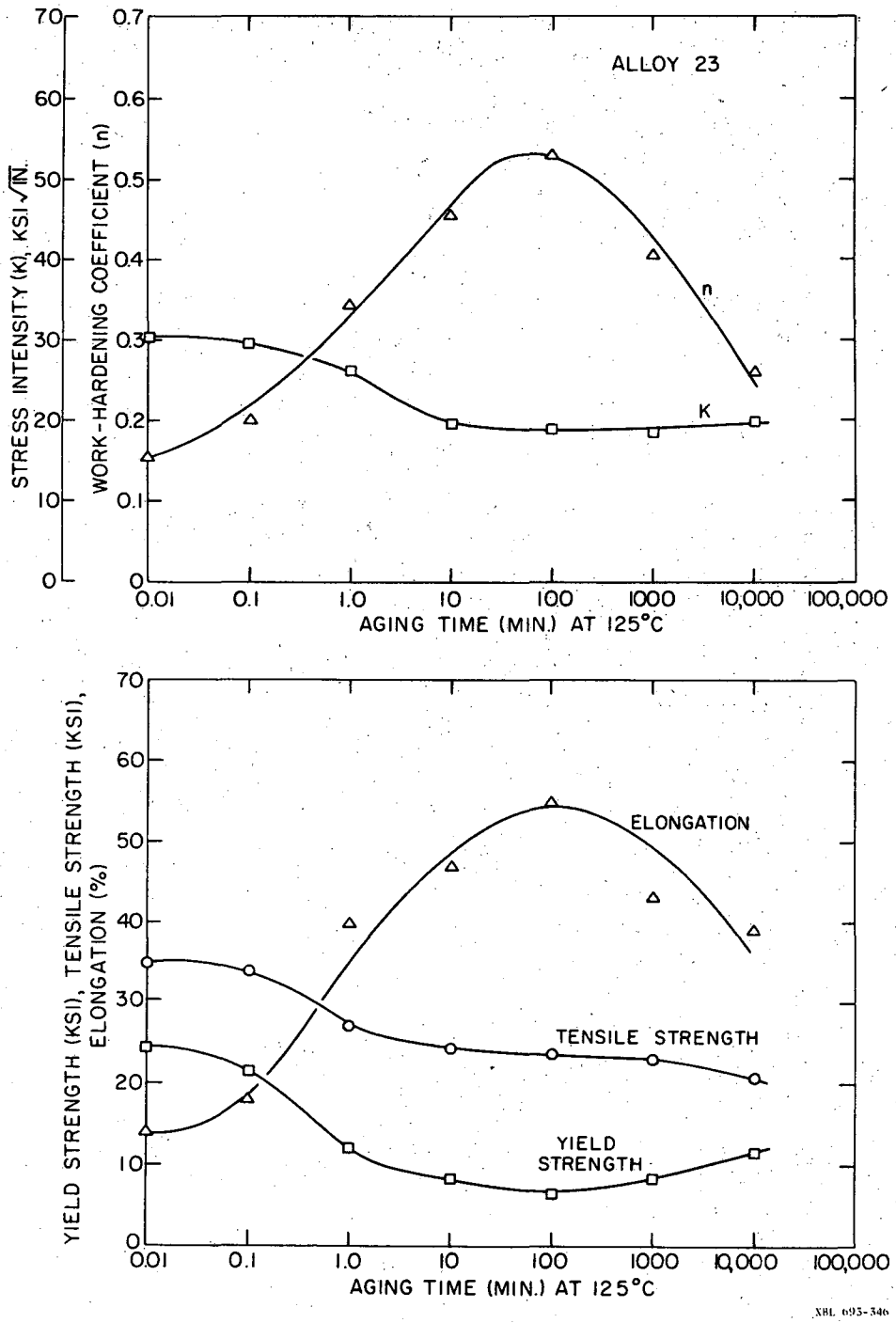

Fig. 5 The mechanical properties of alloy 23 (Al-12.9% Zn) as a function of aging time at 125°C

Table 4 Mechanical Properties of Alloy 23 (Al - 12.9% Zn).
Solution Treated for 60 min. at 425°C, Quenched in Ice Water, and Aged at 125°C.

					Tensile Properties					Fracture Properties			
Test No.	t, in.	Aging time, min.	Test temp, °C	ε̇, 1/min.	Elong, %	YS, ksi	UTS, ksi	N	Test No.	CHS†, cm/min.	K, ksi√in.	K/YS, √in.	% TF‡
156	.0625	0	RT	.39	12	24.4	34.8	.15	297	.1	30.8		
157	.0625	0	RT	.39	15	24.8	35.3	.16	298	.1	30.2		
Average					13.5	24.6	35.05	.155			30.5	1.24	10
502	.125	0	RT	.39	13	26.9	36.0	.15	496	1.0	no meaningful data		
503	.125	0	RT	.39	17	26.9	36.3	.15	497	1.0			
Average					15	26.9	36.15	.15					
158	.0625	.1	RT	.39	19	21.5	34.2	.20	333	.1	29.6		
159	.0625	.1	RT	.39	16	21.6	33.9	.20	334	.1	29.8		
Average					17.5	21.55	34.05	.20			29.7	1.38	10
160	.0625	1.	RT	.39	39	11.5	26.8	.35	335	.1	26.0		
161	.0625	1.	RT	.39	40	12.6	27.4	.34	336	.1	26.8		
Average					39.5	12.05	27.1	.345			26.4	2.20	35
162	.0625	10	RT	.39	47	8.3	24.3	.46	337	.1	20.4		
163	.0625	10	RT	.39	47	8.3	24.6	.45	338	.1	18.9		
Average					47	8.3	24.45	.455			19.65	2.37	60
164	.0625	100	RT	.39	48	6.5	23.3	.50	339	.1	19.1		
165	.0625	100	RT	.39	62	6.4	24.2	.56	340	.1	18.8		
Average					55	6.45	23.75	53			18.95	2.92	70
418	.0625	100	LN_2	.39	60	9.2	27.4	55					
419	.0625	100	LN_2	.039	62	9.8	26.3	49					
168	.0625	1,000	RT	.39	43	8.0	22.9	.42	341	.1	18.1		
169	.0625	1,000	RT	.39	42	8.6	23.2	.39	342	.1	18.4		
Average					42.5	8.3	23.05	.405			18.25	2.20	80
504	.125	1,000	RT	.39	49	8.9	24.2	.38					
505	.125	1,000	RT	.39	47	10.0	24.3	.36					
Average					48	9.45	24.25	.37					
380	.0625	10,000	RT	.39	37	11.0	20.1	.27	398	.1	20.0		
381	.0625	10,000	RT	.39	40	11.9	21.2	.25	399	.1	20.0		
Average					38.5	11.45	20.65	.26			20.0	1.74	90

† CHS = Crosshead Speed
‡ TF = Transgranular Fracture

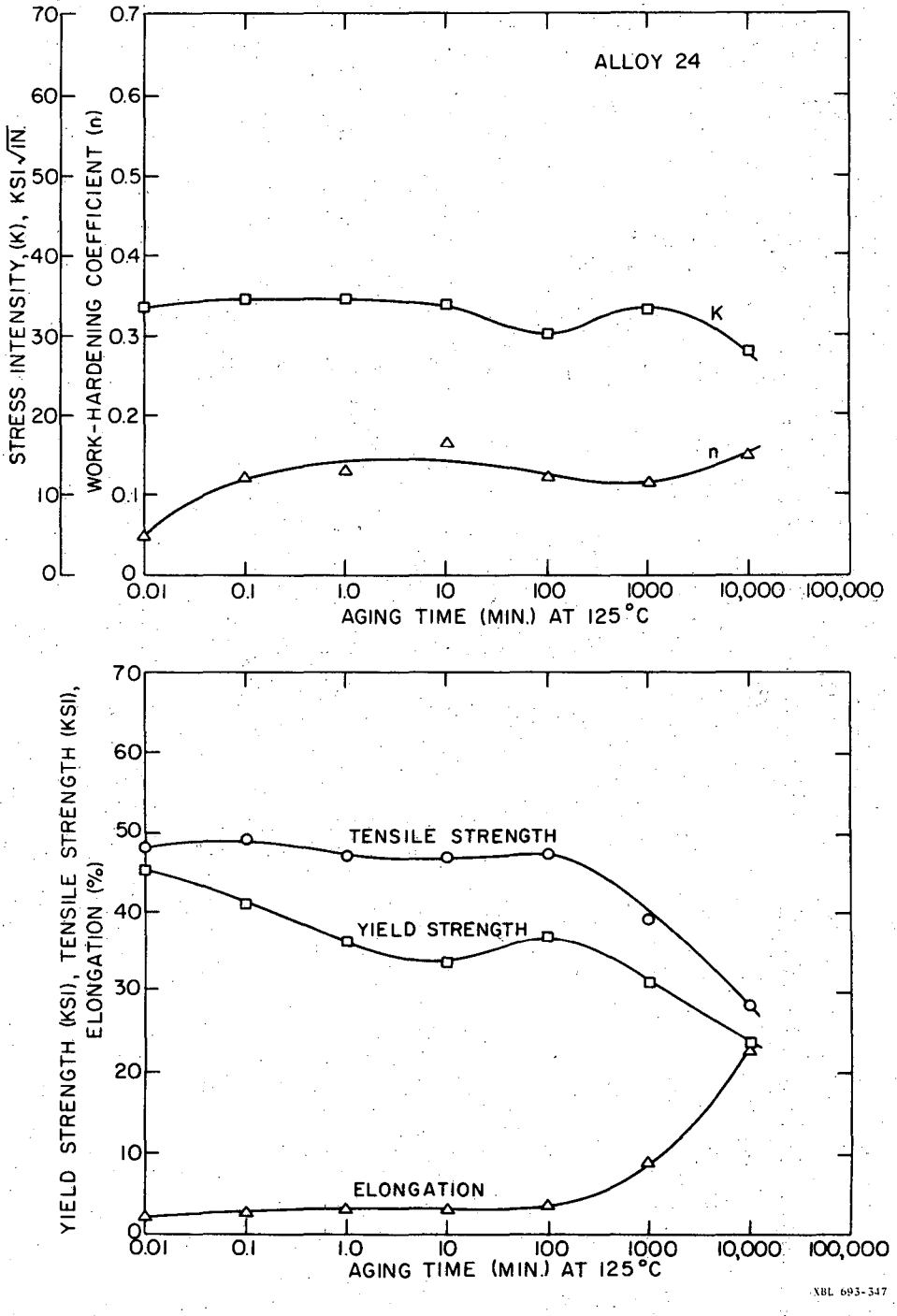

Fig. 6 The mechanical properties of alloy 24 (Al-25.7% Zn) as a function of aging time at 125°C.

TABLE 5. Mechanical Properties of Alloy 24 (Al - 25.7% Zn)
Solution treated for 60 min. at 425°C, Quenched in Ice Water, and Aged at 125°C.

				Tensile Properties						Fracture Properties			
Test No.	t, in.	Aging time, min.	Test temp, °C	ε̇, 1/min.	Elong, %	YS, ksi	UTS, ksi	N	Test No.	CHS†, cm/min.	K, ksi√in.	K/YS, √in.	% TF‡
170	.0625	0	RT	.39	3.0	46.8	49.4	.07	285	.1	36.5(61)**		
171	.0625	0	RT	.39	1.0	44.2	46.8	.03	286	.1	30.1(80)**		
Average					2.0	45.5	48.1	.05			33.3(70.5)**	.732	0
506	.125	0	RT	.39	4.0	46.3	49.1	.07	490	.1	19.0		
507	.125	0	RT	.39	4.0	46.2	48.9	.07	t = .125				
Average					4.0	46.25	49.0	.07	491	1.0	12.2(61.2)*		
									492	1.0	17.4 (high)		
24ST-1 *	.0625	0	RT	.39	4.5	47.6	53.0	.07	534	1.0	14.3(57.8)*		
24ST-3 *	.0625	0	RT	.39	2.4	47.8	49.8	.05					
432 *	.0625	0	RT	.39	2.4	39.7	45.6	.14					
24ST-2	.0625	0	RT	.0035	.6	40.5	44.3	.11					
431	.0625	0	RT	3.9	3.9	47.7	51.1	.07					
416	.0625	0	LN_2	.0039	.3	49.5	50.3	.04					
417	.0625	0	LN_2	.39	.4	49.0	51.7	.07					
427	.0625	0	120°C	.39	4.7	29.0	33.9	.06					
429	.0625	0	180°C	.0039	1.6	14.3	17.0	.03					
428	.0625	0	180°C	.39	3.9	19.1	22.8	.07					
172	.0625	.1	RT	.39	3.0	42.4	50.3	.11	287	.1	33.2(69)**		
173	.0625	.1	RT	.39	2.0	40.0	48.4	.14	288	.1	35.9(85)**		
Average						41.2	49.35	.125			34.55(77)**	.842	0
174	.0625	1	RT	.39	4.0	37.1	46.1	.11	289	.1	34.8		
175	.0625	1	RT	.39	2.0	35.5	48.1	.15	290	.1	34.3		
Average					3.0	36.3	47.1	.13			34.55	.952	3
176	.0625	10	RT	.39	3.0	33.1	47.0	.13	291	.1	35.5		
177	.0625	10	RT	.39	3.0	34.7	47.0	.20	292	.1	32.3		
Average					3.0	33.9	47.0	.165			33.9	1.00	3
178	.0625	100	RT	.39	4.0	37.4	48.1	.10	293	.1	28.7		
179	.0625	100	RT	.39	3.0	36.8	47.1	.14	294	.1	31.5		
Average					3.5	37.1	47.6	.12			30.1	181	3
180	.0625	1000	RT	.39	9.0	31.3	39.2	.11	295	.1	33.2		
181	.0625	1000	RT	.39	9.0	31.3	39.2	.12	296	.1	32.6		
Average					9.0	31.3	39.2	.115			32.9	1.07	10
508	.125	1000	RT	.39	11.0	35.9	41.6	.11	535	1.0	no meaningful data		
509	.125	1000	RT	.39	12.0	33.1	40.6	.12	542	1.0	42.3		
Average					11.5	34.5	41.1	.115					
382	.0625	10,000	RT	.39	24.0	24.4	28.1		400	.1	27.3		
383	.0625	10,000	RT	.39	22.0	22.5	28.6	.15	401	.1	28.4	1.19	75
Average					23.0	23.45	28.35	.15			27.85		

* 24ST-1 Solution treated for 40 min. at 425°C.
24ST-3 " " " 420 min. at 425°C.
432 " " " 4400 min. at 425°C.

** The values in brackets are for cleavage type fracture

† CHS = Crosshead Speed

‡ TF = Transgranular Fracture

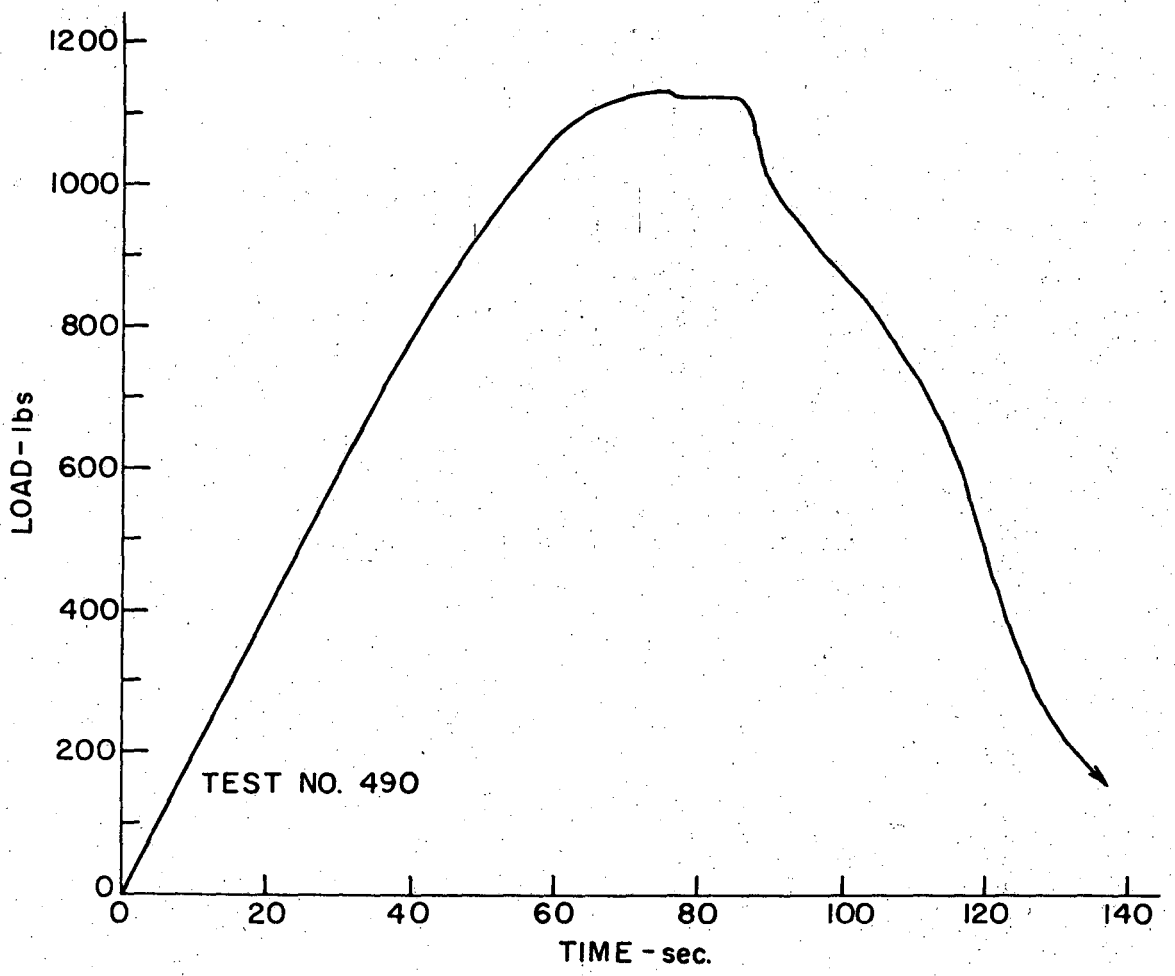

XBL 691-120

Fig. 7 Load versus time curve for a large SEN fracture specimen of alloy 24, solution treated and aged at room temperature for 30 min. Tested at 0.039 in./min.

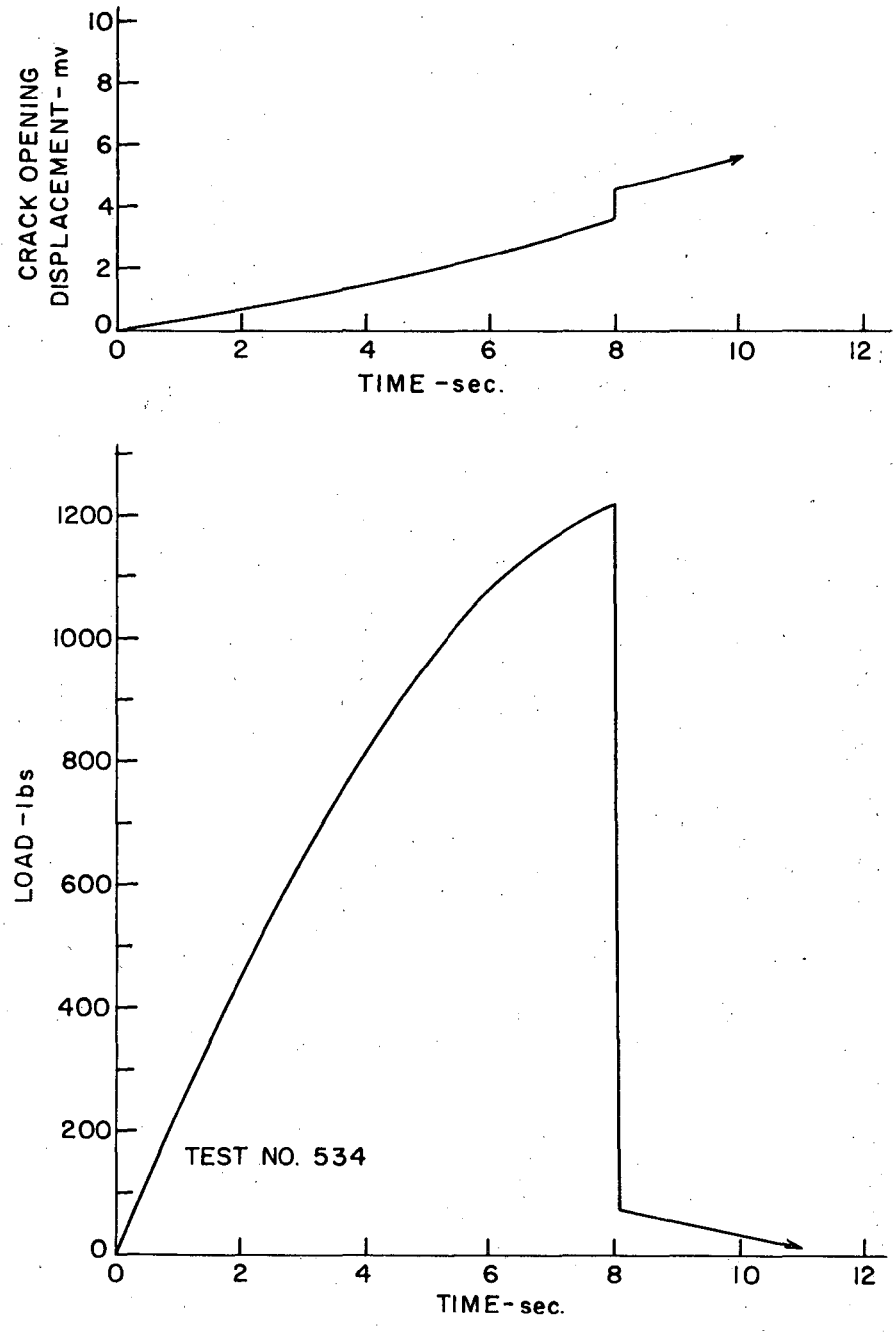

Fig. 8 Crack opening displacement gage output and load versus time records for a large SEN fracture specimen of alloy 24, solution treated and aged at room temperature for 30 min. Tested at 0.39 in./min.

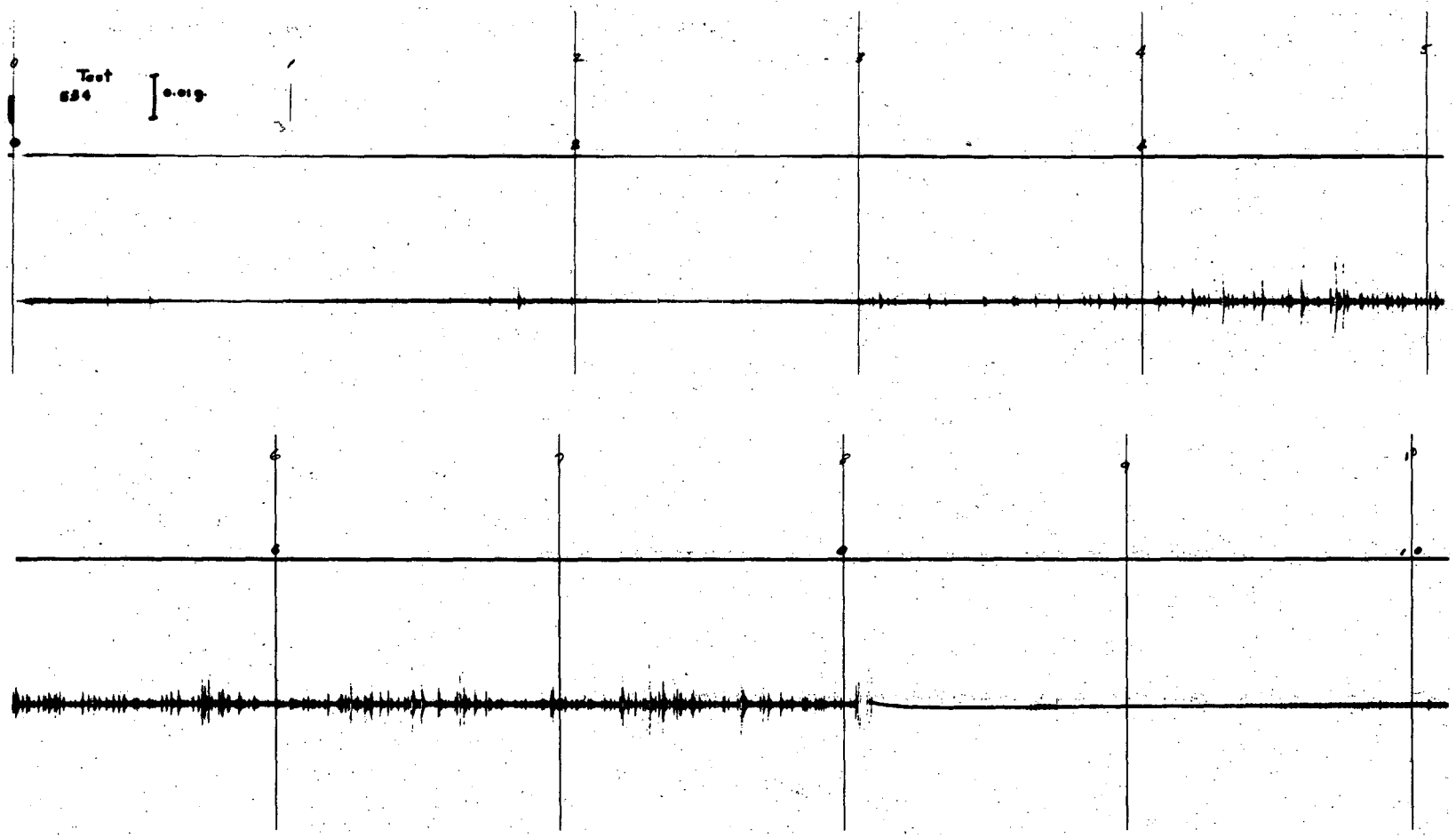

XBL 691-47

Fig. 9 Oscillogram of stress-waves corresponding to Fig. 8. The time lines are 1 sec. apart and the approximate total time (secs.) is given along the top line.

TABLE 6. Stress-Wave and Crack Opening Displacement Analysis for Test No. 534.

a_o = .740 in.

time, sec	COD No.	No. of SW	Amplitude of SW, g. accel.	L_a/L_f, lbs.	a_o/a_f, in.	Δa, in.	K_o/K_f ksi $\sqrt{in}$
0-1.8		3	< .01				
1.8		1	.008	396	.863		14.3
1.8-2		1	< .01				
2-3		4	< .01				
3-4		16	< .03				
4-5		42	< .03				
5				968	.975		38.3
5-6		59	< .03				
6-7		50	< .03				
7-8		48	< .03				
8.05	Pt. of max. load	1	off scale	1220	1.180		57.8

Note: The average jump between minor stress-waves is on the order of 0.001 in.

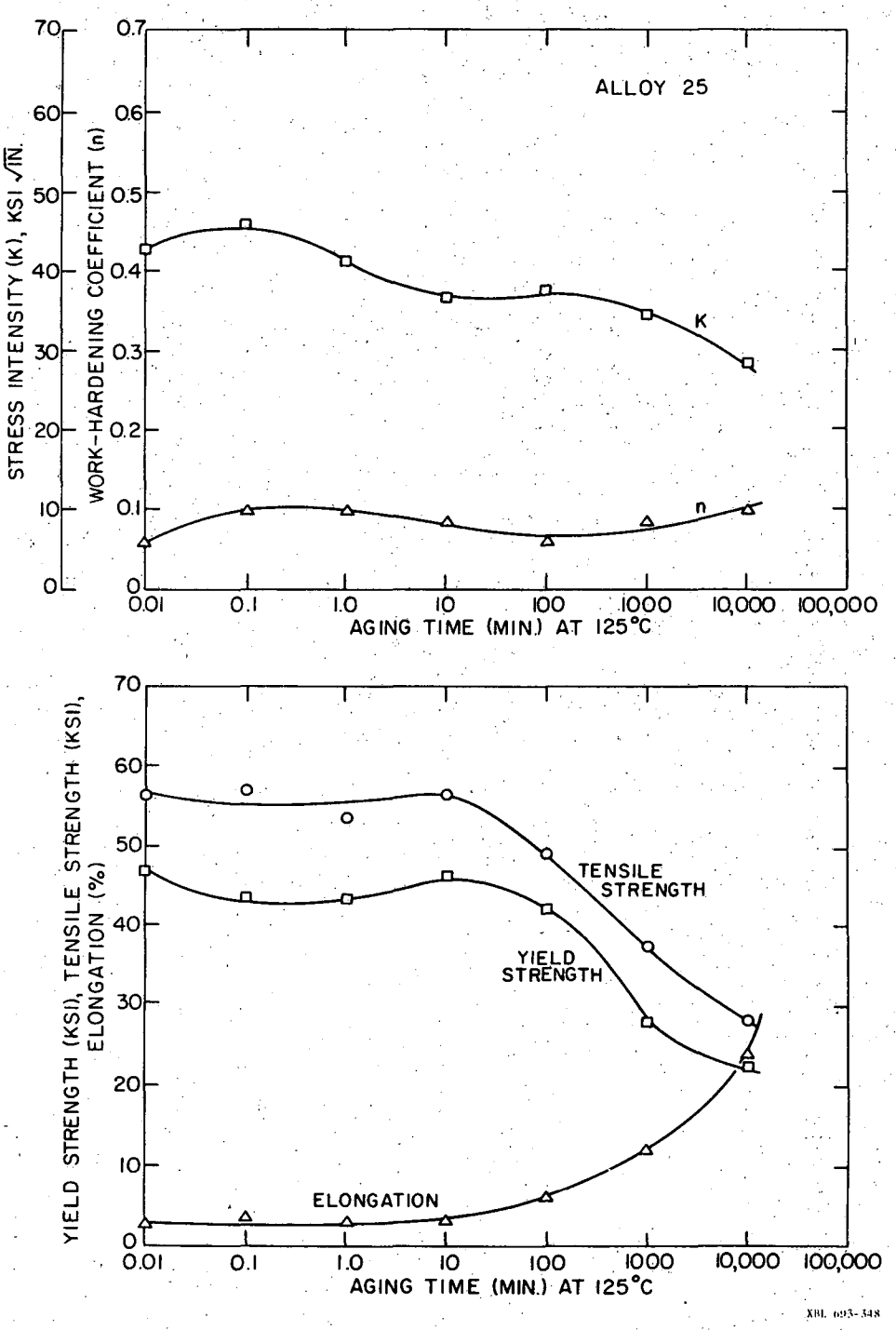

Fig. 10 The mechanical properties of alloy 25 (Al-36.8% Zn) as a function of aging time at 125°C.

Table 7. Mechanical Properties of Alloy 25 (Al - 36.8% Zn).
Solution Treated for 60 min at 425°C, Quenched in Ice Water, and Aged at 125°C.

				Tensile Properties					Fracture Properties				
Test No.	t, in.	Aging time, min.	Test temp, °C	ε̇, 1/min.	Elong, %	YS, ksi	UTS, ksi	N	Test No.	CHS†, cm/min.	K, ksi√in.	K/Y, √in.	% TF‡
182	.0625	0	RT	.39	2.0	48.1	54.5	.06	273	.1	42.5(87)**		
183	.0625	0	RT	.39	3.0	46.0	58.8	.06	274	.1			
Average					2.5	47.05	56.65	.06			42.5(87)**	0.902	0
510	.125	0	RT	.39	3.0	53.1	55.5	.05	493	1.0	12.8(49.5)**		
511	.125	0	RT	.39	3.0	55.1	56.5	.05					
Average					3.0	54.1	56.0	.05					
184	.0625	.1	RT	.39	3.0	44.7	54.9	.1	275	.1	45.4(94)**		
185	.0625	.1	RT	.39	4.0	42.7	59.1	.1	276	.1	46.2(98)**		
Average					3.5	43.7	57.0	.1			45.8(96)**	1.05	0
186	.0625	1	RT	.39	3.0	42.7	52.8	.1	277	.1	41.0		
187	.0625	1	RT	.39	3.0	44.3	54.5	.1	278	.1	41.4		
Average					3.0	43.5	53.65	.1			41.2	.946	0
188	.0625	10	RT	.39	3.0	45.6	58.3	.10	279	.1	33.9		
189	.0625	10	RT	.39	3.0	46.5	55.3	.07	280	.1	39.2		
Average					3.0	46.05	56.8	.085			36.55	.788	0
433*	.0625	10	RT	.39	4.7	43.0	56.0	.08					
190	.0625	100	RT	.39	6.0	41.8	48.9	.06	281	.1	36.4		
191	.0625	100	RT	.39	6.0	42.7	49.0	.06	282	.1	38.6		
Average					6.0	42.25	48.95	.06			37.5	.886	2
192	.0625	1,000	RT	.39	15.0	27.7	37.7	.07	283	.1	33.0		
193	.0625	1,000	RT	.39	8.0	28.1	36.5	.1	284	.1	35.8		
Average					11.5	27.9	37.1	.085			34.4	1.23	75
512	.125	1,000	RT	.39	18.0	36.8	40.0	.06	536	1.0	No meaningful data		
513	.125	1,000	RT	.39	14.0	35.0	39.4	.07					
Average					16.0	35.9	39.7	.065					
384	.0625	10,000	RT	.39	22.0	22.6	28.2	.1	406	.1	28.3		
385	.0625	10,000	RT	.39	25.0	22.6	28.2	.1	407	.1	27.8		
Average					23.5	22.6	28.2	.1			28.05	1.17	95

* Solution treated, quenched in ice water, deformed 5% by cold rolling and aged at 125°C.

** The values in brackets are for cleavage type fracture.

† CHS = Crosshead Speed.

‡ TF = Transgranular Fracture.

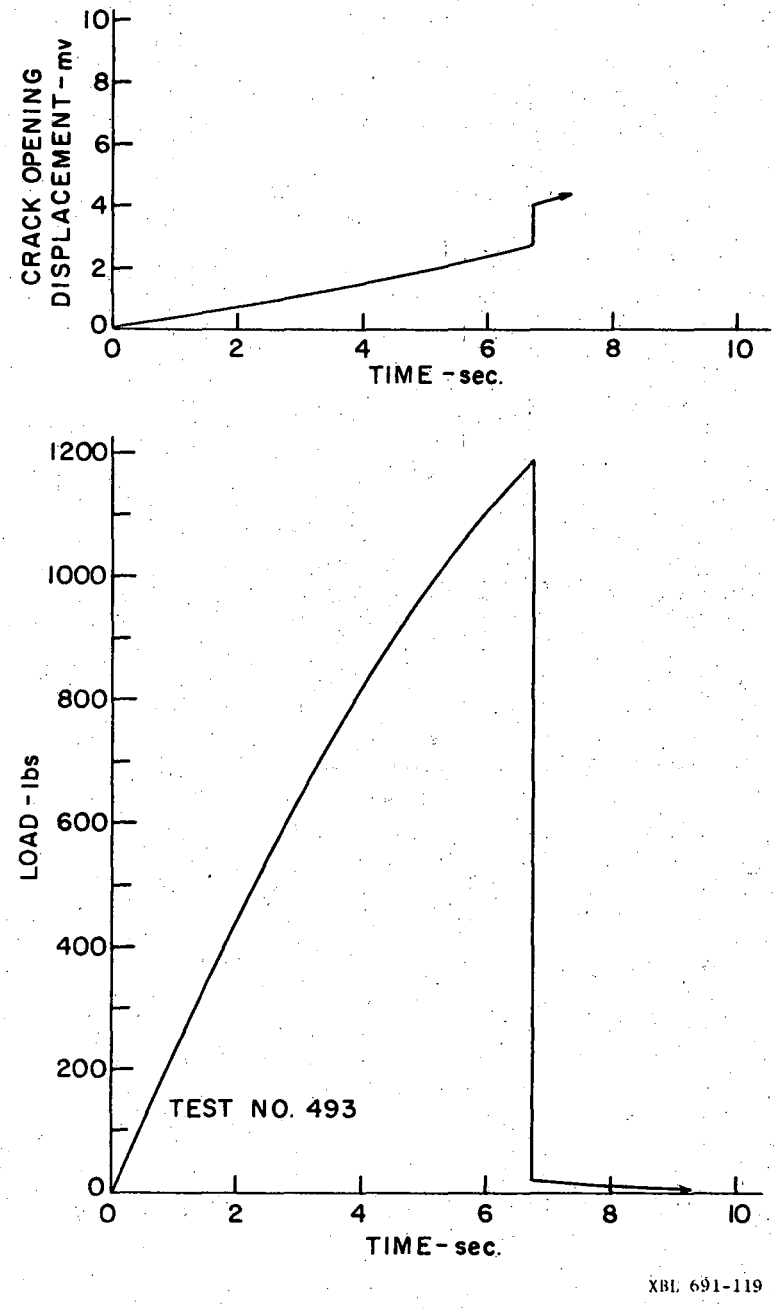

Fig. 11 Crack opening displacement gage output and load versus time records for a large SEN fracture specimen of alloy 24, solution treated and aged at room temperature for 30 min. Tested at 0.39 in./min.

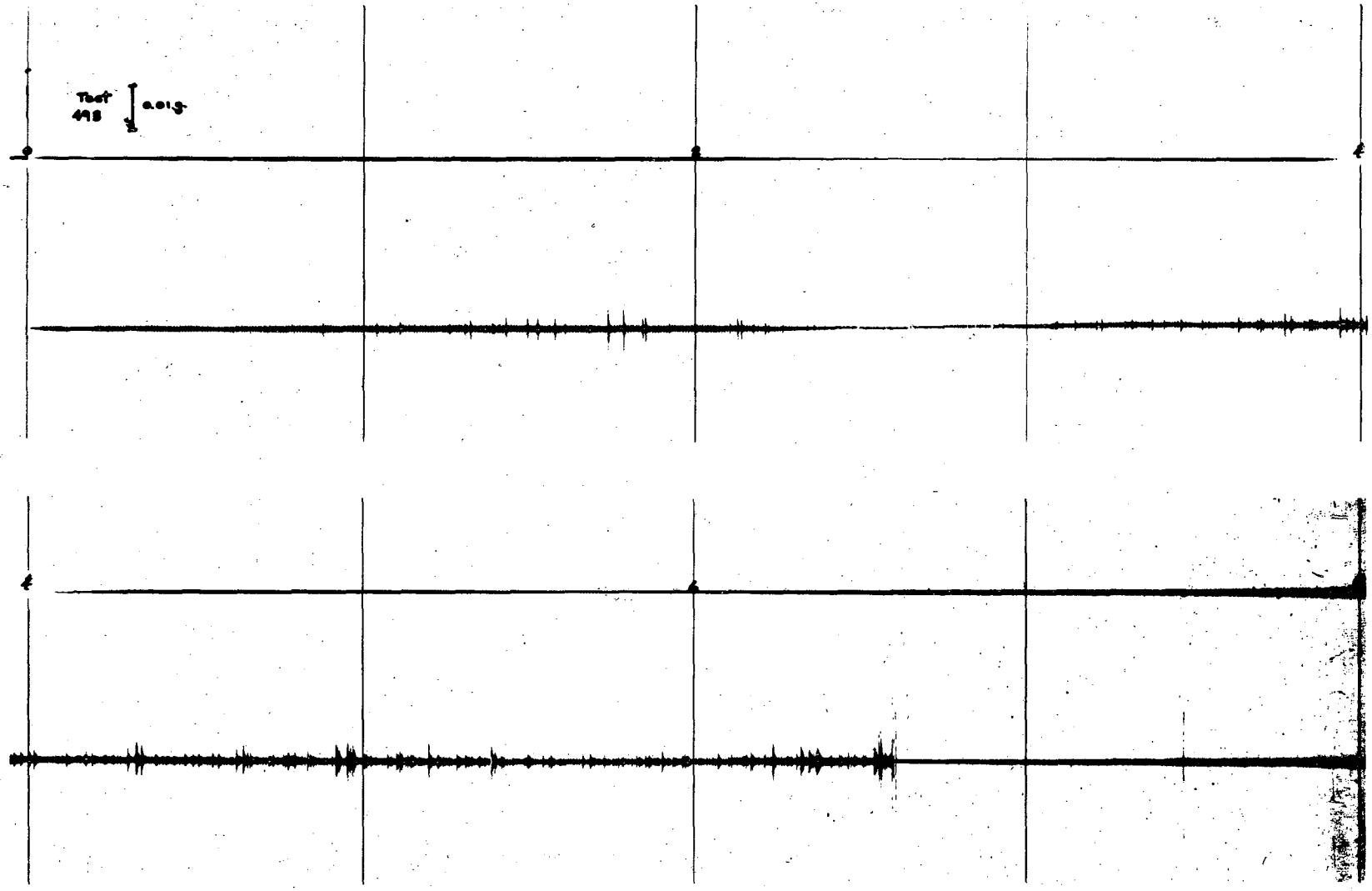

XBL 691-48

Fig. 12 Oscillogram of stress-waves corresponding to Fig. 11. The time lines are 1 sec. apart and the approximate total time (secs.) is given along the top line.

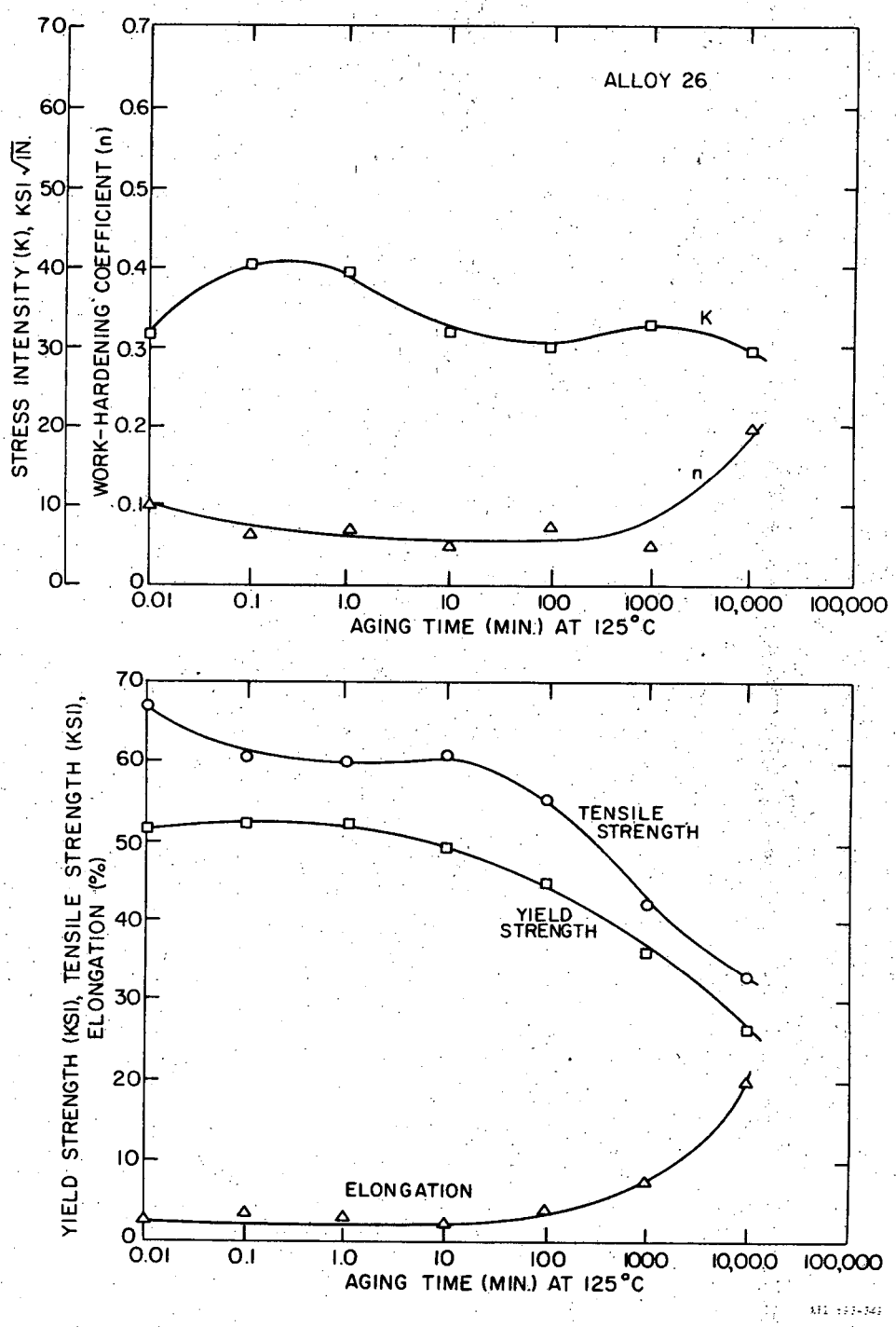

Fig. 13 The mechanical properties of alloy 26 (Al-49.2% Zn) as a function of aging time at 125°C.

Table 8 Mechanical Properties of Alloy 26 (Al - 49.2% Zn).
Solution Treated for 60 min at 425°C, Quenched in Ice Water, and Aged at 125°C.

				Tensile Properties					Fracture Properties				
Test No.	t, in.	Aging time, min.	Test temp, °C	$\dot{\epsilon}$, 1/min.	%Elong, %	YS, ksi	UTS, ksi	n	Test No.	CHS†, cm/min.	K, ksi$\sqrt{in.}$	K/E, $\sqrt{in.}$	% TF‡
194	.0625	0	RT	.39	2.0	51.7	66.2	.1	262	.1	32.1(101)*		
195	.0625	0	RT	.39	3.0	52.2	67.8	.1	263	.1	30.7		
Average					2.5	51.95	67.0	.1			31.4	.605	0
514	.125	0	RT	.39	5.0	50.5	65.9	.14	494	1.0	22.8		
515	.125	0	RT	.39	4.0	62.4	66.9	.07	495	1.0	13.6		
Average					4.5	56.45	66.4	.105			18.2		
196	.0625	.1	RT	.39	4.0	53.1	60.9	.06	264	.1	40.2		
197	.0625	.1	RT	.39	3.0	52.2	61.3	.07	265	.1	40.3		
Average					3.5	52.65	61.1	.065			40.25	.766	0
198	.0625	1	RT	.39	3.0	52.6	60.5	.07	266	.1	43.3		
199	.0625	1	RT	.39	3.0	52.2	60.0	.07	267	.1	36.3		
Average					3.0	52.4	60.25	.07			39.8	.760	
200	.0625	10	RT	.39	2.0	53.5	61.3	.05	268	.1	33.8		
201	.0625	10	RT	.39	2.0	45.7	61.3	-	269	.1	29.7		
Average					2.0	49.6	61.3	.05			31.75	.642	0
202	.0625	100	RT	.39	4.0	45.7	54.8	.07	270	.1	30.3		
203	.0625	100	RT	.39	4.0	42.3	56.0	.08	271	.1	29.7		
Average					4.0	44.0	55.4	.075			30.0	.667	2
204	.0625	1,000	RT	.39	7.0	35.8	41.4	.05	272	.1	33.0		
205	.0625	1,000	RT	.39	8.0	36.5	43.0	.05	343	.1			
Average					7.5	36.15	42.2	.05			33.0	.914	60
516	.125	1,000	RT	.39	9.0	40.5	42.6	.06	537	1.0	No meaningful data		
517	.125	1,000	RT	.39	11.0	40.5	42.8	.07	543	1.0			
Average					10.0	40.5	42.7	.065					
386	.0625	10,000	RT	.39	18.0	26.6	33.4	.1	408	.1	25.9		
387	.0625	10,000	RT	.39	22.0	-	32.9	.3	413	.1	31.4		
Average					20.0	26.6	33.15	.2			28.65	1.06	85

* The value in brackets is for cleavage type fracture.

† CHS = Crosshead Speed.

‡ TF = Transgranular Fracture.

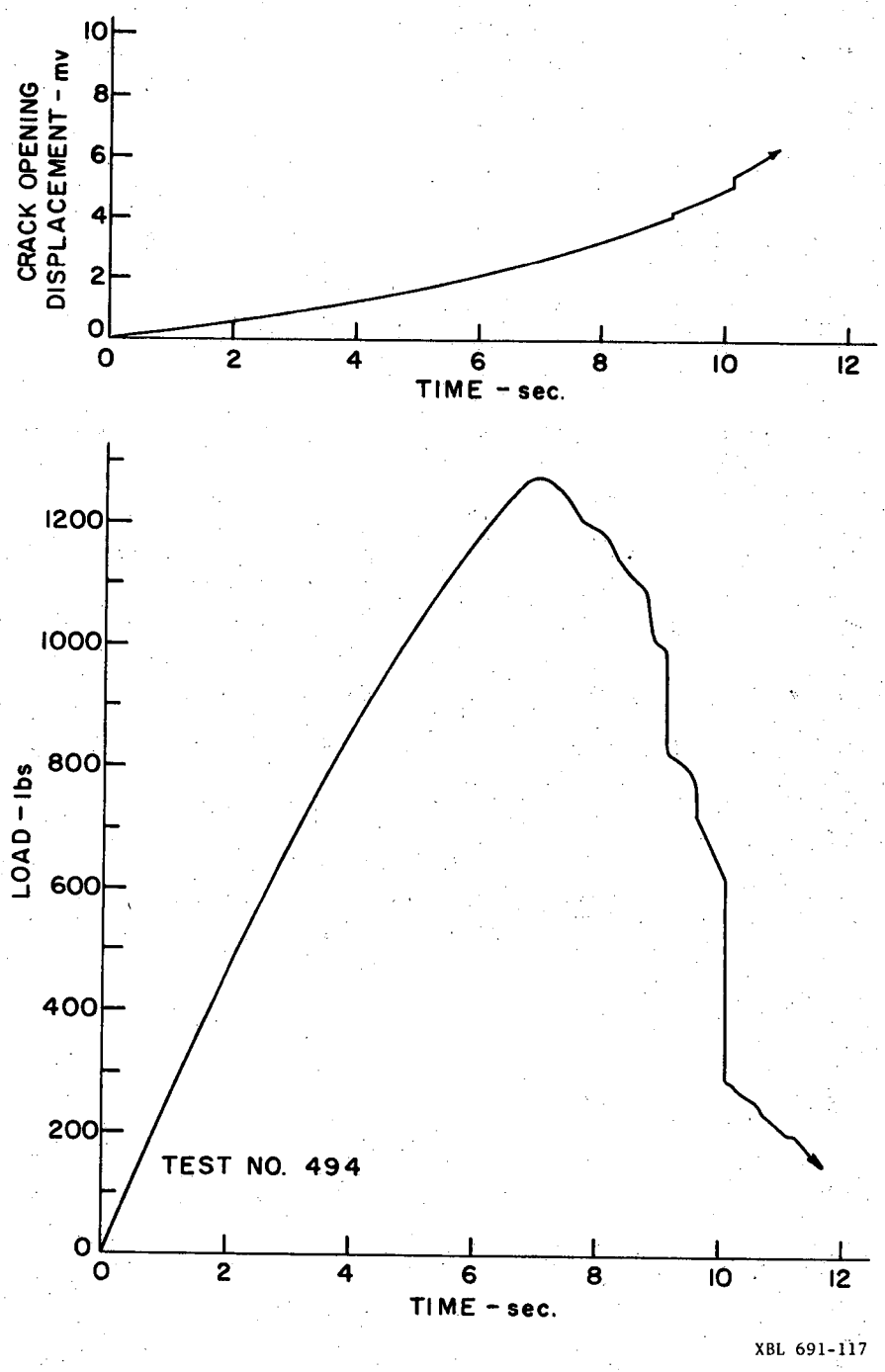

Fig. 14 / Crack opening displacement gage output and load versus time records for a large SEN fracture specimen of alloy 26, solution treated and aged at room temperature for 30 min. Tested at 0.39 in./min.

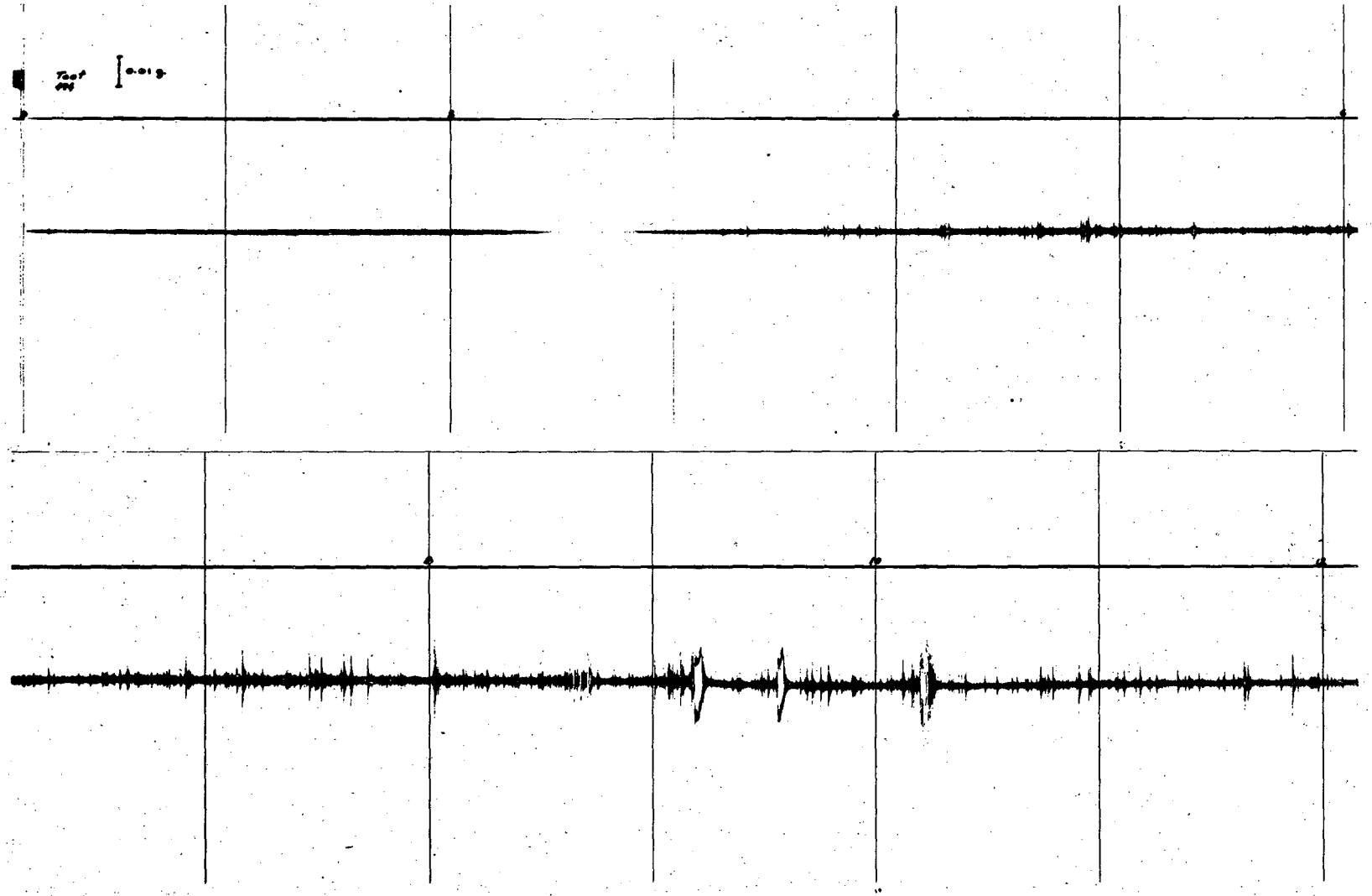

XBL 691-43

Fig. 15 Oscillogram of stress-waves corresponding to Fig. 14. The time lines are 1 sec. apart and the approximate total time (secs.) is given along the top line.

TABLE 9. Stress-Wave and Crack Opening Displacement Analysis for Test No. 494.

a_o = .700 in.

time sec.	COD No.	No. of SW	Amplitude of SW, g. accel.	L_o/L_f, lbs	a_o/a_f, in.	Δa, in	K_o/k_f ksi $\sqrt{in.}$
0-3.3		0					
3.3		1	.004	720	.762		
3.3-4		10	< .01				
4-5		31	< .01				
5-6		30	< .02				
6-7		32	< .02				
7 (Pt. of max load)				1275	1.010		49.7
7-8		30	< .03				
8-9		40	< .03				
9.1	1	1	.03	1000/825	1.415/1.515	.100	60.0/57.0
9-10		40	< .04				
10.1	2	1	.1	616/286	1.75/> 2.00	>.25	64.2/-
10-11		22	< .02				
11-12		27	<..04				
12-13		18	< .01				
13-14		33	< .01				

Note: The average jump between minor stress-wave is on the order of 0.002 in.

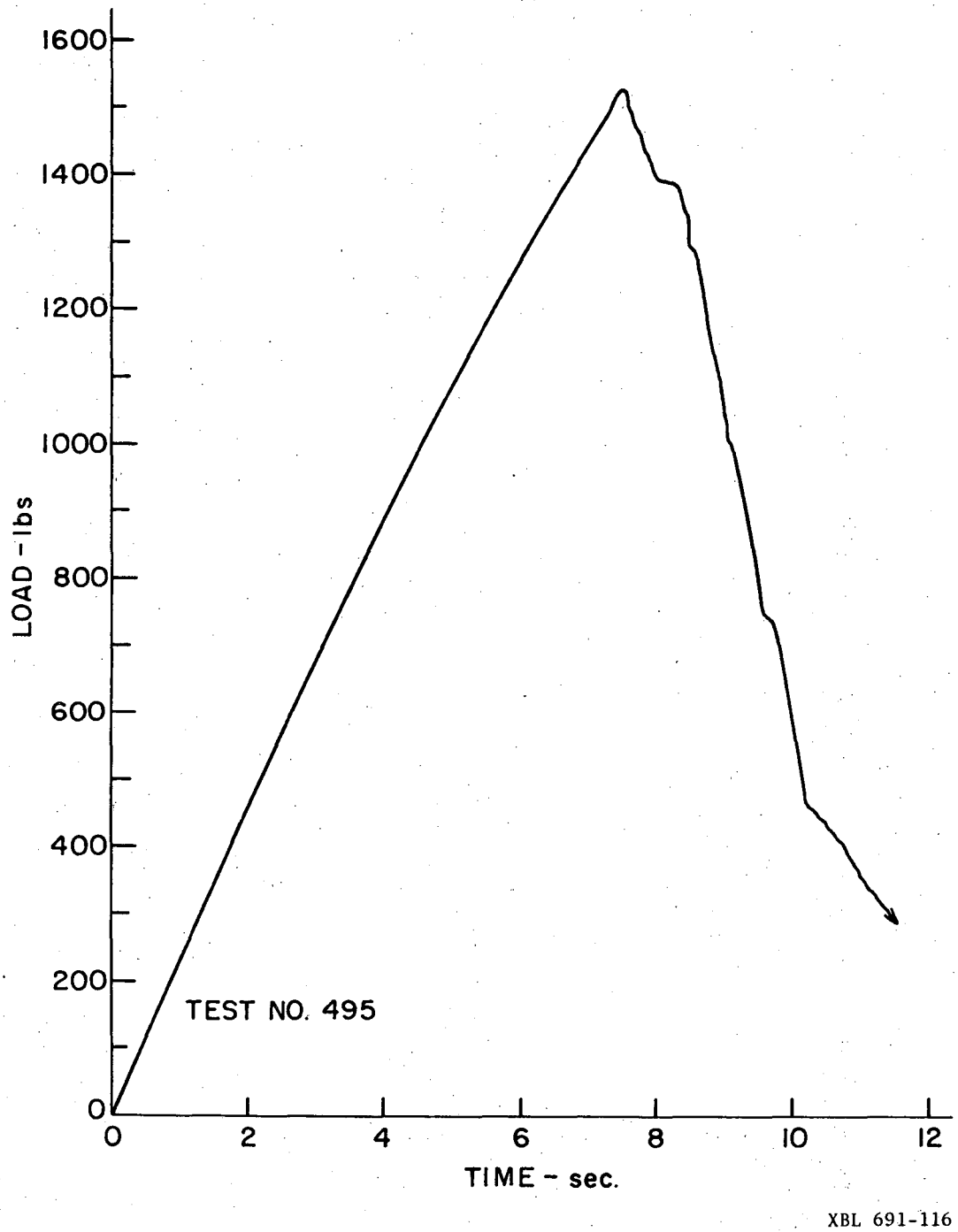

Fig. 16 Load versus time curve for a large SEN fracture specimen of alloy 26, solution treated and aged at room temperature for 30 min. Tested at 0.39 in./min.

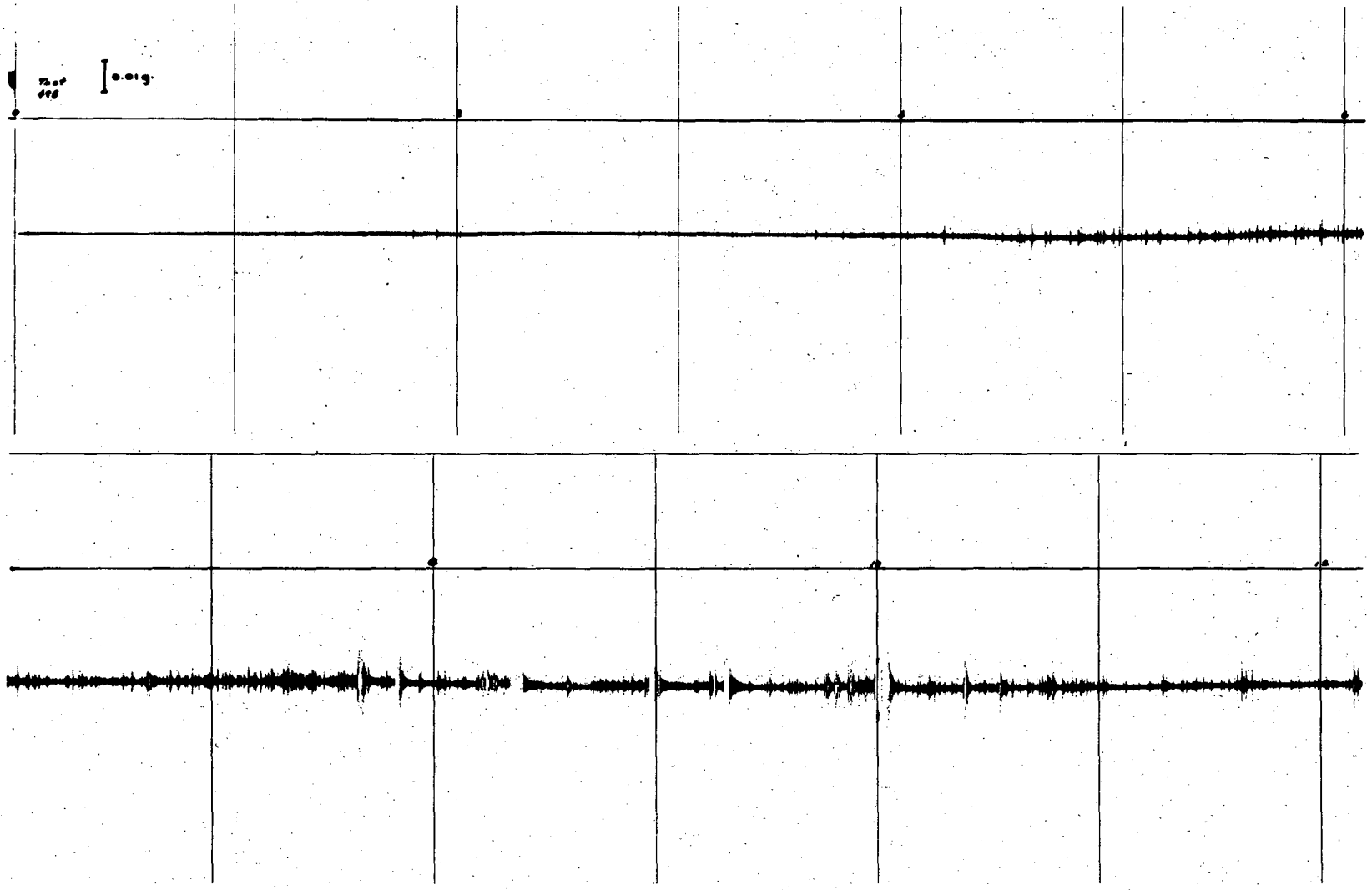

XBL 691-46

Fig. 17 Oscillogram of stress-waves corresponding to Fig. 16. The time lines are 1 sec. apart and the approximate total time (secs.) is given along the top line.

TABLE 10. Stress-Wave and Crack Opening Displacement Analysis for Test No. 495.

a_o = .680 in.

time, sec.	COD No.	No. of SW	Amplitude of SW, g. accel.	L_o/L_f, lbs.	a_o/a_f, in.	Δa, in.	K_o/K_f ksi $\sqrt{in.}$
0-1.8		3	< 0.01				
1.8		1	.01	440	.755		13.6
2-3		2	< .01				
3-4		3	< .01				
4-5		30	< .02				
5-6		41	< .02				
6-7		54	< .02				
7-8		55	< .05				
7.6 Pt. of max.load	1	1	.03	1527/1385	.960/1.045	.095	55.6/53.8
8-9		39	< .05				
8.5	2	1	.05	1385/1290	1.140/1.170	.030	57.0/56.0
9-10		34	< .05				
9.2	3	1	.05	1290/900	1.235/1.490	.255	60.2/58.0
9.5	4	1	.05	900/748	1.510/1.610	.100	61.0/59.0
10-11		36	< .03				
10.1	5	1	.1	748/462	1.660/> 1.750	>.110	64.2/-

Note: The average jump between minor stress-wave is on the order of 0.001 in.

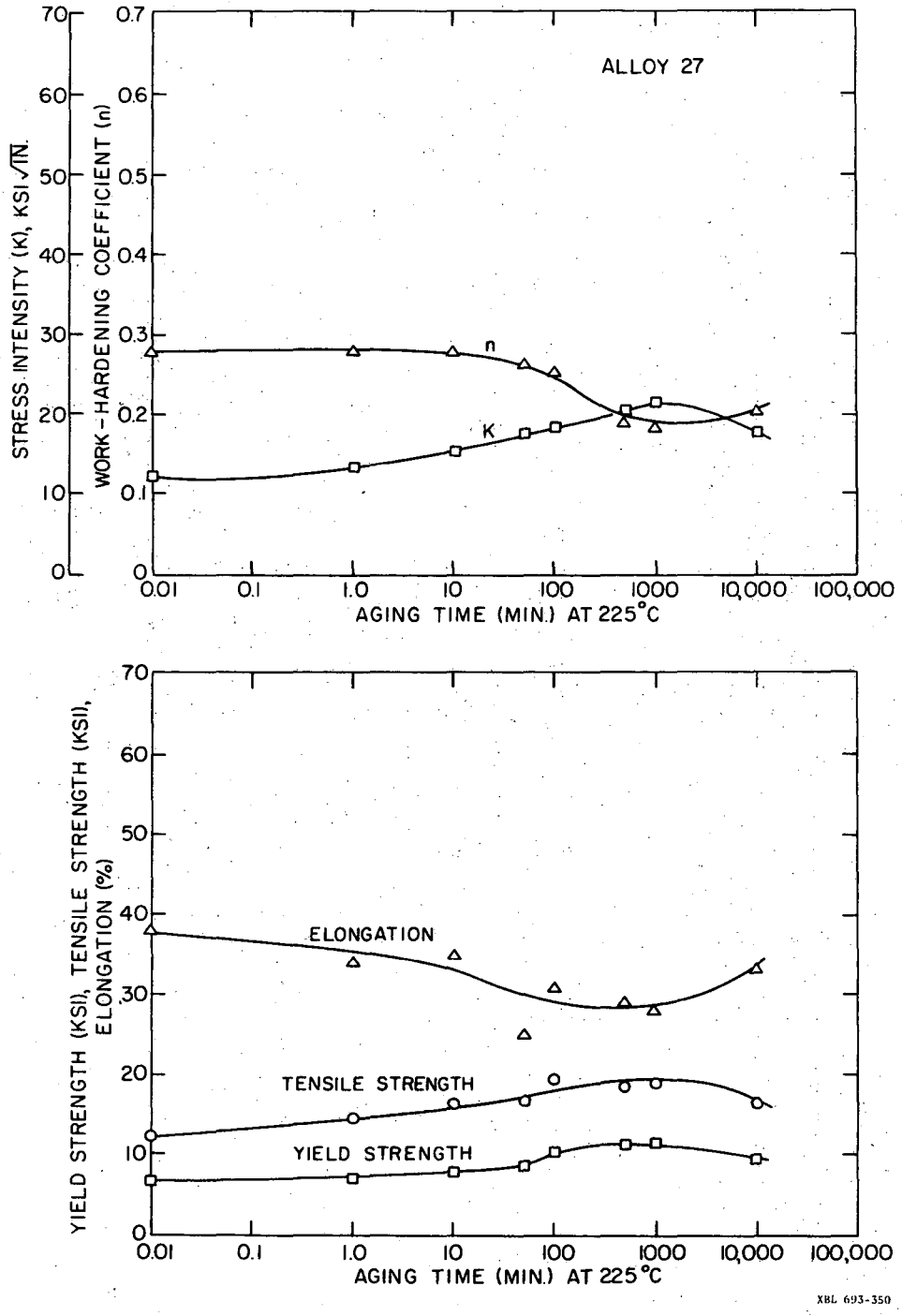

Fig. 18 The mechanical properties of alloy 27 (Al-4.76% Ag) as a function of aging time at 225°C.

Table 11. Mechanical Properties of Alloy 27 (Al - 4.76% Ag).
Solution Treated at 525°C for 60 min., Quenched in Ice Water and Aged at 225°C

				Tensile Properties						Fracture Properties			
Test No.	t, in.	Aging time, min.	Test temp, °C	$\dot{\epsilon}$, 1/min.	Elong. %	YS, ksi	UTS, ksi	N	Test No.	CHS†, cm/min.	K, ksi$\sqrt{\text{in.}}$	K/YS, $\sqrt{\text{in.}}$	% TF‡
206	.0625	0	RT	.39	35	6.9	12.3	.27	344	.1	12.2		
207	.0625	0	RT	.39	41	6.8	12.6	.29	345	.1	11.9		
Average					38	6.85	12.45	.28			12.05	1.75	100
208	.0625	1	RT	.39	33	7.3	14.7	.27	346	.1	13.0		
209	.0625	1	RT	.39	34	6.8	15.0	.29	347	.1	14.2		
Average					33.5	7.05	14.85	.28			13.6	1.92	100
210	.0625	10	RT	.39	32	7.6	16.0	.28	348	.1	16.6		
211	.0625	10	RT	.39	38	8.1	16.8	.28	349	.1	14.8		
Average					35	7.85	16.4	.28			15.7	1.99	100
212	.0625	50	RT	.39	26	8.8	17.2	.26	350	.1	17.5		
213	.0625	50	RT	.39	24	8.5	16.4	.27	351	.1	17.3		
Average					25	8.65	16.8	.265			17.4	2.02	100
214	.0625	100	RT	.39	32	10.4	19.7	.26	352	.1	18.2		
215	.0625	100	RT	.39	29	10.5	19.4	.25	353	.1	18.8		
Average					30.5	10.45	19.55	.255			18.5	1.78	100
518	.125	100	RT	.39	35	10.5	18.6	.25					
519	.125	100	RT	.39	36	10.3	19.0	.25					
Average					35.5	10.4	18.8	.25					
216	.0625	500	RT	.39	30	11.0	17.9	.19	354	.1	21.4		
217	.0625	500	RT	.39	27	11.5	19.2	.19	355	.1	20.1		
Average					28.5	11.25	18.55	.19			20.75	1.86	100
218	.0625	1000	RT	.39	27	11.3	19.1	.19	356	.1	21.7		
219	.0625	1000	RT	.39	26	11.5	18.9	.18	357	.1	20.6		
Average					26.5	11.4	19.0	.185			21.15	1.86	95
520	.125	1000	RT	.39	39	11.1	18.3	.18					
521	.125	1000	RT	.39	39	11.3	17.9	.17					
Average					39	11.2	18.1	.175					
388	.0625	10,000	RT	.39	31	9.7	16.4	.20	402	.1	17.8		
389	.0625	10,000	RT	.39	34	9.6	16.6	.21	403	.1	16.8		
Average					32.5	9.65	16.5	.205			17.25	1.78	98

† CHS = Crosshead Speed

‡ TF = Trangranular Fracture

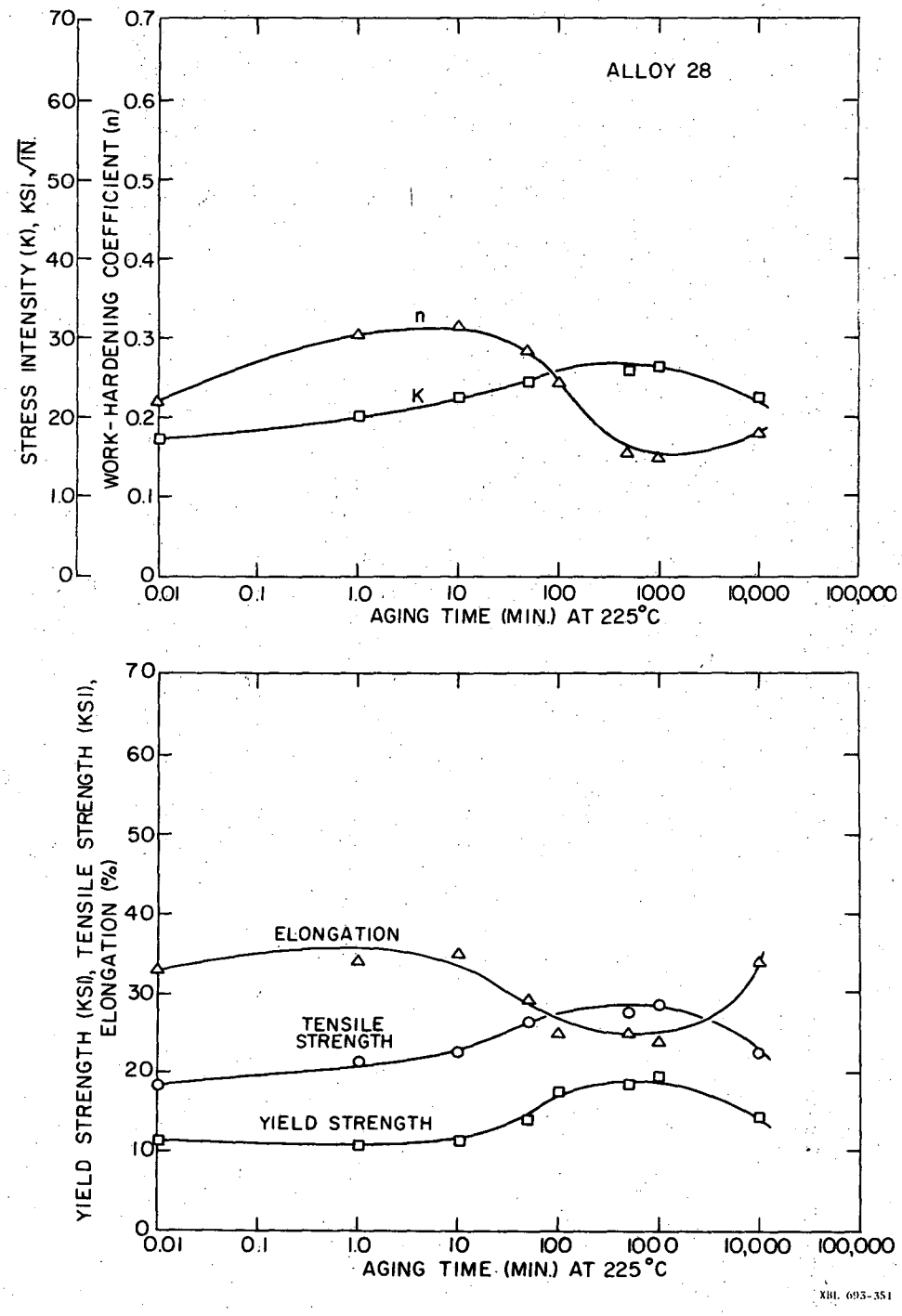

Fig. 19 The mechanical properties of alloy 28 (Al-9.66% Ag) as a function of aging time at 225°C.

Table 12. Mechanical Properties of Alloy 28 (Al - 9.66% Ag).
Solution Treated at 525°C for 60 min., Quenched in Ice Water, and Aged at 225°C.

				Tensile Properties						Fracture Properties				
Test No.	t, in.	Aging time, min.	Test temp, °C	$\dot{\epsilon}$, 1/min.	Elong, %	YS, ksi	UTS, ksi	N	Test No.	CHS†, cm/min.	K, ksi$\sqrt{in.}$	K/S, $\sqrt{in.}$	% TF‡
220	.0625	0	RT	.39	38	10.9	18.3	.22	358	.1	18.9		
221	.0625	0	RT	.39	28	11.3	18.2	.22	359	.1	15.2		
Average					33	11.1	18.25	.22			17.05	1.54	100
222	.0625	1	RT	.39	34	10.8	21.6	.30	360	.1	20.4		
223	.0625	1	RT	.39	33	11.0	21.2	.31	361	.1	20.2		
Average					33.5	10.9	21.4	.305			20.3	1.86	100
224	.0625	10	RT	.39	35	11.1	23.6	.32	362	.1	22.8		
225	.0625	10	RT	.39		11.5	23.9	.31	363	.1	23.0		
Average					35	11.3	23.75	.315			22.9	2.01	100
226	.0625	50	RT	.39	25	15.1	26.9	.27	364	.1	25.8		
227	.0625	50	RT	.39	33	13.0	25.4	.30	365	.1	23.6		
Average					29	14.05	26.15	.285			24.7	1.76	100
228	.0625	100	RT	.39	23	18.0	28.5	.21	366	.1	29.4		
229	.0625	100	RT	.39	27	17.3	28.7	.28	367	.1	27.0		
Average					25	17.65	28.6	.245			28.2	1.60	90
522	.125	100	RT	.39	24	15.6	27.9	.20					
523	.125	100	RT	.39	28	16.0	25.7	.19					
Average					26	15.8	26.8	.195					
230	.0625	500	RT	.39	24	18.0	27.3	.15	368	.1	26.5		
231	.0625	500	RT	.39	26	19.0	28.0	.16	369	.1	24.5		
Average					25	18.5	27.65	.155			25.5	1.38	80
232	.0625	1000	RT	.39	24	19.5	28.7	.15	376	.1	27.2		
233	.0625	1000	RT	.39	24	19.7	28.7	.15	377	.1	25.3		
Average					24	19.6	28.7	.15			26.25	1.34	50
524	.125	1000	RT	.39	35	18.9	26.4	.14					
525	.125	1000	RT	.39	35	17.4	25.3	.15					
Average					35	18.15	25.85	.145					
390	.0625	10,000	RT	.39	32	14.3	22.9	.18	404	.1	21.8		
391	.0625	10,000	RT	.39	35	14.6	22.2	.18	405	.1	23.2		
Average					33.5	14.45	22.55	.18			22.5	1.56	95

† CHS = Crosshead Speed
‡ TF = Transgranular Fracture

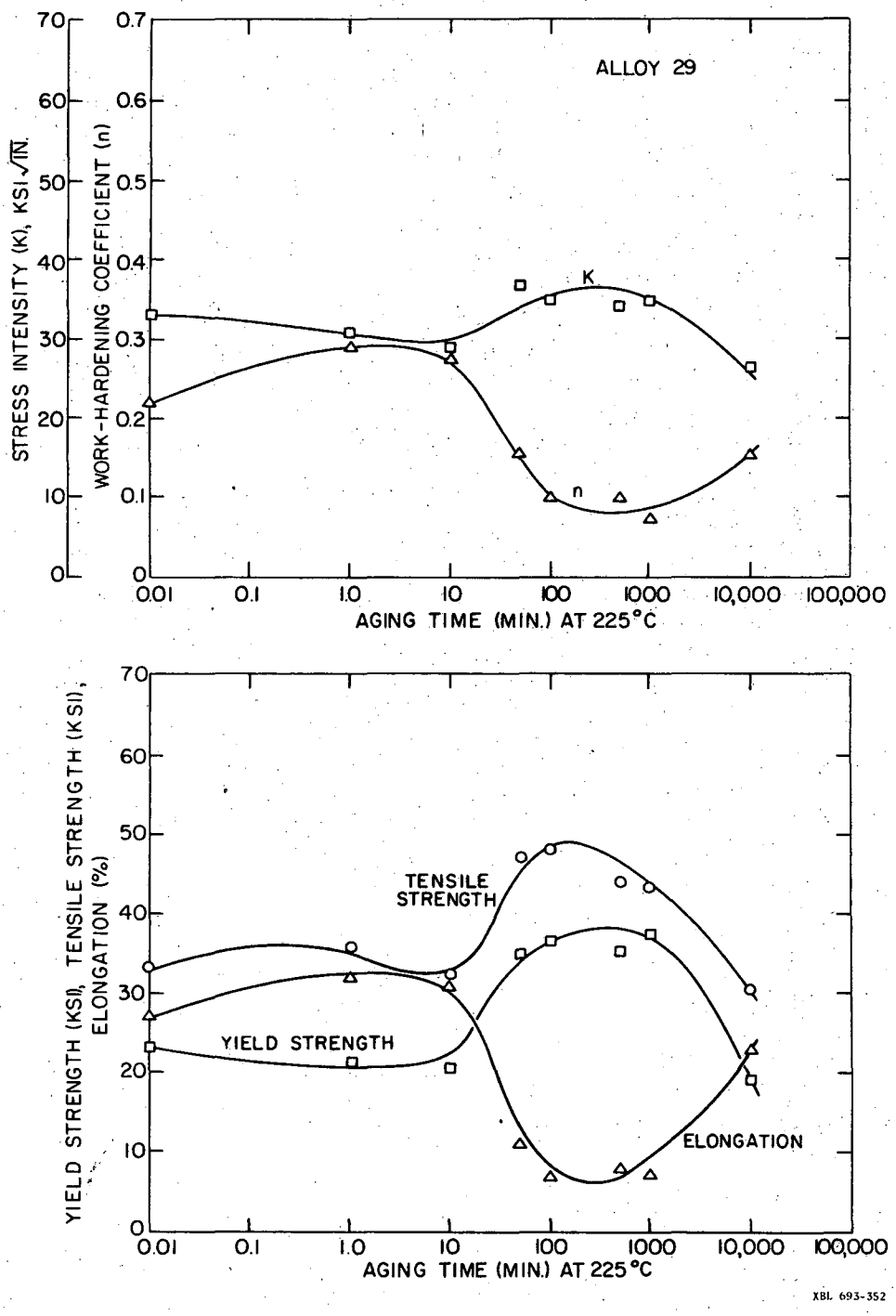

Fig. 20 The mechanical properties of alloy 29 (Al-20.11% Ag) as a function of aging time at 225°C.

Table 13. Mechanical Properties of Alloy 29 (Al - 20.11% Ag).
Solution Treated at 525°C for 60 min., Quenched in Ice Water, and Aged at 225°C.

				Tensile Properties					Fracture Properties				
Test No.	t, in.	Aging time, min.	Test temp, °C	$\dot{\epsilon}$, 1/min.	Elong. %	YS, ksi	UTS, ksi	N	Test No.	CHS†, cm/min.	K, ksi$\sqrt{\text{in.}}$	K/S, $\sqrt{\text{in.}}$	% TF‡
234	.0625	0	RT	.39	26	22.3	31.8	.20	313	.1	34.7		
235	.0625	0	RT	.39	27	24.1	34.7	.24	314	.1	31.5		
Average					26.5	23.2	33.25	.22			33.1	1.48	100
236	.0625	1	RT	.39	33	21.5	35.8	.29	372	.1	30.6		
237	.0625	1	RT	.39	30	21.3	36.0	.29	373	.1	30.7		
Average					31.5	21.4	35.9	.29			30.65	1.44	100
238	.0625	10	RT	.39	30	20.3	32.2	.28	374	.1	29.1		
239	.0625	10	RT	.39	31	21.3	32.2	.27	375	.1	28.2		
Average					30.5	20.8	32.2	.275			28.65	1.38	100
240	.0625	50	RT	.39	8.0	35.8	46.6	.15	315	.1	32.6		
241	.0625	50	RT	.39	14.0	34.4	47.4	.16	316	.1	40.4		
Average					11.0	35.1	47.0	.155			36.5	1.04	20
242	.0625	100	RT	.39	7.0	35.6	46.9	.10	317	.1	32.6		
243	.0625	100	RT	.39	7.0	38.2	49.0	.10	318	.1	36.7		
Average					7.0	36.9	47.95	.10			34.65	.94	10
526	.125	100	RT	.39	7.0	37.6	46.4	.11	538	1.0	41.8		
527	.125	100	RT	.39	8.0	37.5	46.3	.12	544		43.8		
Average					7.5	37.55	46.35	.115			42.8		
437 *	.0625	100	RT	.39	6.3	37.6	45.3	.10					
438 *	.0625	100	RT	.39	4.0	42.4	47.2	.09					
436 **	.0625	100	RT	.39	6.3	36.5	45.6	.11					
435	.0625	100	RT	.0039	6.0	37.6	45.8	.09					
434	.0625	100	RT	3.9	7.9	39.2	45.7	.13					
421	.0625	100	LN_2	.0039	9.0	36.8	53.6	.10					
420	.0625	100	LN_2	.39	8.0	46.7	56.0	.09					
244	.0625	500	RT	.39	8.0	35.6	45.0	.11	319	.1	34.5		
245	.0625	500	RT	.39	8.0	34.9	43.0	.09	320	.1	33.3		
Average					8.0	35.25	44.0	.10			33.9	.96	5
246	.0625	1000	RT	.39	8.0	35.7	43.4	.09	370	.1	33.6		
247	.0625	1000	RT	.39	5.0	38.9	43.1	.06	371	.1	35.8		
Average					6.5	37.3	43.25	.075			34.7	.93	0
528	.125	1000	RT	.39	12.0	32.5	40.0	.11	539	1.0	no meaningful data		
529	.125	1000	RT	.39	12.0	32.5	40.0	.11	545	1.0			
Average					12.0	32.5	40.0	.11					
392	.0625	10,000	RT	.39	24	19.0	29.9	.16	409	.1	26.4		
393	.0625	10,000	RT	.39	22	19.1	31.1	.15	410	.1	26.0		
Average					23	19.05	30.5	.155			26.2	1.38	10

* 437 Solution treated for 1000 min. at 525°C, quenched in ice water and aged at 225°C
438 Solution treated for 4400 min. at 525°C, quenched in ice water, and aged at 225°C

** 436 Solution treated, quenched in ice water, deformed 6% by cold rolling, and aged at 225°C

† CHS = Crosshead Speed

‡ TF = Transgranular Fracture

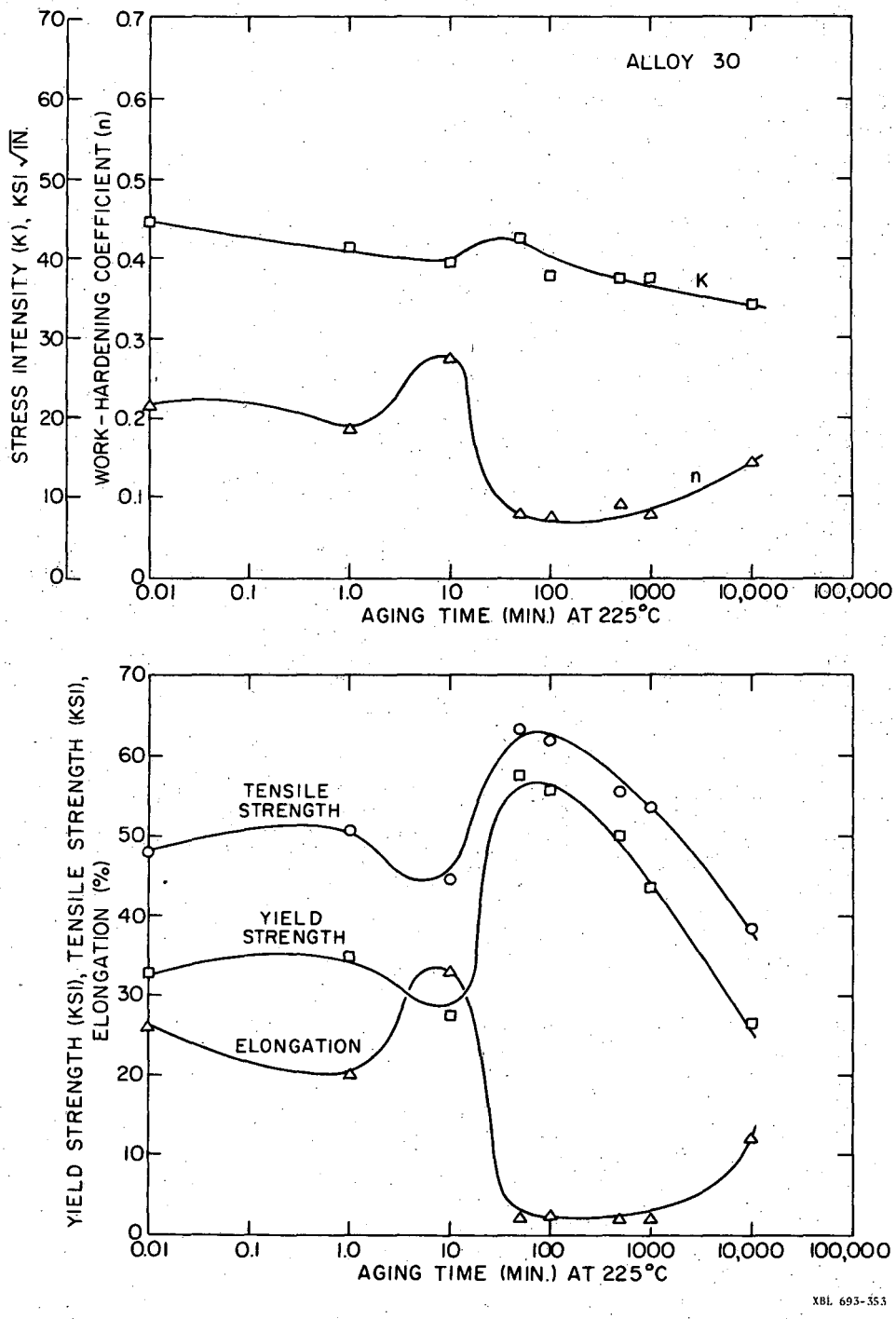

Fig. 21 The mechanical properties of alloy 30 (Al-28.6% Ag) as a function of aging time at 225°C.

Table 14. Mechanical Properties of Alloy 30 (Al-28.6%)
Solution Treated at 525°C for 60 min., Quenched in Ice Water, and Aged at 225°C.

				Tensile Properties						Fracture Properties				
Test No.	t, in.	Aging time, min.	Test temp., °C	ε̇, 1/min.	Elong. %	YS, ksi	UTS, ksi	N	Test No.	CHS†, cm/min.	K, ksi√in.	K/YS, √in.	% TF‡
248	.0625	0	RT	.39	26	32.2	45.9	.21	299	.1	44.5		
249	.0625	0	RT	.39	25	32.5	50.0	.22	300	.1	44.2		
Average					25.5	32.35	47.95	.215			44.35	1.37	75
250	.0625	1	RT	.39	20	35.6	51.7	.17	301	.1	40.5		
251	.0625	1	RT	.39	20	34.4	49.7	.20	302	.1	41.8		
Average					20	35.0	50.7	.185			41.15	1.18	90
252	.0625	10	RT	.39	33	27.1	43.8	.27	303	.1	38.2		
253	.0625	10	RT	.39	32	27.2	45.0	.28	304	.1	40.1		
Average					32.5	27.15	44.4	.275			39.15	1.44	100
254	.0625	50	RT	.39	1	60.1	64.2	.06	305	.1	43.3		
255	.0625	50	RT	.39	2	55.4	62.7	.10	306	.1	41.3		
Average					1.5	57.75	63.45	.08			42.3	.73	0
256	.0625	100	RT	.39	2	55.3	61.7	.07	307	.1	37.0		
257	.0625	100	RT	.39	1	56.6	62.3	.08	308	.1	37.9		
Average					1.5	55.95	62.0	.075			37.45	.67	0
530	.125	100	RT	.39	2	59.9	62.0	.06	540	1.0	37.4		
531	.125	100	RT	.39	2	60.9	62.3	.04	546	1.0	43.3		
Average					2	60.4	62.15	.05			40.35		
258	.0625	500	RT	.39	2	49.7	54.5	.11	309	.1	36.0		
259	.0625	500	RT	.39	2	50.1	56.2	.07	310	.1	38.3		
Average					2	49.9	55.35	.09			37.15	.75	0
260	.0625	1000	RT	.39	2	42.1	51.7	.07	311	.1	35.0		
261	.0625	1000	RT	.39	2	45.5	55.4	.07	312	.1	39.6		
Average					2	43.8	53.55	.07			37.3	.85	0
532	.125	1000	RT	.39	4	51.3	54.8	.06	541	1.0	46.0		
533	.125	1000	RT	.39	3	50.2	53.0	.07	547	1.0	43.0		
Average					3.5	50.75	53.9	.065			44.5		
394	.0625	10,000	RT	.39	12	27.1	38.1	.15	411	.1	33.5		
395	.0625	10,000	RT	.39	11	26.6	38.1	.14	412	.1	34.5		
Average					11.5	26.85	38.1	.145			34.0	1.27	0

† CHS = Crosshead Speed

‡ TF = Transgranular Fracture

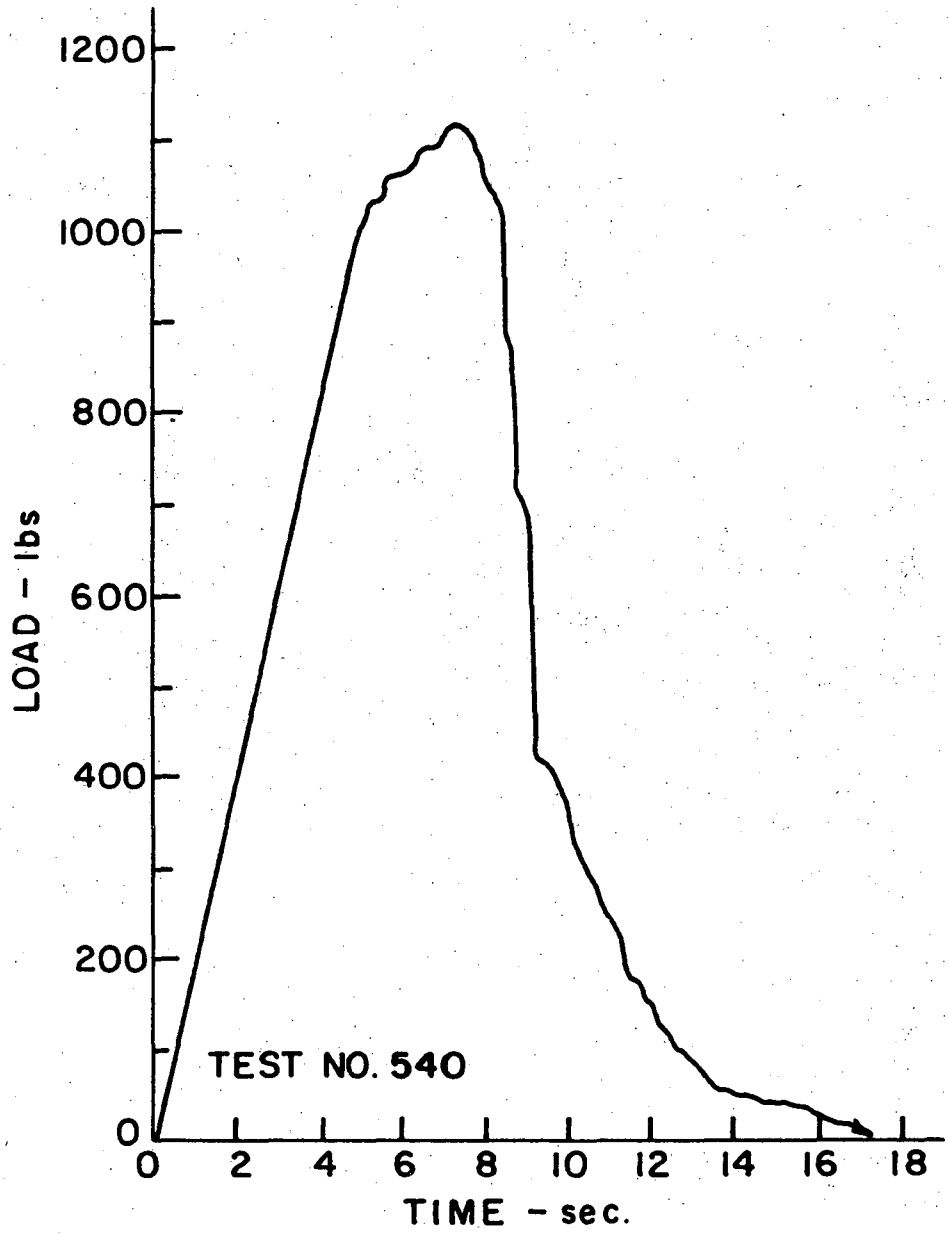

XBL 691-113

Fig. 22 Load versus time record for a large SEN fracture specimen of alloy 30, solution treated and aged for 100 min. at 225°C. Tested at 0.39 in./min.

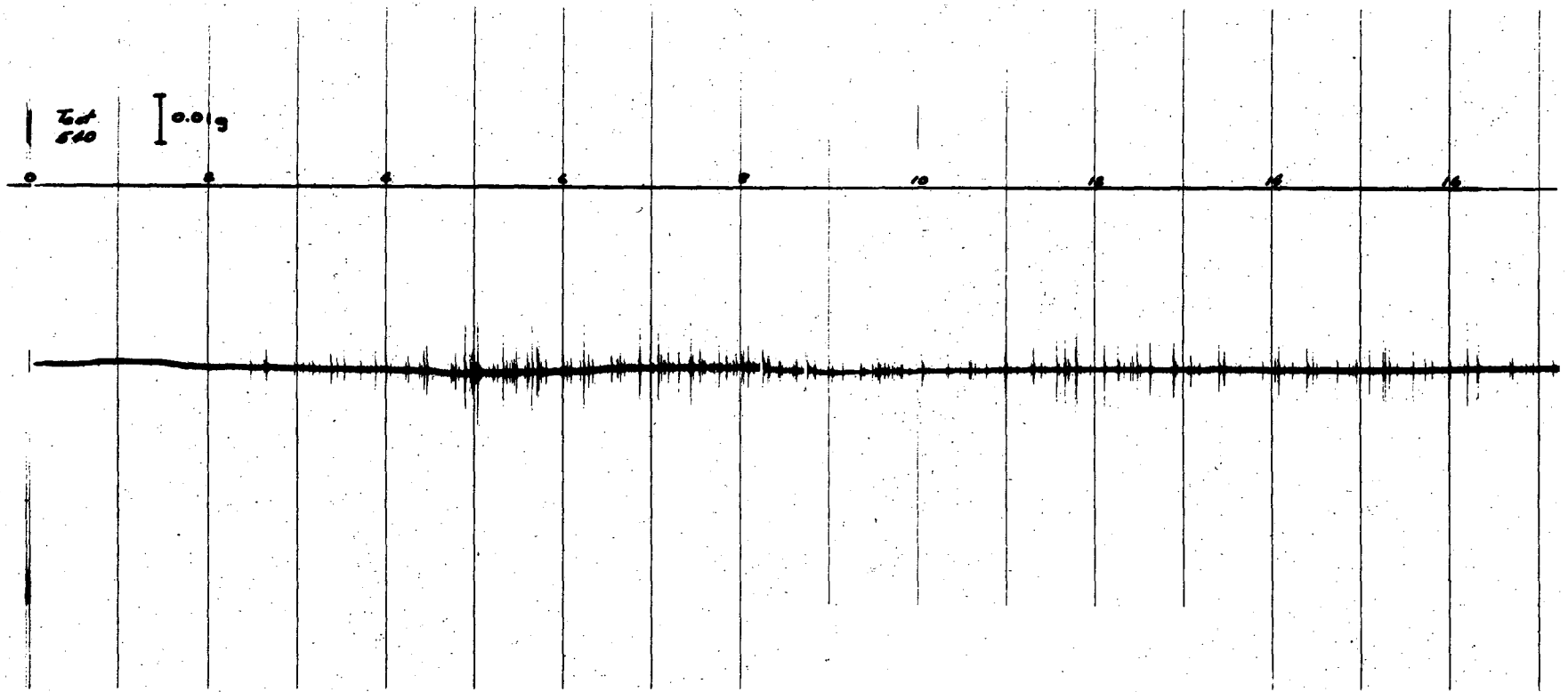

XBL 691-44

Fig. 23 Oscillogram of stress-waves corresponding to Fig. 22. The time lines are 1 sec. apart and the approximate total time (secs.) is given along the top line.

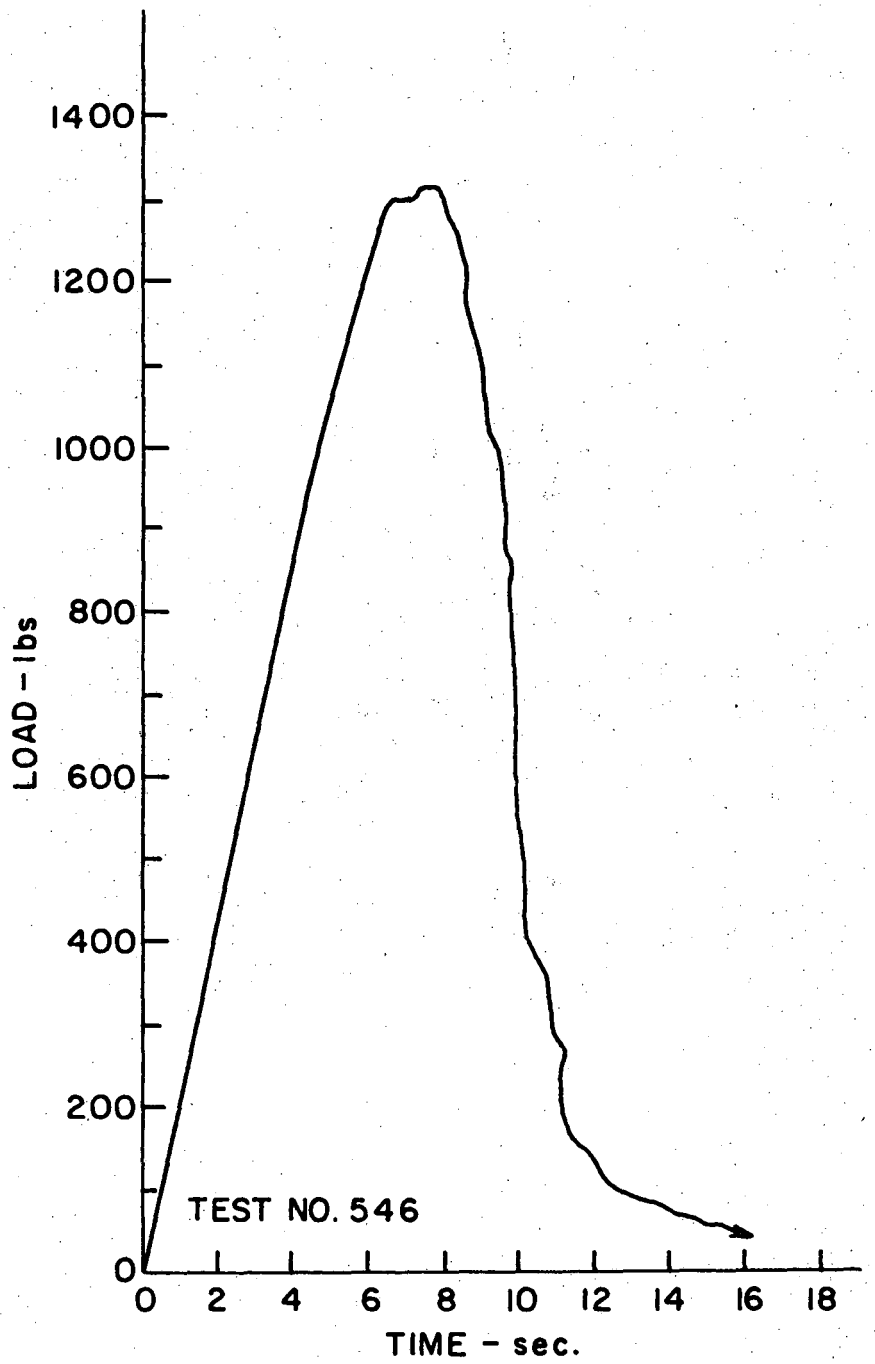

XBL 691-114

Fig. 24 Load versus time record for a large SEN fracture specimen of alloy 30, solution treated and aged for 100 min. at 225°C. Tested at 0.39 in./min.

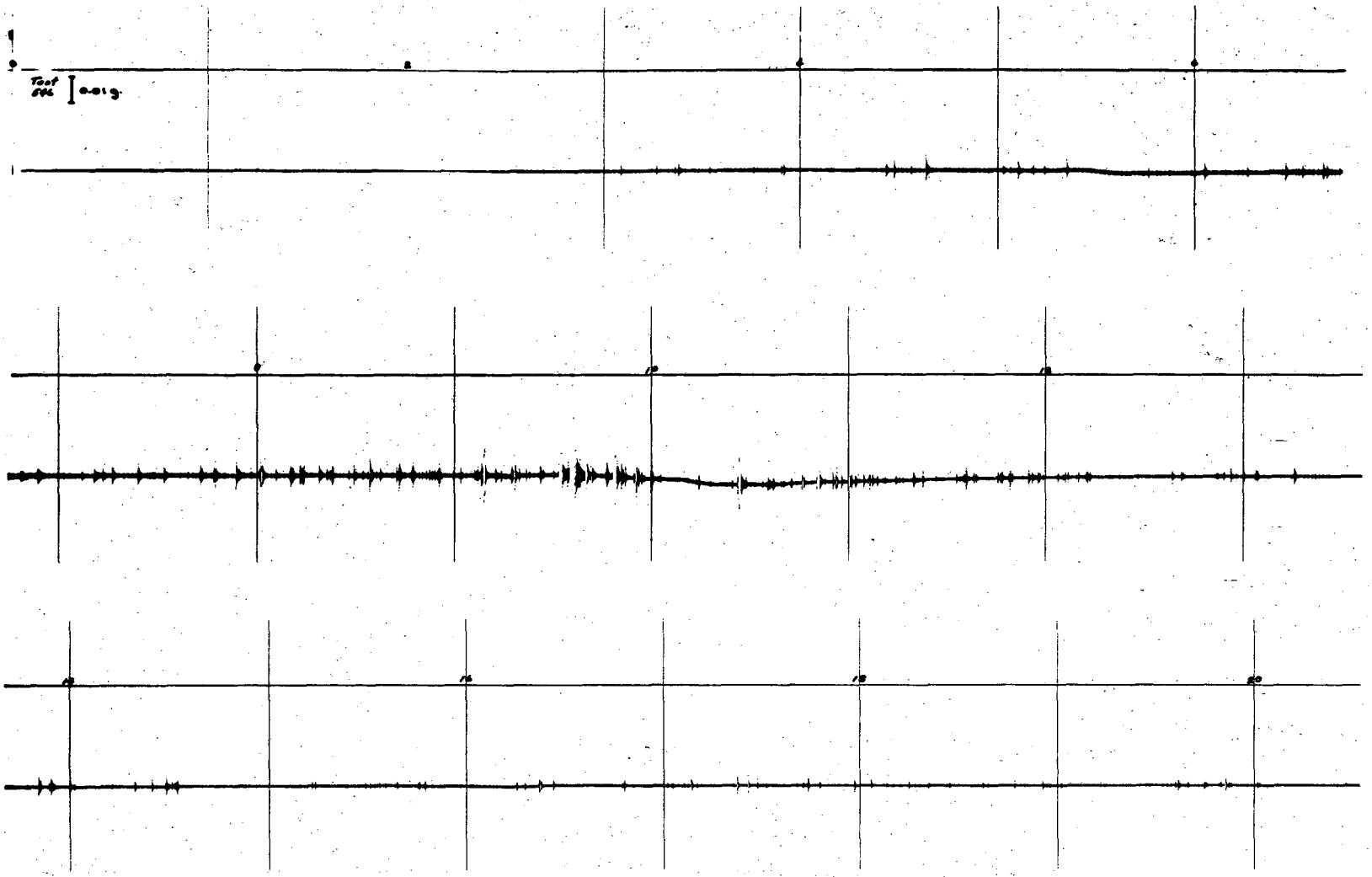

XBL 691-45

Fig. 25 Oscillogram of stress-waves corresponding to Fig. 24. The time lines are 1 sec. apart and the approximate total time (secs.) is given along the top line.

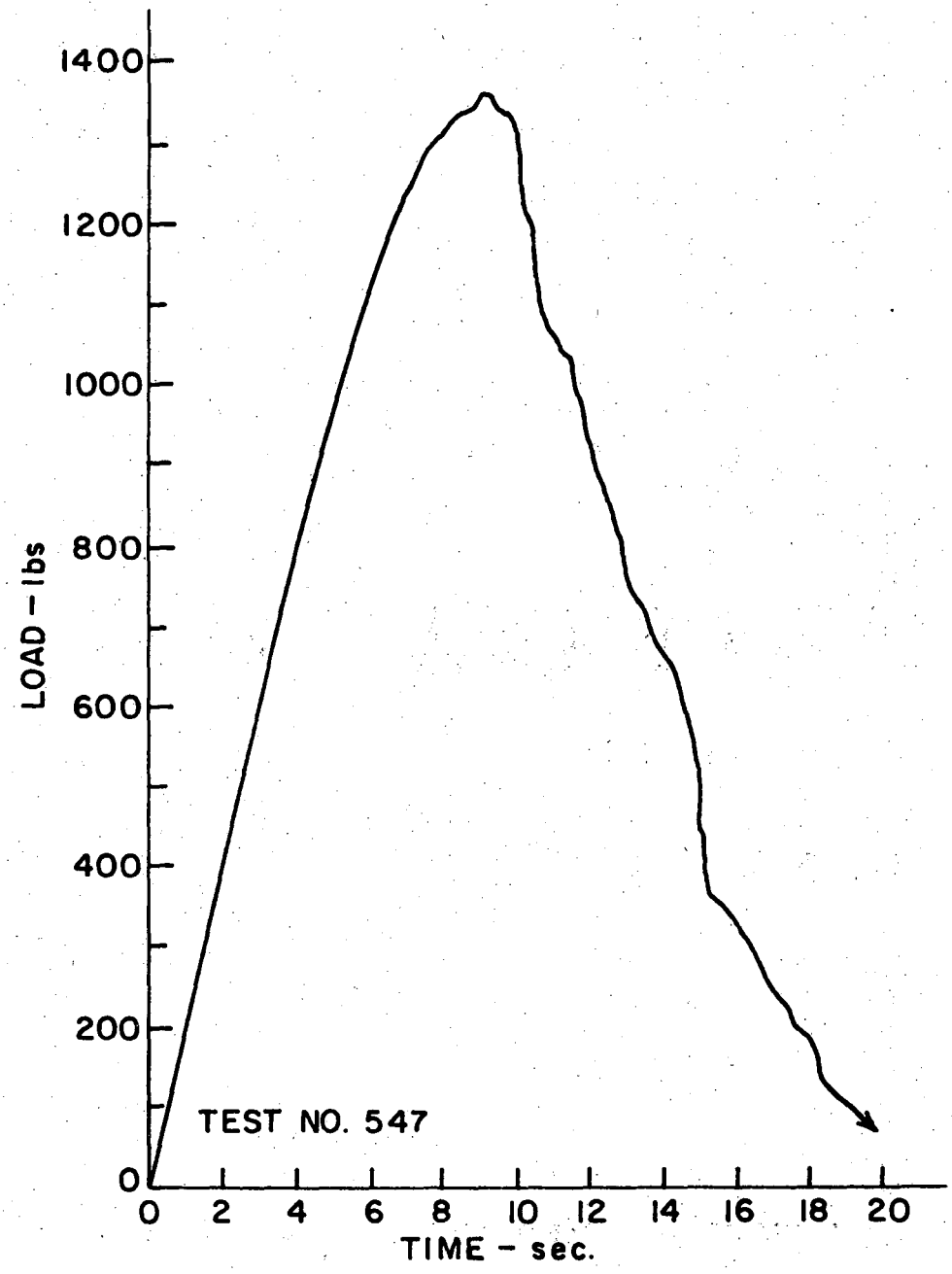

XBL 691-115

Fig. 26 Load versus time record for a large SEN fracture specimen of alloy 30, solution treated and aged for 1000 min. at 225°C. Tested at 0.39 in./min.

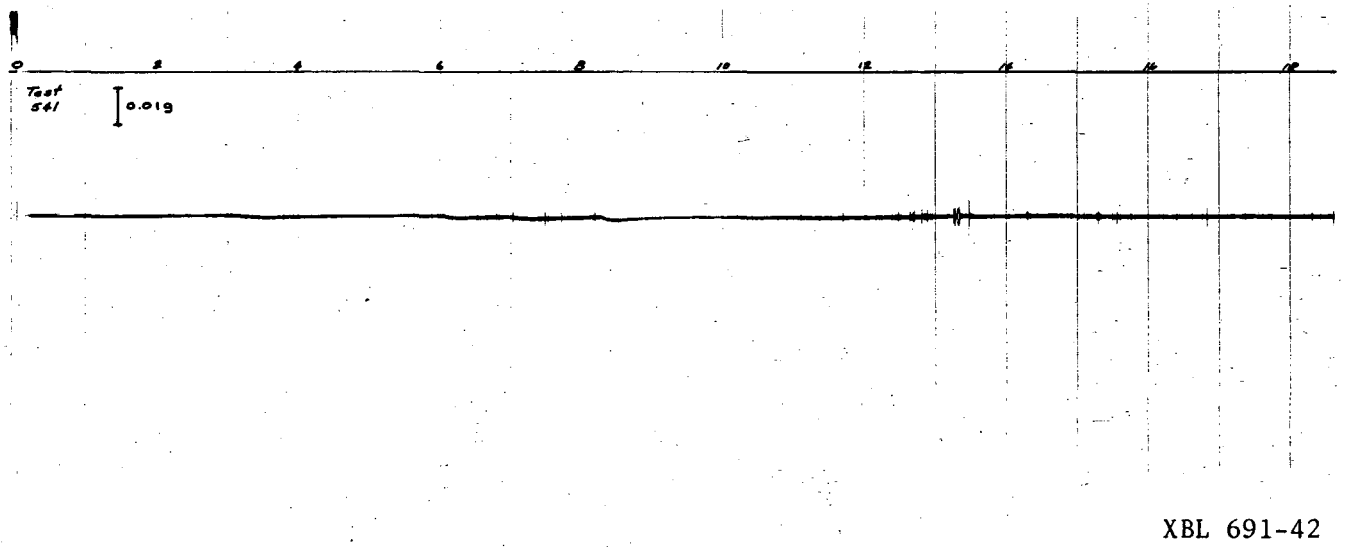

XBL 691-42

Fig. 27 Oscillogram of stress-waves for a large SEN fracture specimen of alloy 30, solution treated and aged for 1000 min. at 225°C. Tested at 0.39 in./min.

D. Metallography

1. Experimental

Metallographic samples were prepared by wet grinding in several stages to a finish equivalent to number 600 paper. The samples were then electropolished and photographed with either an optical or scanning electron microscope. The electropolish used for aluminum-zinc alloys was 2% perchloric acid in methyl alcohol and the operation was carried out at -55°C with a potential of 45 volts. Similary the electropolishing of aluminum-silver alloys was carried out using a solution of 2% perchloric acid in ethyl alcohol at -30°C and a potential of 30 volts. A troublesome anodic film sometimes formed on the surface of the aluminum-silver specimens and this was removed with 5% aqueous solution of sodium dichromate held at 90°C. This anodic film removal took only seconds and did not seem to change the microstructure significantly.

Transmission electron microscopy was carried out on material that had been rolled to 0.005 in. thickness. The foils were heat treated then electropolished using the window technique[22] with the same basic solutions and conditions described for surface metallography.

2. Metallographic Observations

Representative micrographs for the aluminum-zinc system are shown in Figs. 28 to 34. Similar micrographs for the aluminum-silver system are shown in Figs. 35 to 40.

E. Fractography

1. Experimental

The fracture surfaces representative of various aging times were routinely studied using a scanning optical microscope for extreme depth of field

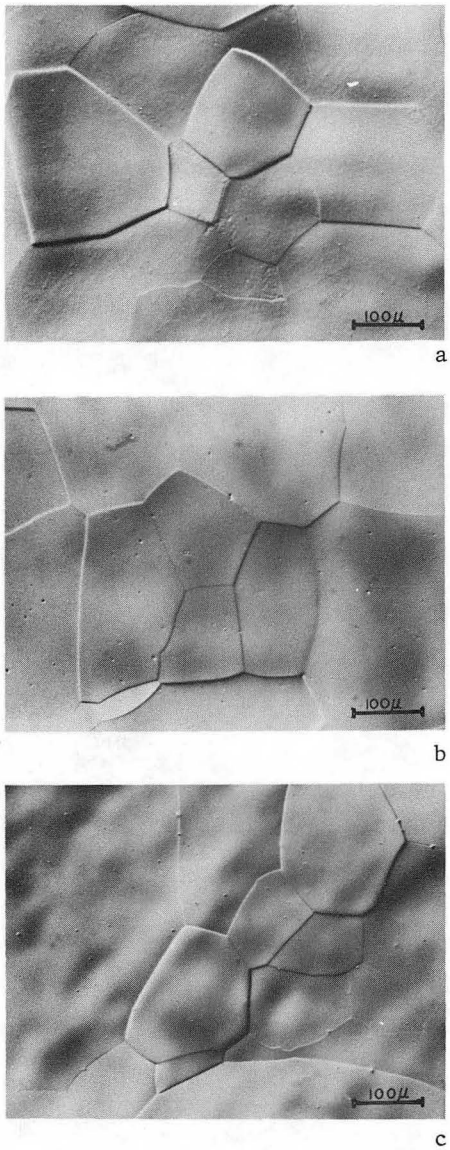

XBB 691-465

Fig. 28 Optical micrographs of alloy 22, solution treated and aged:

(a) 30 min. at room temperature.
(b) 1000 min. at 125°C
(c) 10,000 min. at 125°C.

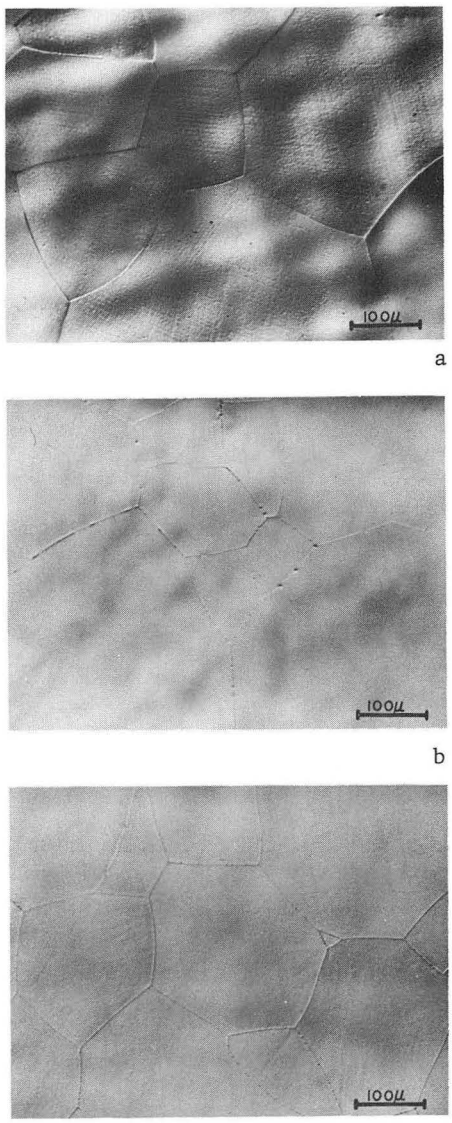

XBB 691-475

Fig. 29 Optical micrographs of alloy 23, solution treated and aged:

(a) 30 min. at room temperature.
(b) 1000 min. at 125°C.
(c) 10,000 min. at 125°C.

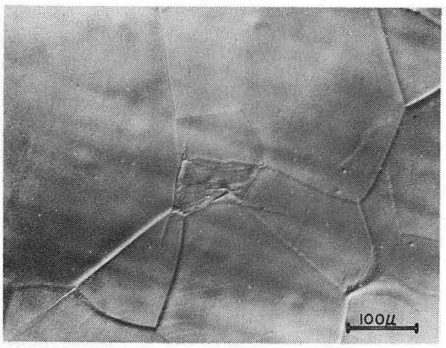

a

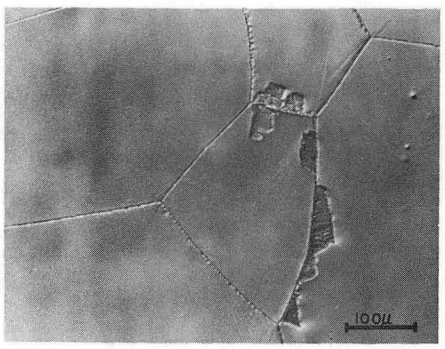

b

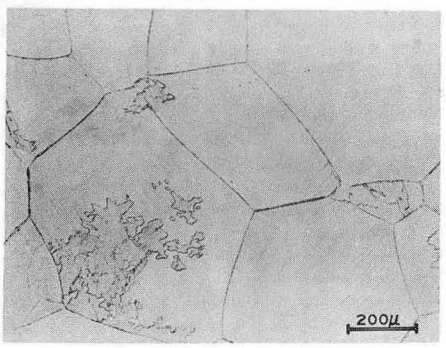

c

XBB 691-474

Fig. 30 Optical micrographs of alloy 24, solution treated and aged:

(a) 30 min. at room temperature.
(b) 1000 min. at 125°C
(c) 10,000 min. at 125°C

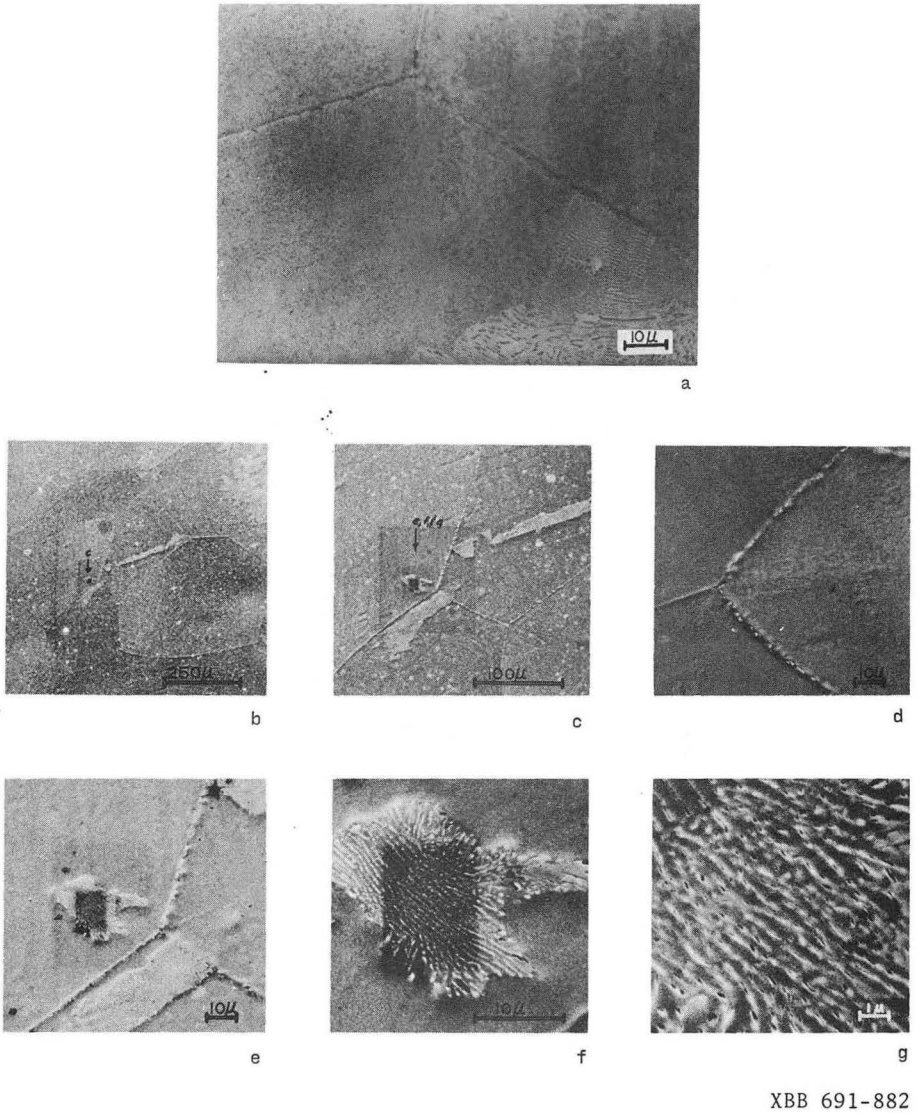

XBB 691-882

Fig. 31 Micrographs of alloy 24 in overaged condition (10,000 min. at 125°C).

(a) optical micrograph
(b) to (g) scanning electron micrographs of the same area with increasing magnification. The dark areas are caused from the electron beam breaking down the oil contaminated onto the surface of specimen.

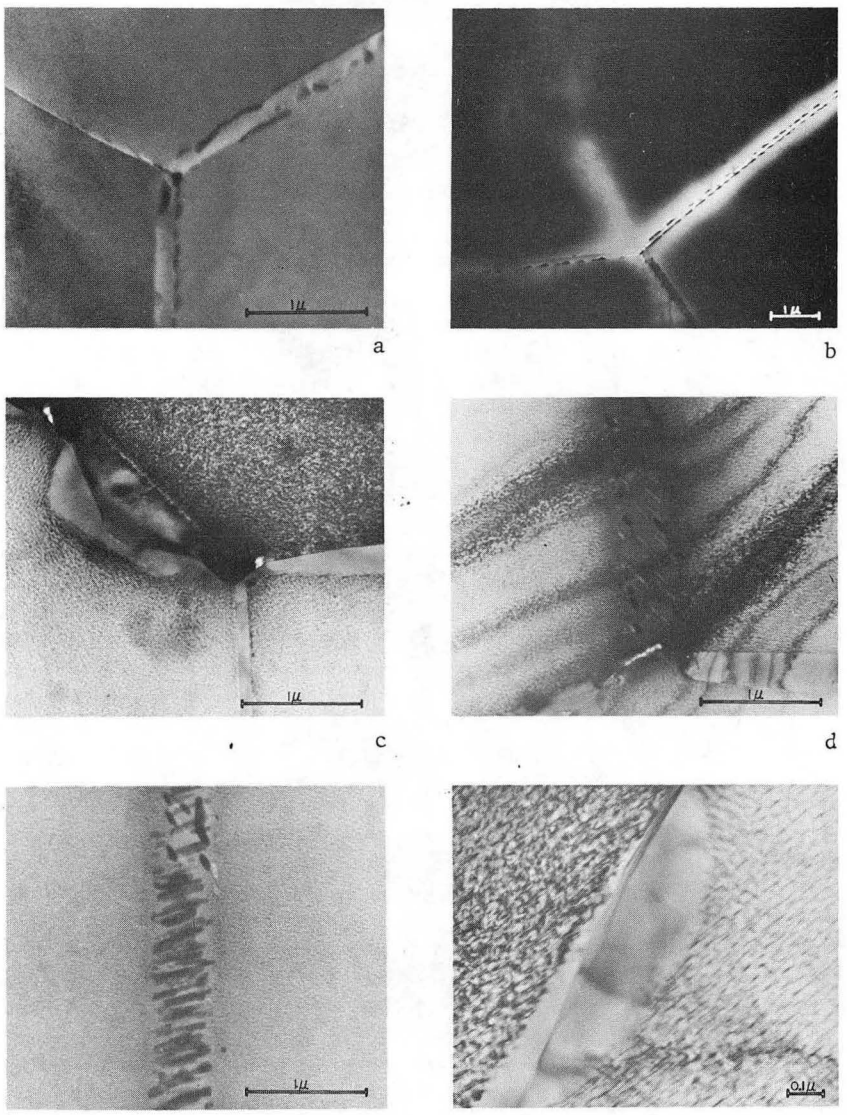

XBB 691-470

Fig. 32 Transmission electron micrographs of alloy 24, solution treated and aged:

(a) and (b) 30 min. at room temperature.
(c) to (f) 1000 min. at 125°C.

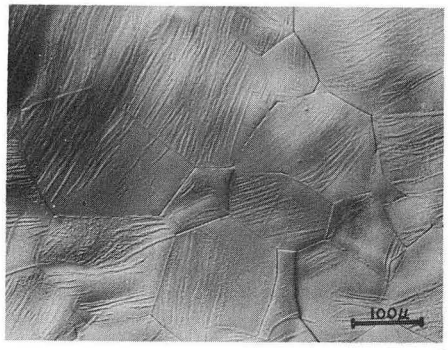

a

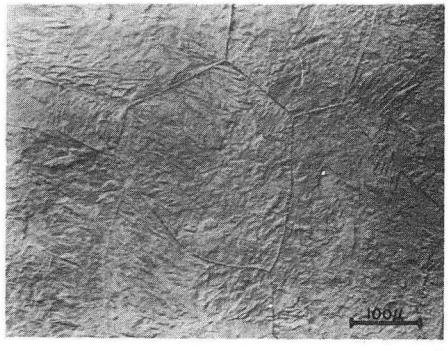

b

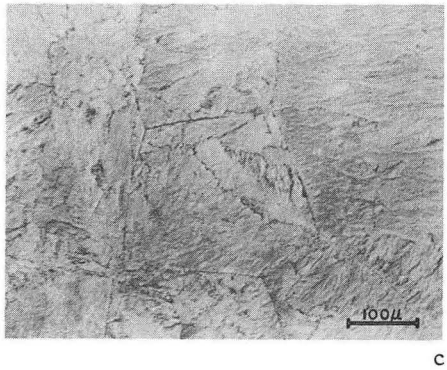

c

XBB 691-471

Fig. 33 Optical micrographs of alloy 25, solution treated and aged:

(a) 30 min. at room temperature.
(b) 1000 min. at 125°C.
(c) 10,000 min. at 125°C.

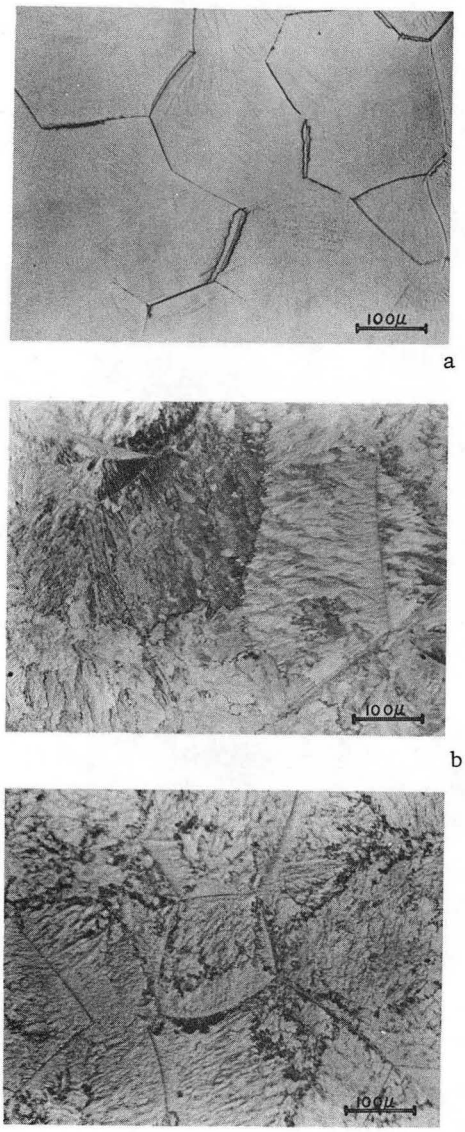

XBB 691-464

Fig. 34 Optical micrographs of alloy 26, solution treated and aged:

(a) 30 min. at room temperature.
(b) 1000 min. at 125°C.
(c) 10,000 min. at 125°C

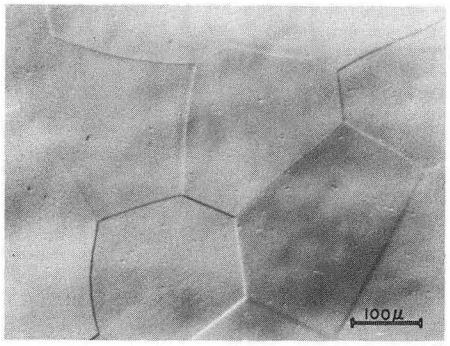

a

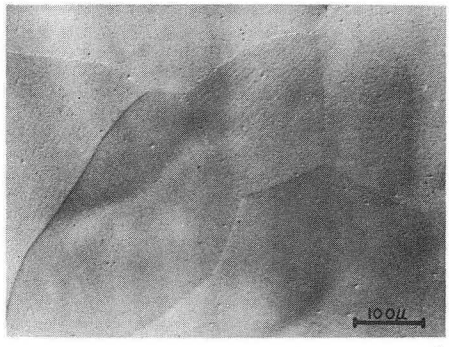

b

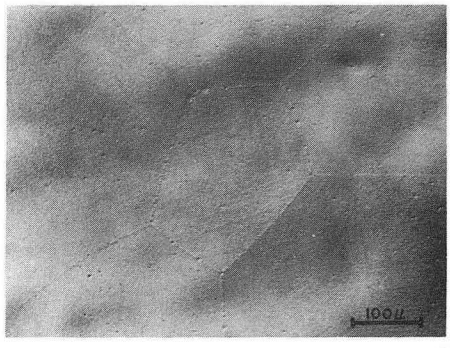

c

XBB 691-478

Fig. 35 Optical micrographs of alloy 27, solution treated and aged:

(a) 30 min. at room temperature.
(b) 1000 min. at 225°C.
(c) 10,000 min. at 225°C.

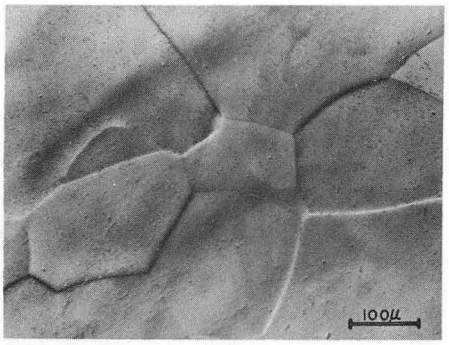

a

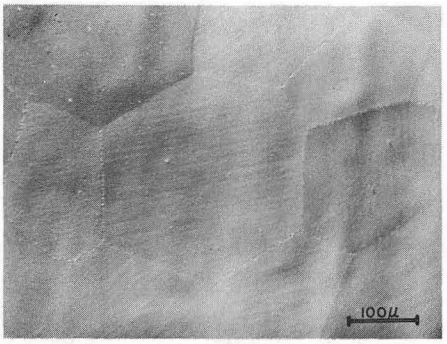

b

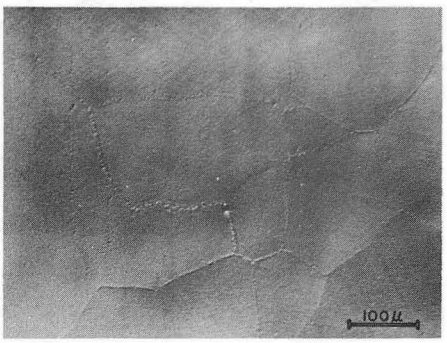

c

XBB 691-473

Fig. 36 Optical micrographs of alloy 28, solution treated and aged:

(a) 30 min. at room temperature.
(b) 1000 min. at 225°C.
(c) 10,000 min. at 225°C.

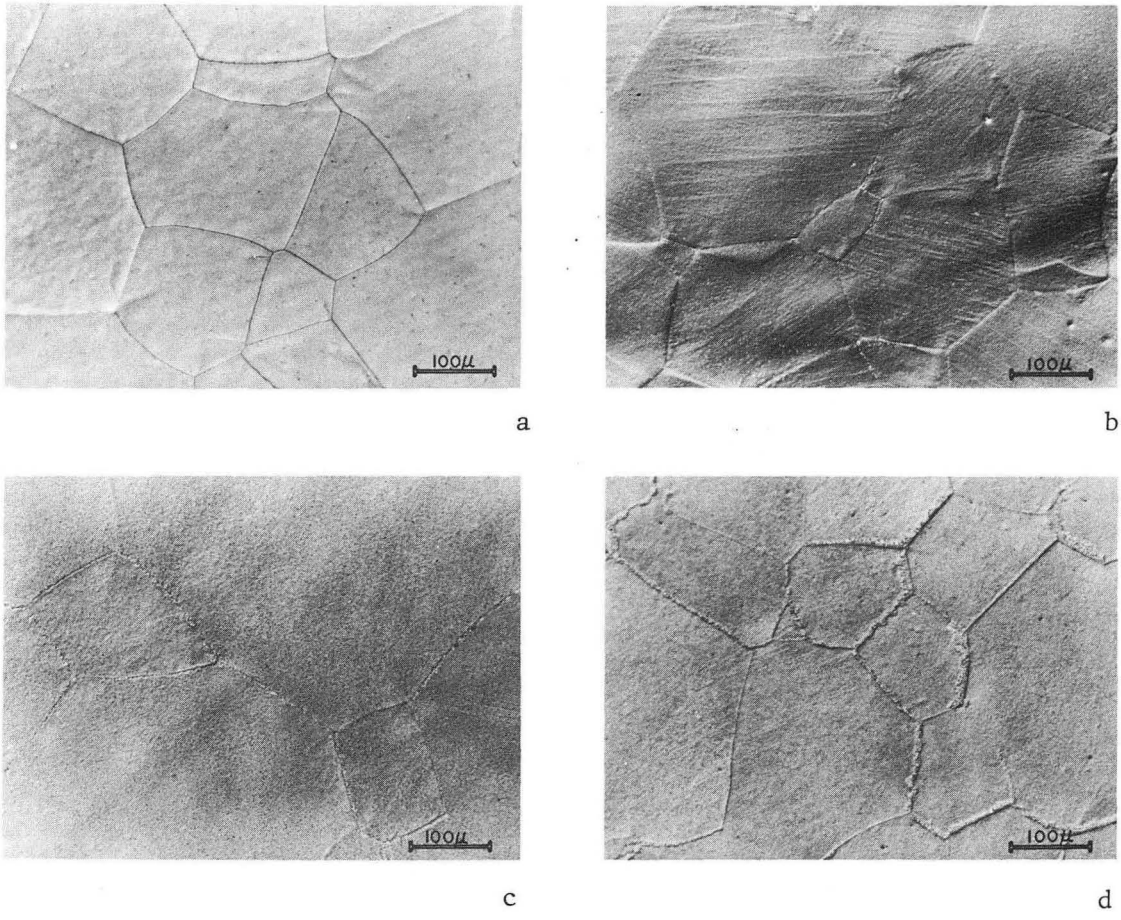

a b

c d

XBB 691-469

Fig. 37 Optical micrographs of alloy 29, solution treated and aged:

(a) 30 min. at room temperature.
(b) 100 min. at 225°C.
(c) 1000 min. at 225°C.
(d) 10,000 min. at 225°C.

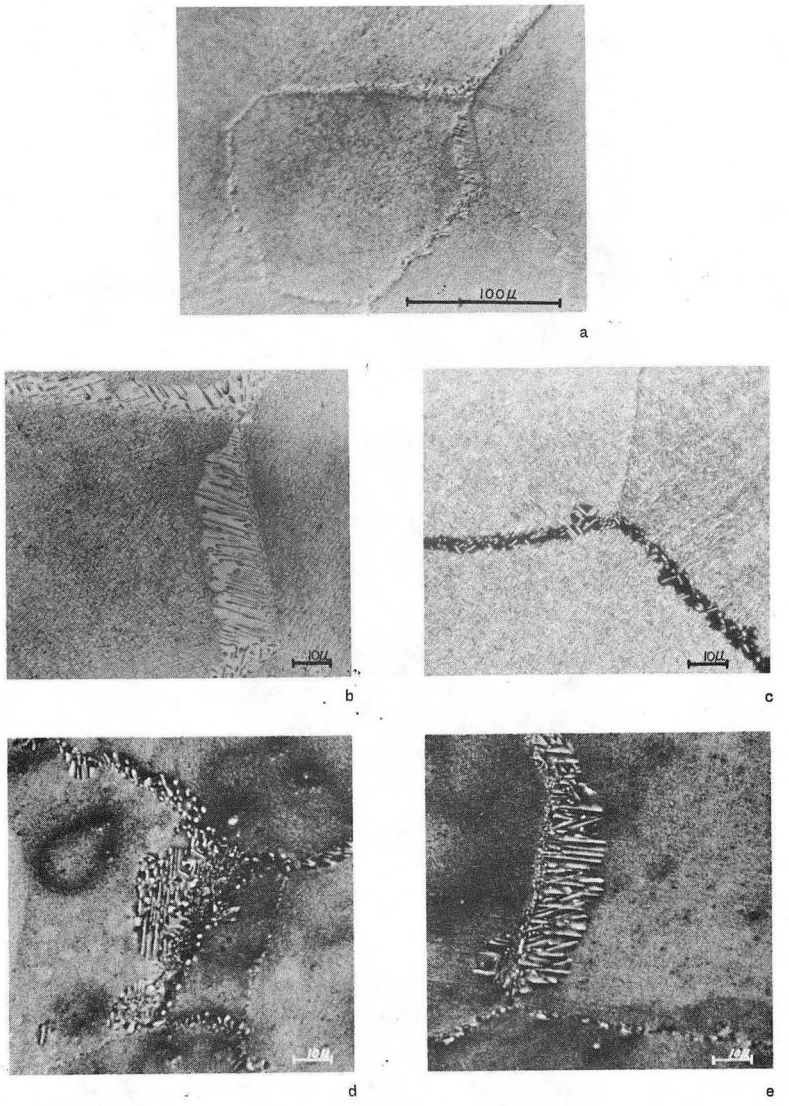

Fig. 38 Micrographs of alloy 29 in the overaged condition (10,000 min at 225°C):

(a) to (c) optical micrographs.
(d) and (e) scanning electron micrographs.

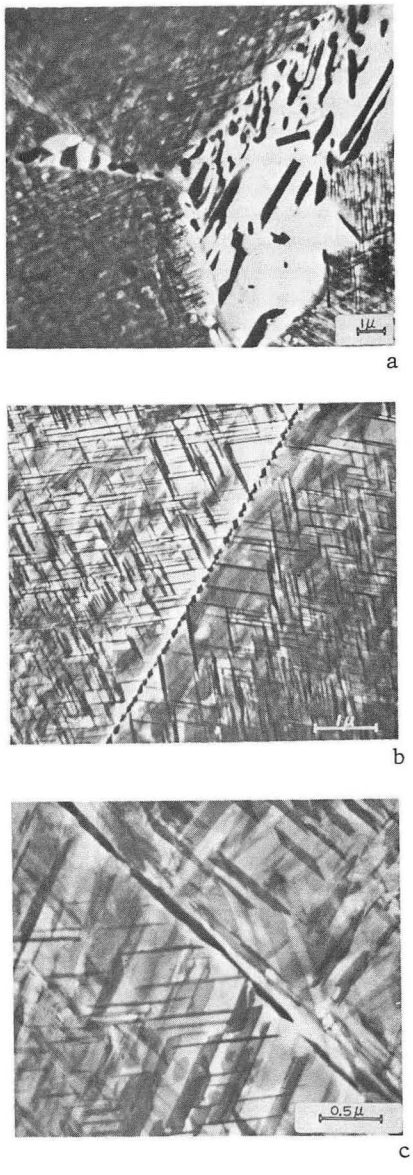

XBB 691-466

Fig. 39 Transmission electron micrographs of alloy 29, solution and aged for 1000 min. at 225°C.

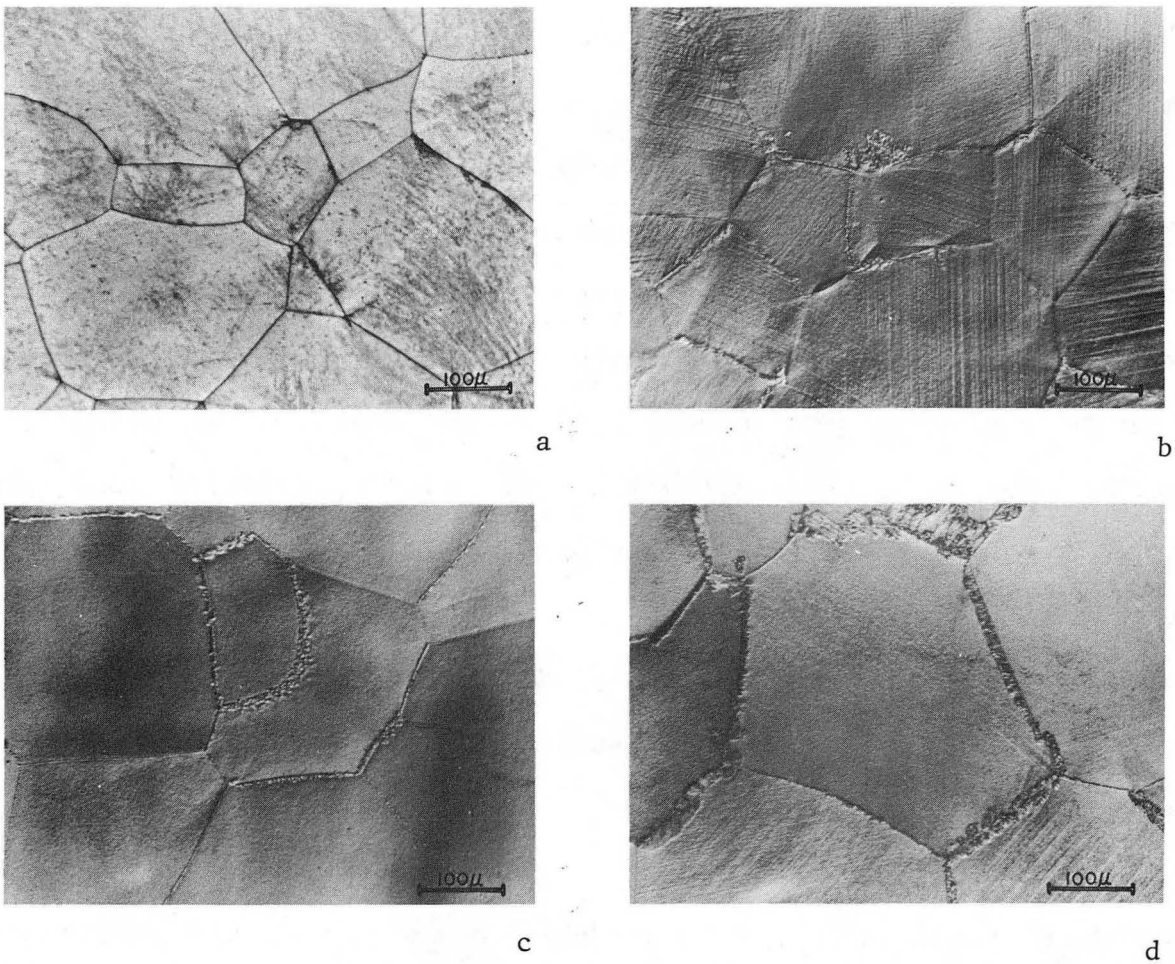

a b c d

XBB 691-472

Fig. 40 Optical micrographs of alloy 30, solution treated and aged:

(a) 30 min. at room temperature.
(b) 100 min. at 225°C.
(c) 1000 min. at 225°C.
(d) 10,000 min. at 225°C.

photography. A Ziess ultraphot metallograph was set up so that a sample could be scanned along the optical axis of the metallograph (with the surface to be viewed tilted to this axis). A highly collimated beam of light was placed at the focal point of the optic system, normal to the optic axis. The sample is scanned with respect to the collimated light and only that portion of the sample that is in focus is illuminated and recorded. For further information on this technique, the reader is referred to the work of McLachlan.[23] The major difficulty with this fractographic technique arises from the high reflectivity of metallic fracture surfaces. The incident light may be reflected several times from a rough fracture surface and illuminate areas that are not in focus. This effect coupled with the fact that there is a wide range of light intensity coming from a rough fracture surface tends to degrade the final negative quality. It was found that film with a wide exposure latitude such as Eastman Kodak Tri-X or Royal Pan, developed in Acufine, gave the best results.

The fractographs taken as part of the routine analysis were studied and where additional information was needed a scanning electron microscope was used. (Replica techniques were difficult to use because of the roughness of the fracture surface.) Specimens were cut from the fracture specimens and viewed in a JEOLCO JSM-1 scanning electron microscope. This microscope was operated at 25 KV in the secondary electron mode.

2. Fractographic Observations

Fractography for the aluminum-zinc system can be found in Figs. 41 to 59, while similar observations for the aluminum-silver system can be found in Figs. 60 to 68. The scanning electron micrographs generally have a sequence of "zoom" magnifications, which relate the fine surface structure to the overall fracture appearance.

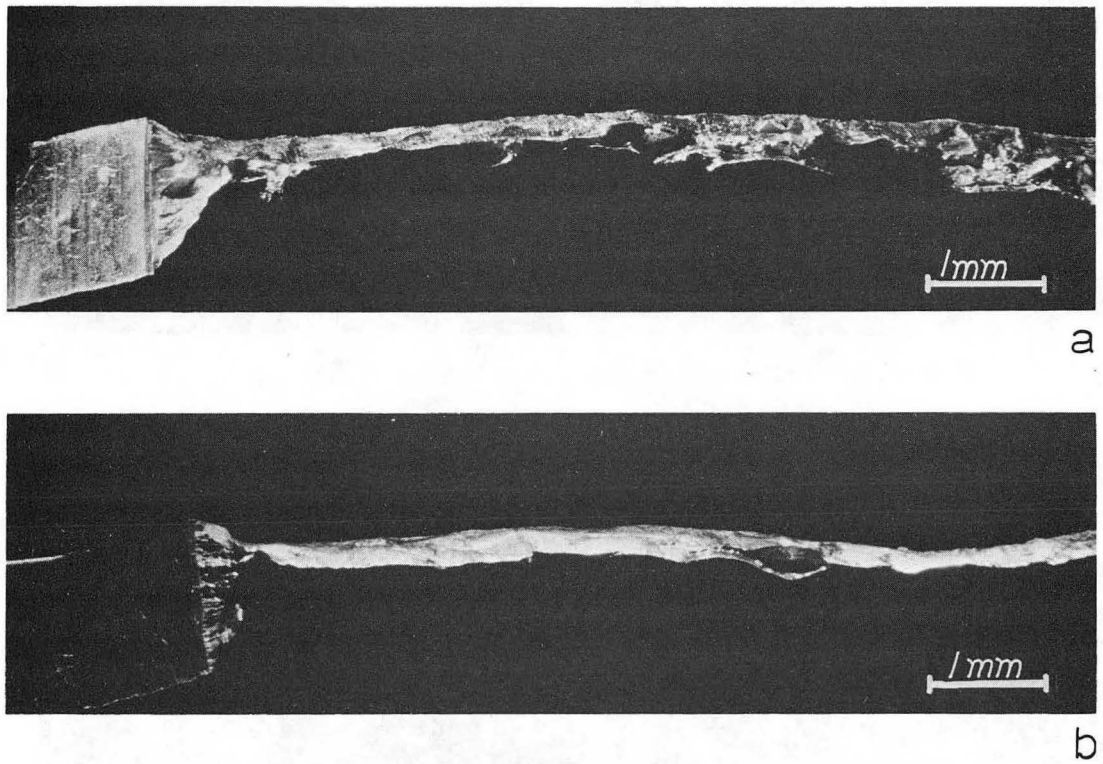

XBB 691-905

Fig. 41 Scanning optical fractographs of alloy 22, solution treated and aged:
(a) 30 min. at room temperature.
(b) 10,000 min. at 125°C.

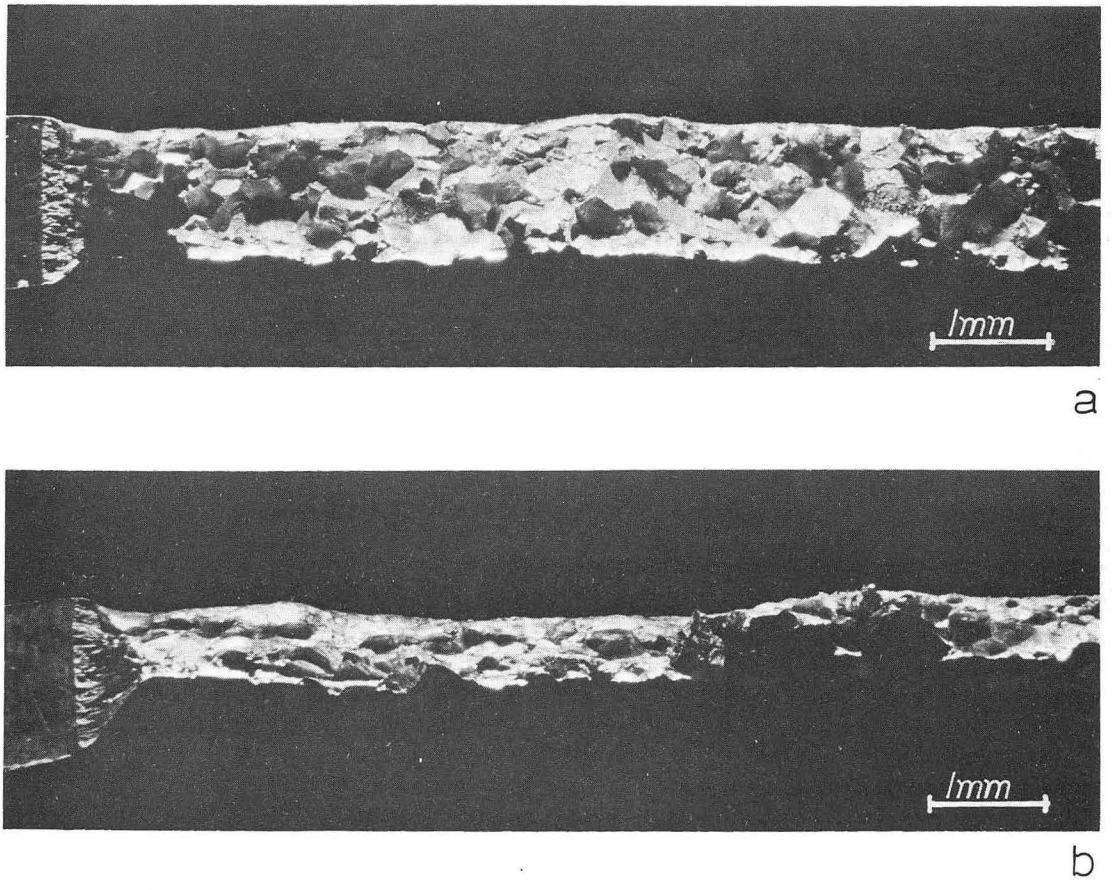

Fig. 42 Scanning optical fractographs of alloy 23, solution treated and aged: (a) 30 min. at room temperature; (b) 10,000 min. at 125°C.

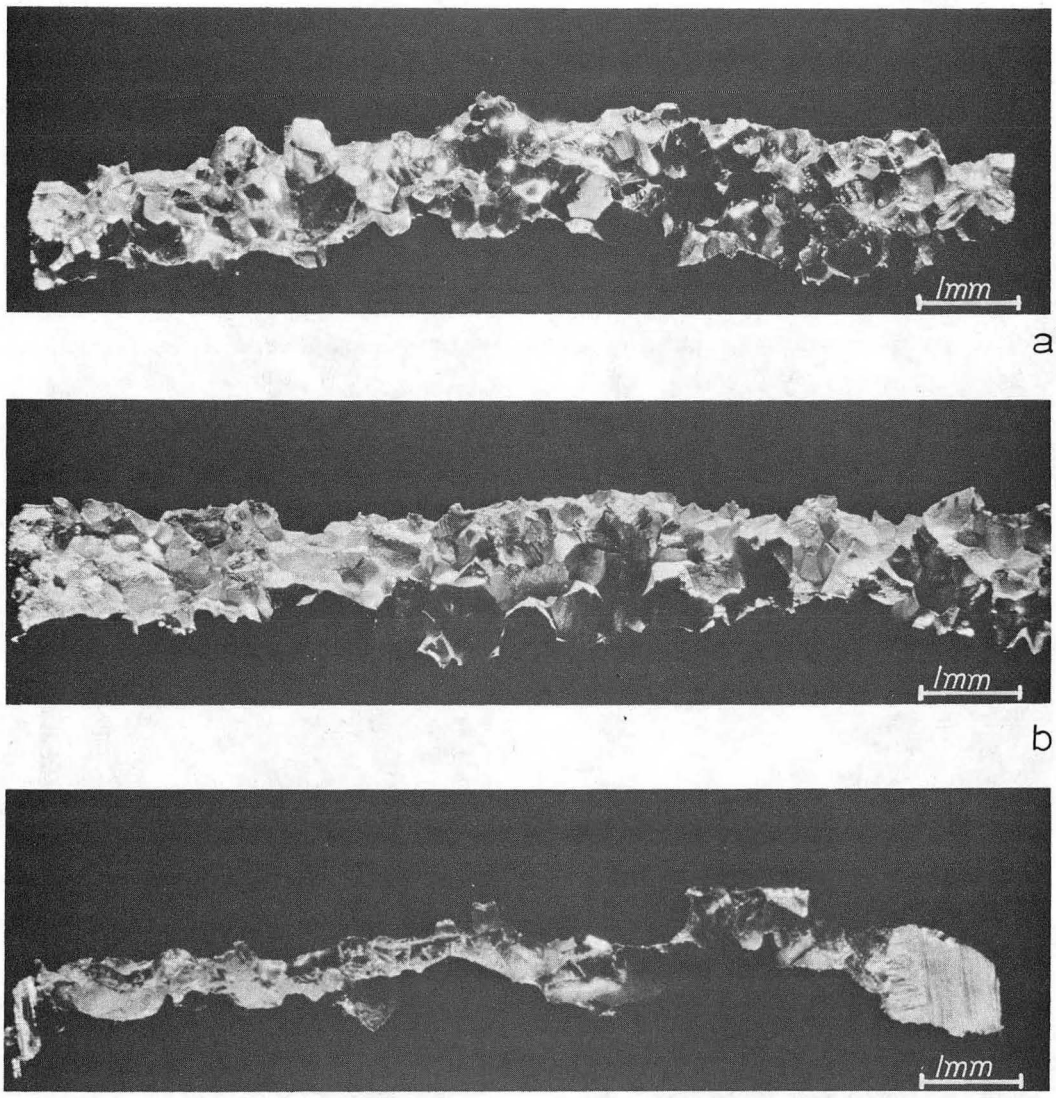

XBB 691-891

Fig. 43 Scanning optical fractographs of alloy 24, solution treated and aged:

(a) 30 min. at room temperature.
(b) 1000 min. at 125°C.
(c) 10,000 min. at 125°C.

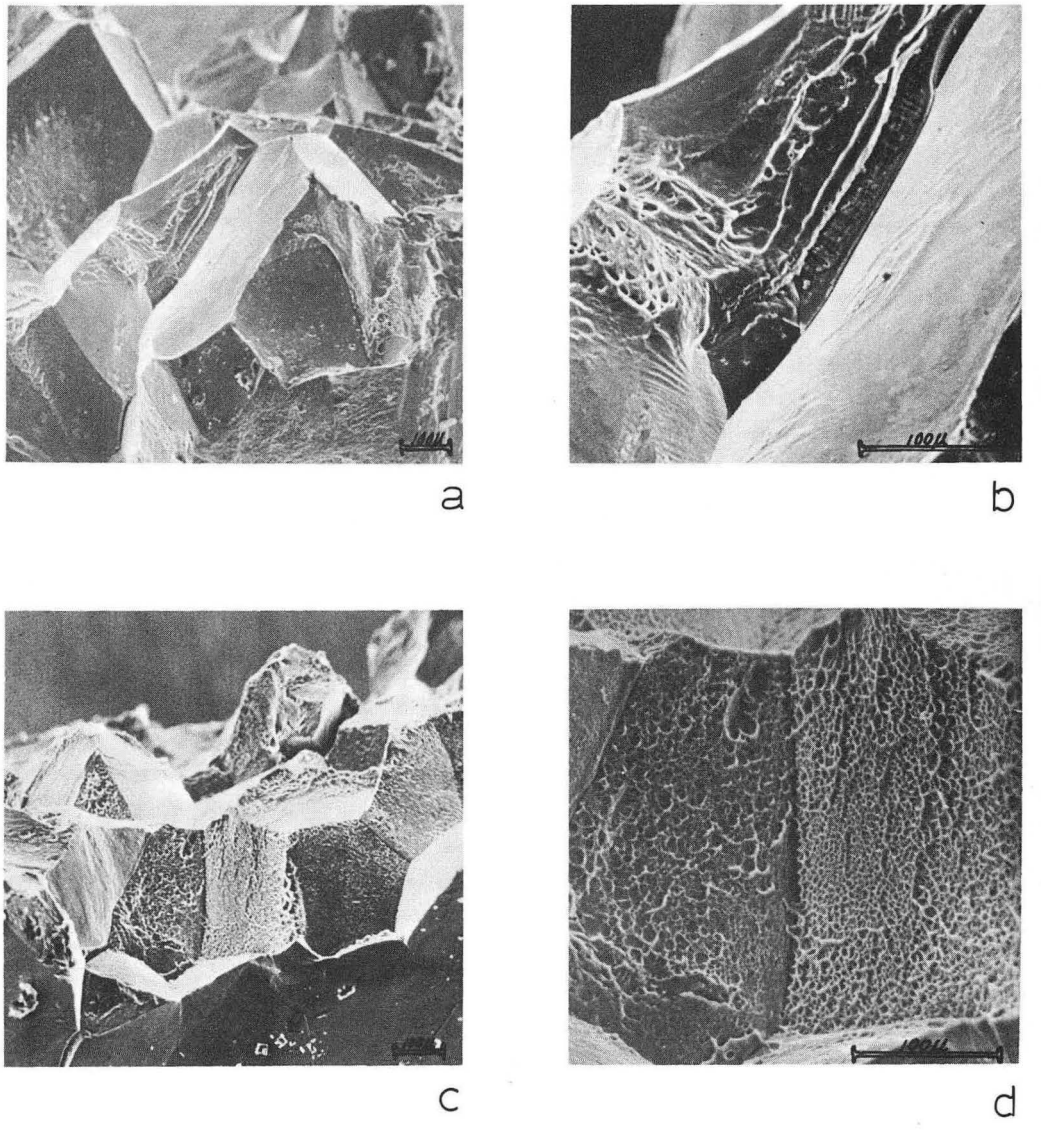

Fig. 44 Scanning electron fractographs of alloy 24, solution treated and aged:

(a) 30 min. at room temperature.
(b) same area as (a), higher magnification.
(c) 1000 min. at 125°C.
(d) same area as (c), higher magnification.

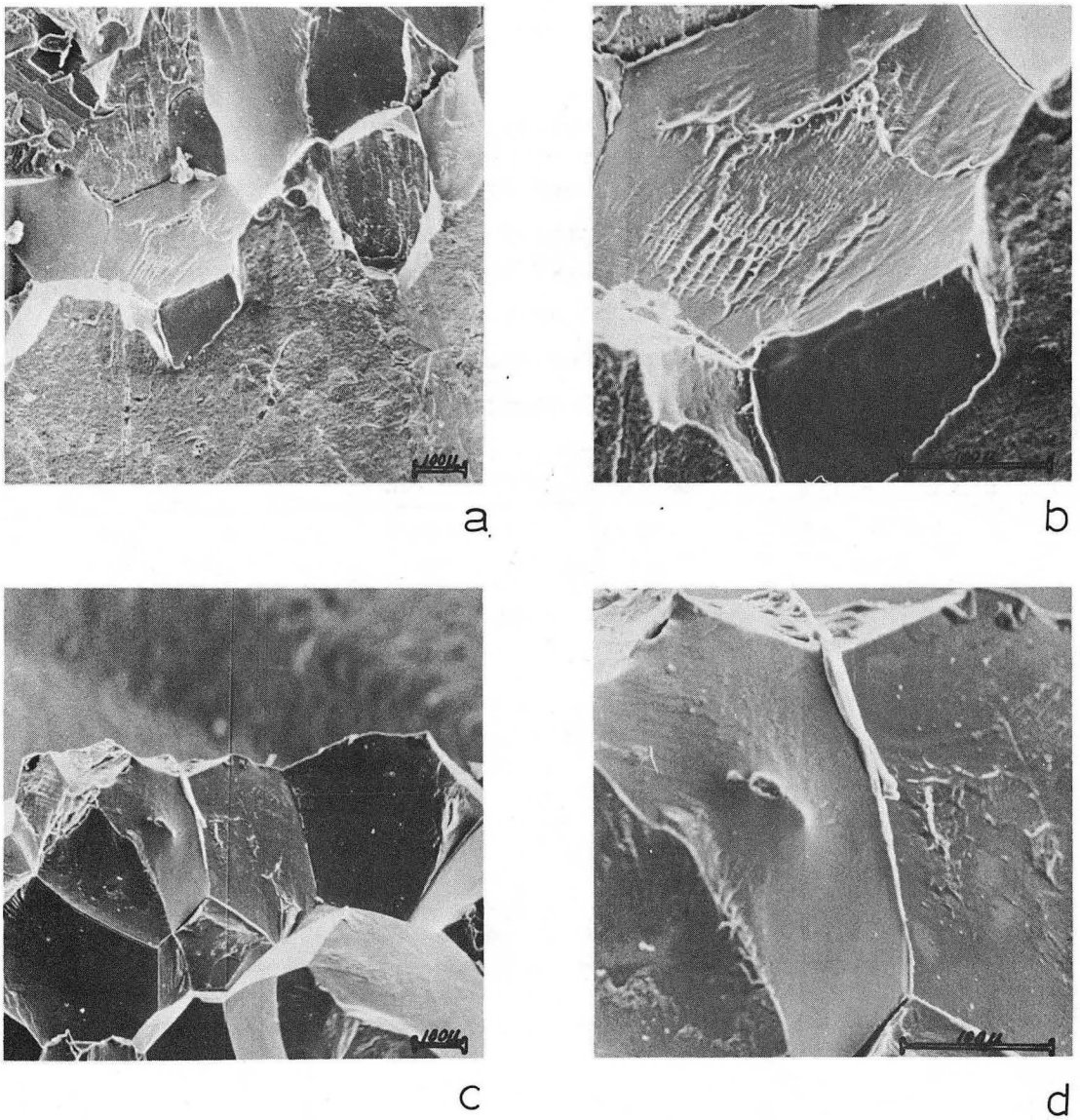

XBB 691-898

Fig. 45 Scanning electron fractographs of alloy 24, solution treated and aged for 30 min. at room temperature:

(b) same area as (a), higher magnification.
(d) same area as (c), higher magnification.

Fig. 46 Fractographs of alloy 24, solution treated and aged for 30 min. at room temperature. These fractographs show the fast-crack growth mode of fracture.

(a) scanning optical micrograph showing the area from which (b) to (d) come.

(b) an enlarged area of (a).

(c) scanning electron micrograph of the same area as (a).

(d) scanning electron micrograph of the same area as (c).

(e) to (g) a series of scanning electron micrographs of increasing magnification.

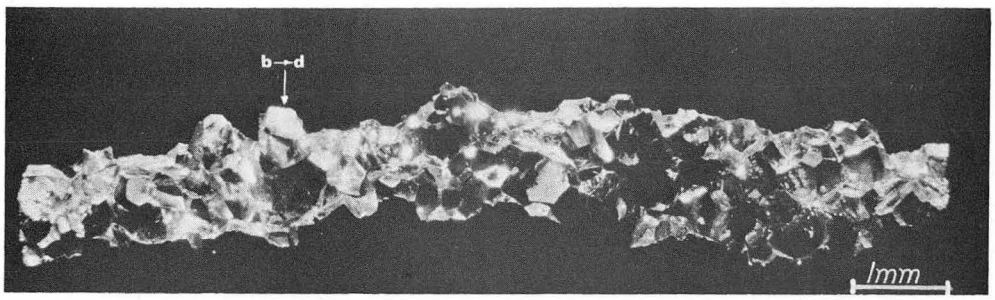

a

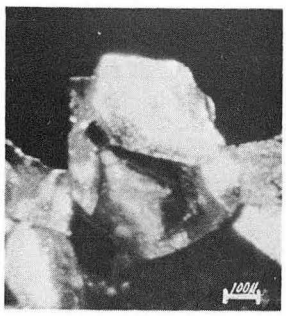

b

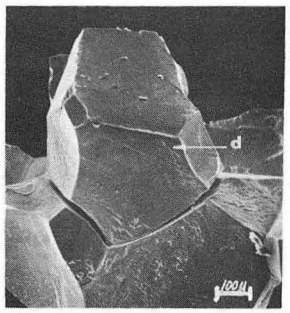

c

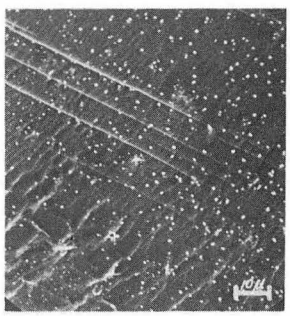

d

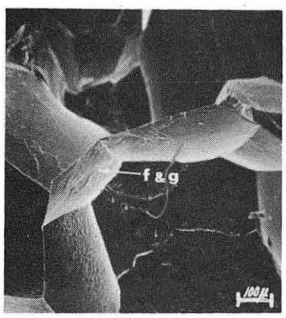

e

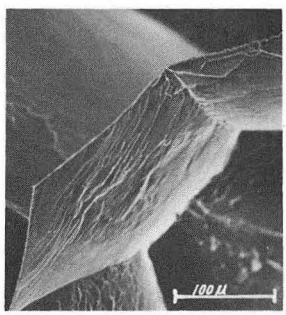

f

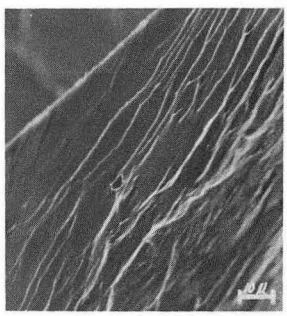

g

XBB 691-910

Fig. 46

Fig. 47 Fractographs of alloy 24, solution treated and aged for 6 sec. at 125°C. Slow-crack growth region.

(a) scanning optical fractograph showing the areas from which the scanning electron fractographs come.

(b) to (d) a series of scanning electron fractographs showing the fatigue to intergranular fracture transition.

(e) to (g) a series of scanning electron fractographs showing that fracture has occurred by microvoid coalescence.

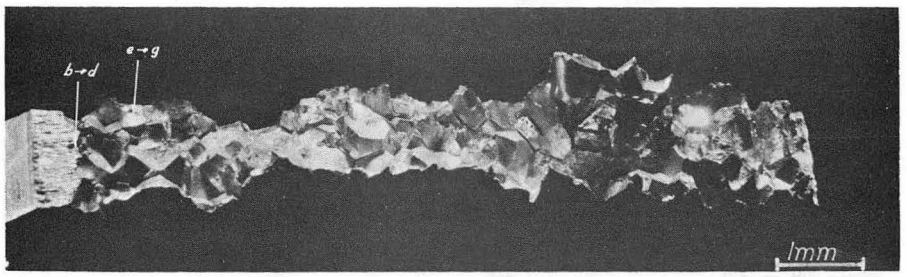

a

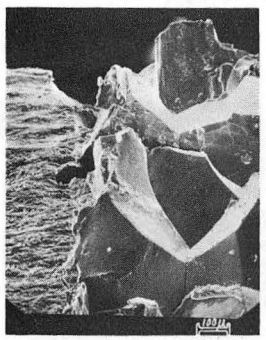

b

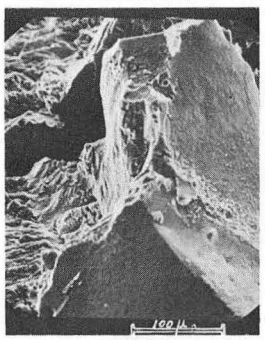

c

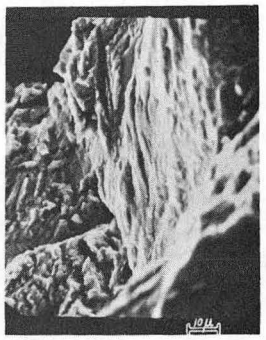

d

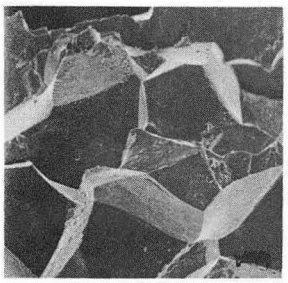

e

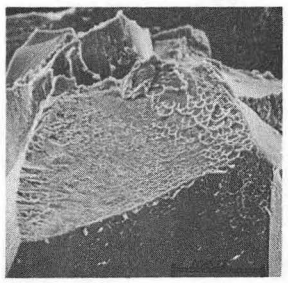

f

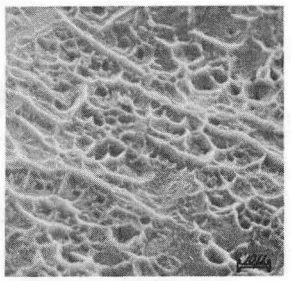

g

XBB 691-911

Fig. 47

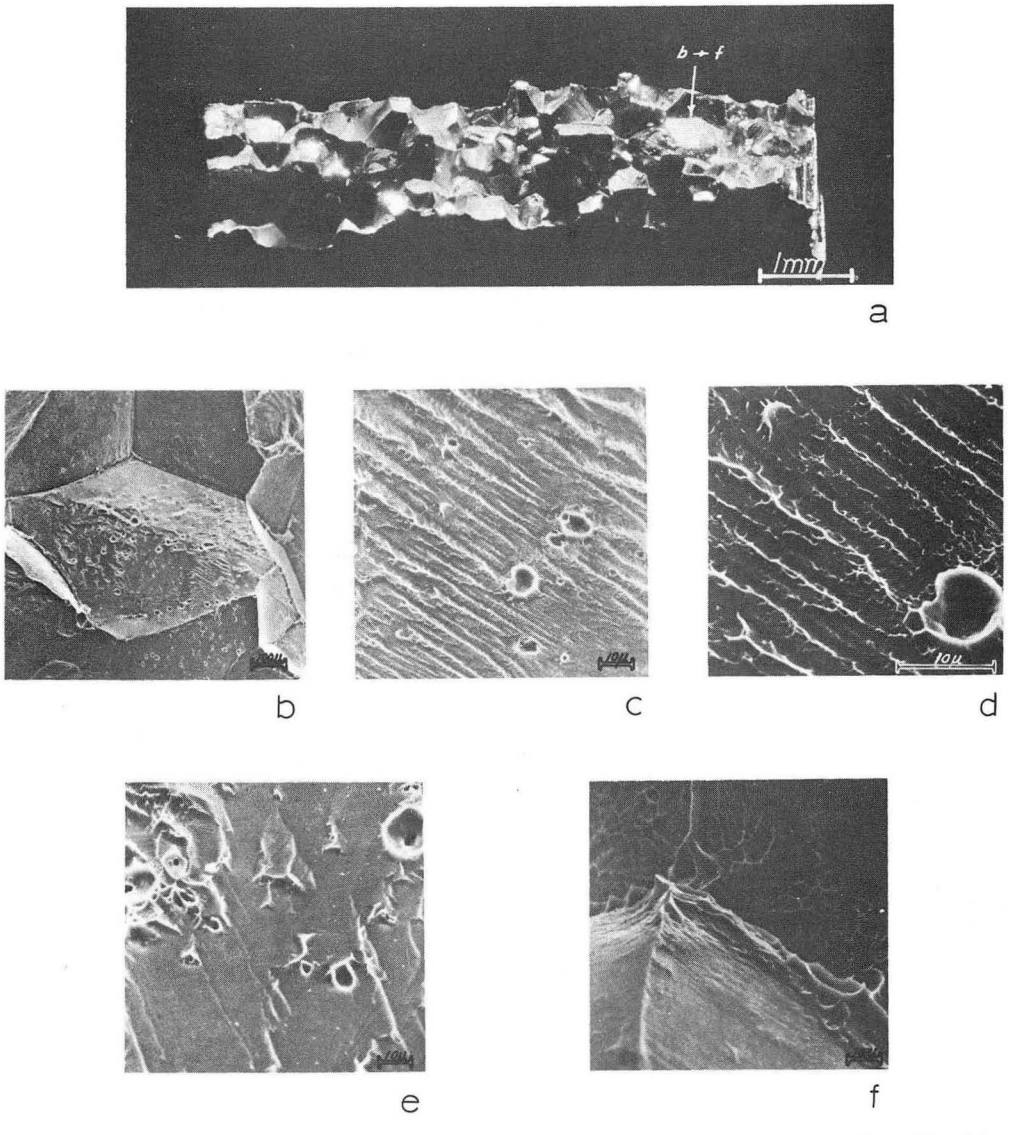

Fig. 48 Fractographs of alloy 24, solution treated and aged for 6 sec. at 125°C. Fast crack growth region.

(a) scanning optical fractograph showing the area from which the scanning electron fractographs come.

(b) to (f) a series of scanning electron micrographs showing the fast crack growth region.

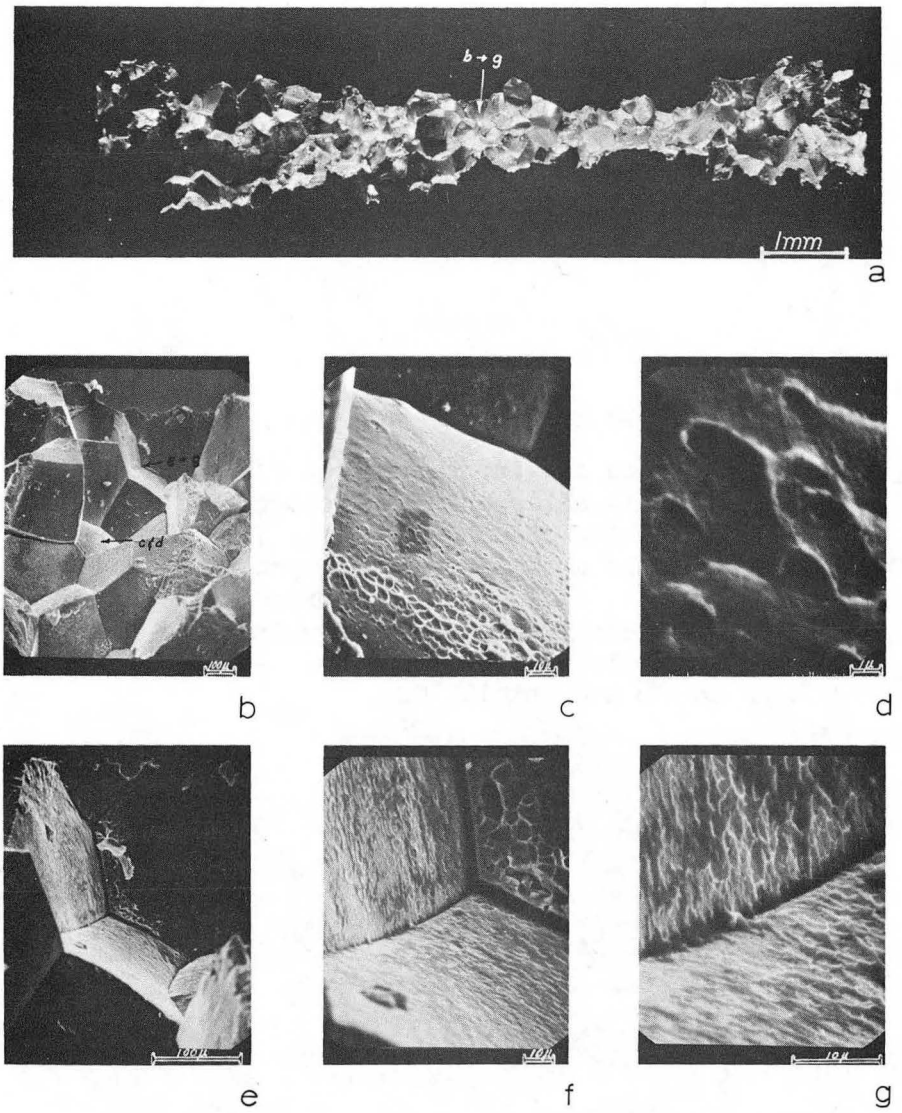

Fig. 49 Fractographs of alloy 24, solution treated and aged for 1 min. at 125°C.

(a) scanning optical fractograph showing the area from which the scanning electron fractographs come.

(b) to (g) a series of scanning electron fractographs showing how shear has taken place in the grain-boundary region.

Fig. 50 Fractographs showing the effect of abrasion of a grain facet. This abrasion may have occurred in situation similar to the one shown in Fig. 71. The fractograph (a) was taken on a standard metallograph and does not have the depth of field of the scanning electron fractograph (b). Both of these fractographs were taken of the same grain facet, in the same orientation. Alloy 24, solution treated and aged 6 sec. at 125°C.

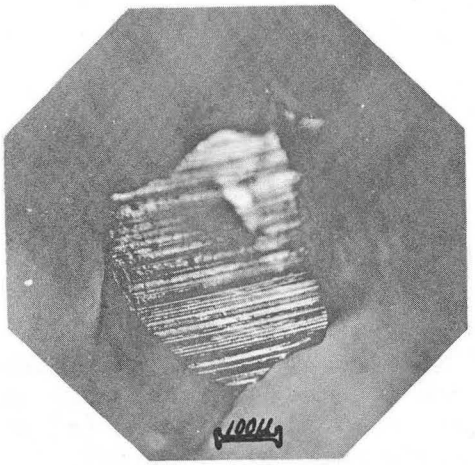

a

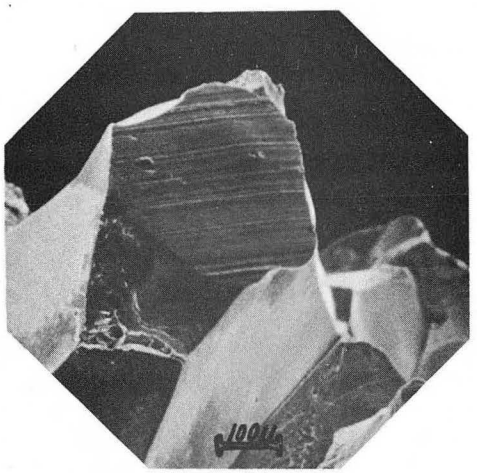

b

XBB 691-894

Fig. 50

Fig. 51 Fractographs of alloy 24, solution treated and aged for 6 sec. at 125°C, showing a change of fracture plane. The standard metallographic technique (a) does not have the resolution or the depth of field of the scanning electron fractograph (b). Both (a) and (b) are taken from the same grain facet. The series of fractographs (c) to (e) are taken from the grain facet shown in (b).

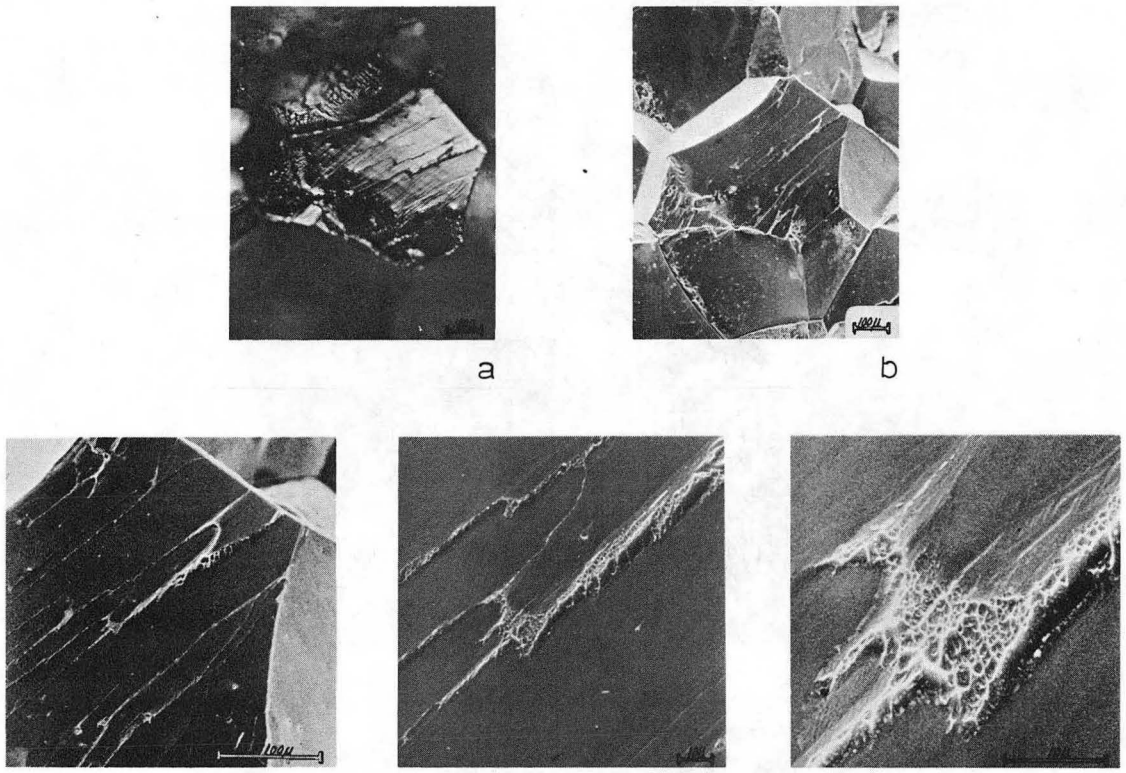

XBB 691-876

Fig. 51

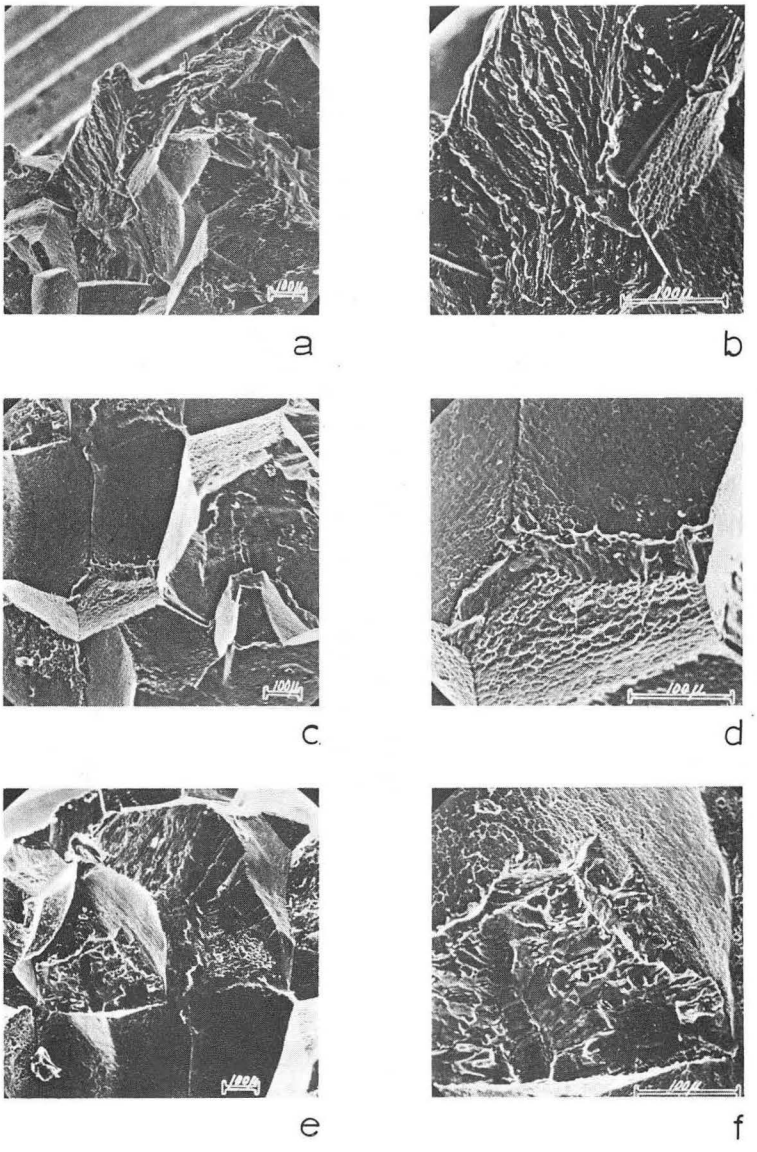

XBB 691-895

Fig. 52 Scanning electron fractographs of alloy 24, solution treated and aged for 1000 min. at 125°C, showing both transgranular and intergranular fracture. Arrow shows region of transgranular fracture (e).

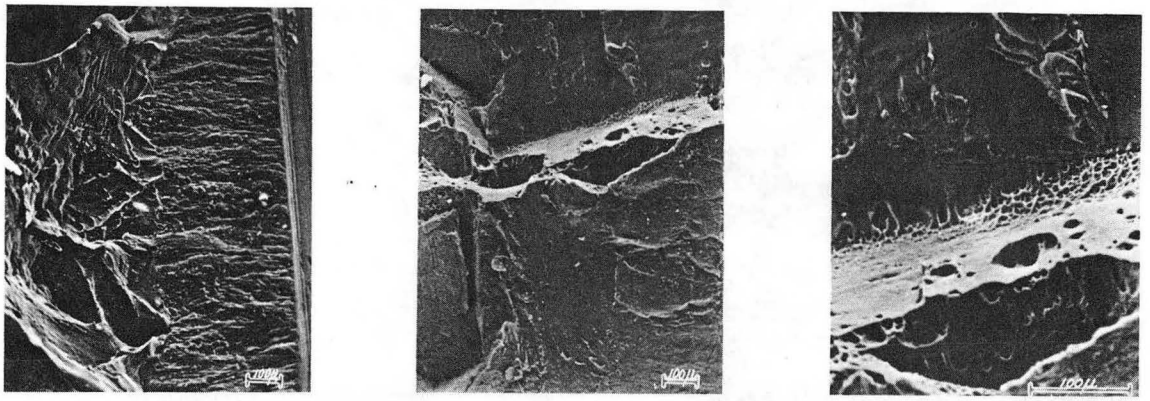

a b c

XBB 691-875

Fig. 53 Scanning electron fractographs of alloy 24, soltuion treated and aged for 10,000 min. at 125°C, showing the fatigue to transgranular fracture transition (a) and transgranular shear rupture (b) and (c).

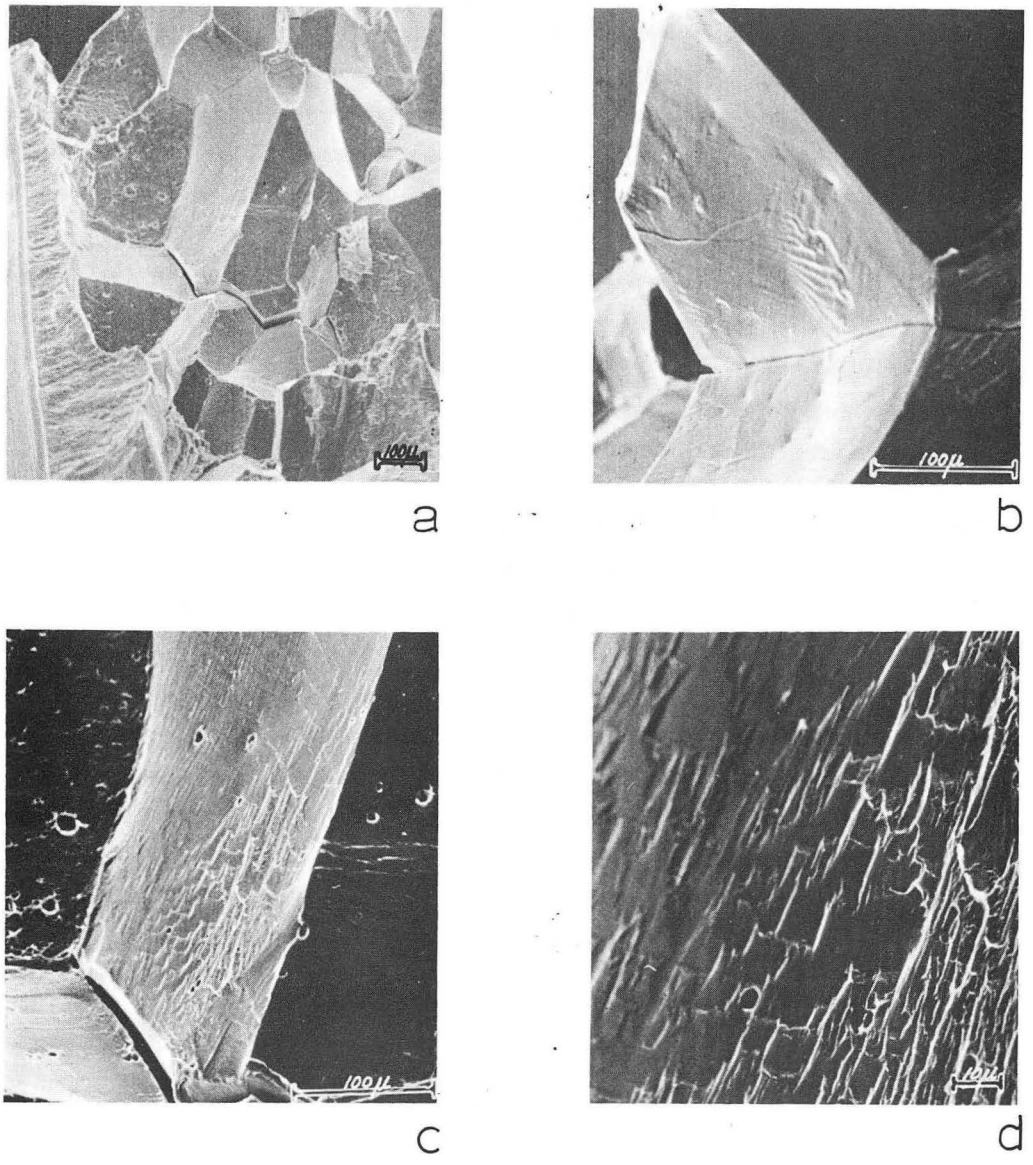

XBB 691-897

Fig. 54 Scanning electron fractographs of alloy 24, solution treated and aged for 30 min. at room temperature, tested at liquid nitrogen temperature. Fractographs show fatigue to intergranular fracture transition (a) and fast-crack growth fracture (b) to (d). Fractographs (b) to (d) are taken from the area shown in (a).

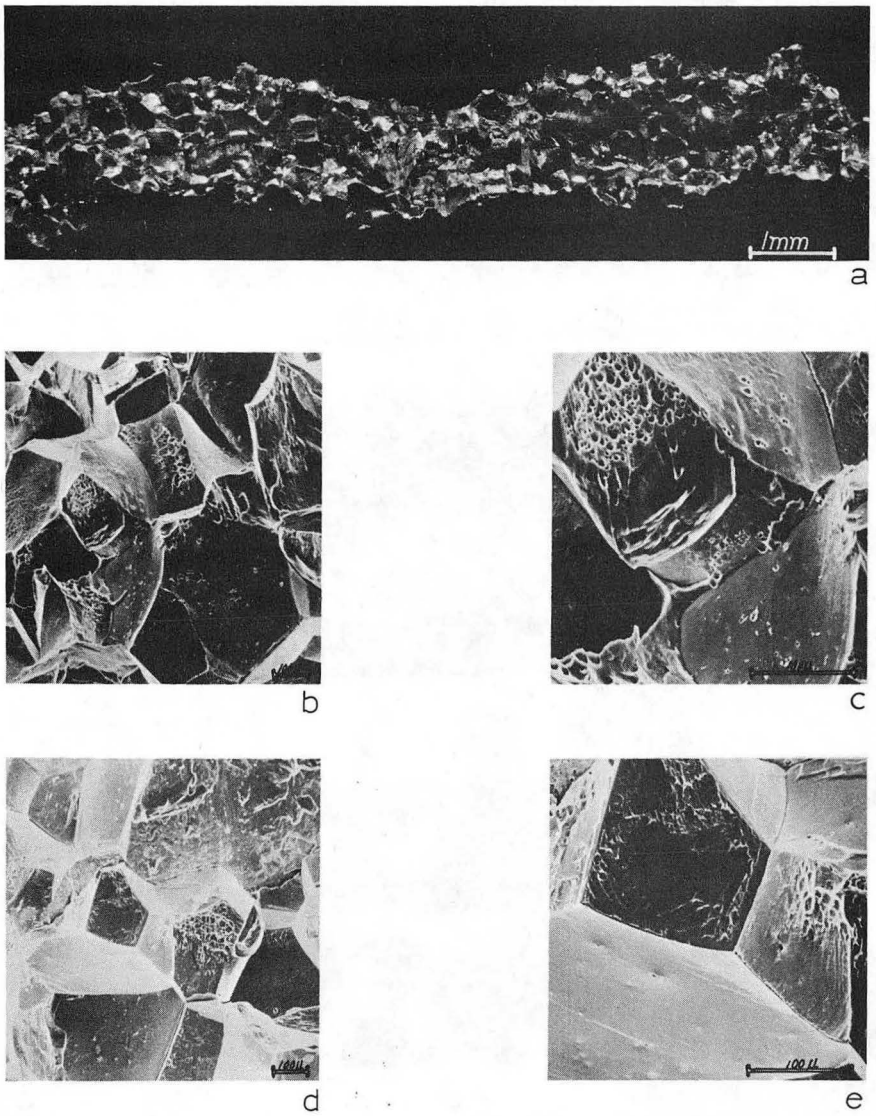

Fig. 55 Fractographs of alloy 24, solution treated and aged for 30 min. at room temperature (tested under impact conditions). These fractographs show that there is a mixture of fast-crack growth and transgranular shear modes of fracture.

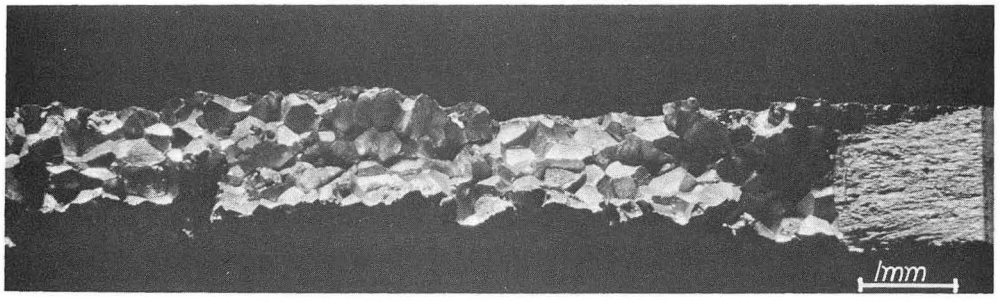

a

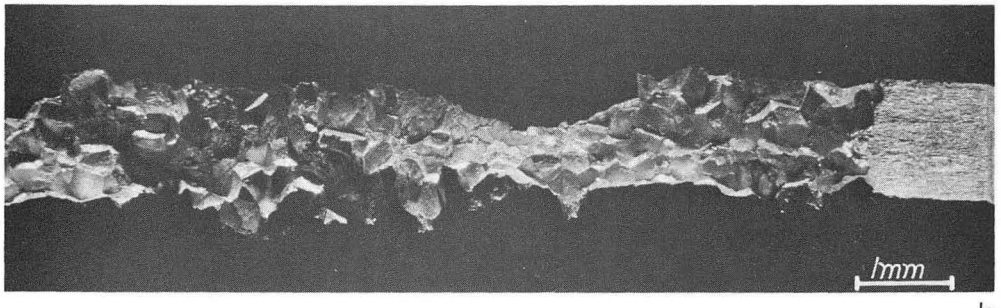

b

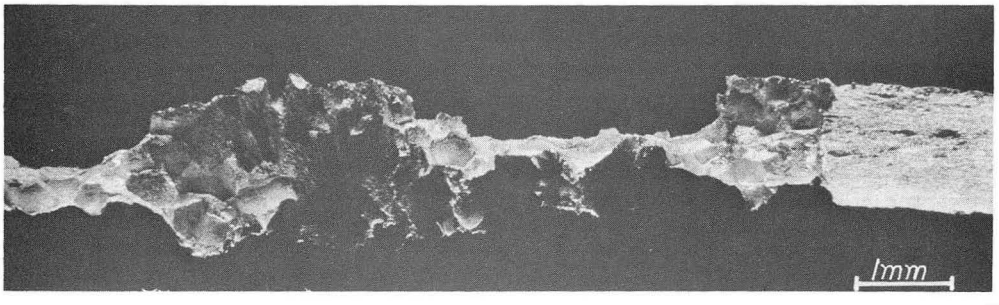

c

XBB 691-893

Fig. 56 Scanning optical fractographs of alloy 25, solution treated and aged:

(a) 30 min. at room temperature.
(b) 100 min. at 125°C.
(c) 1000 min. at 125°C.

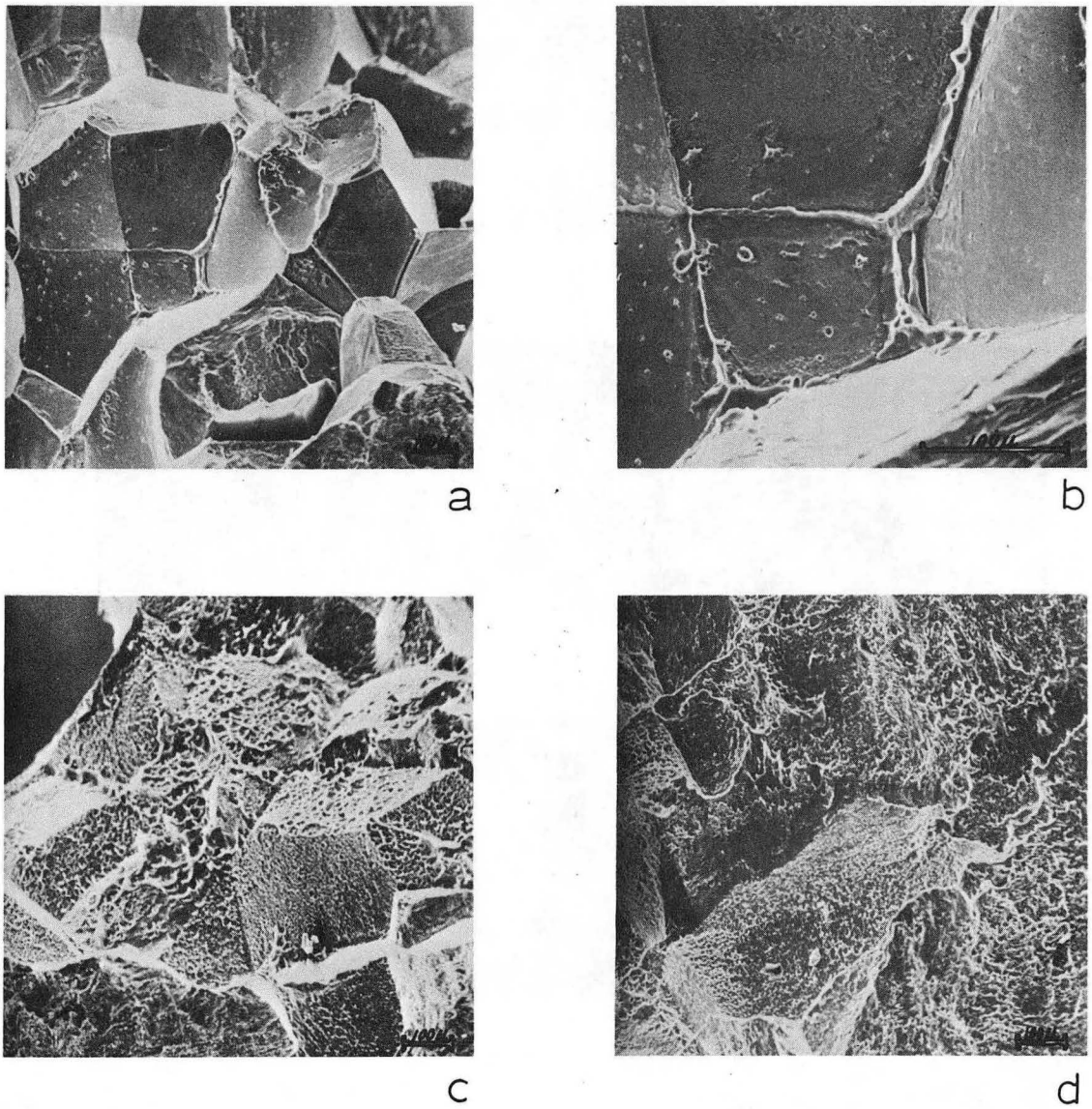

XBB 691-899

Fig. 57 Scanning electron fractographs of alloy 25, solution treated and aged:

(a), (b) 30 min. at room temperature. [(b) same area as (a)]
(c), (d) 1000 min. at 125°C.

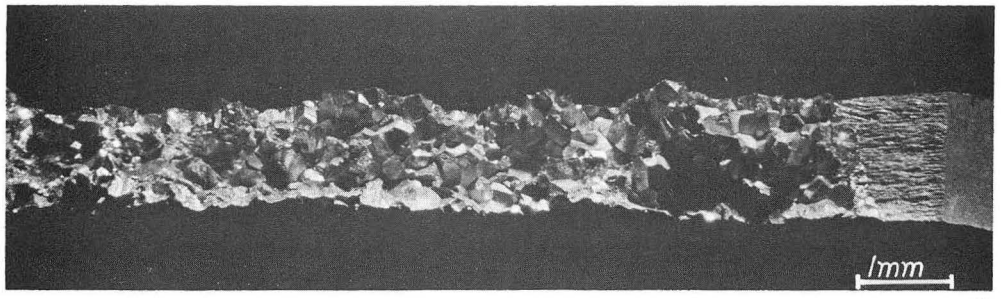

a

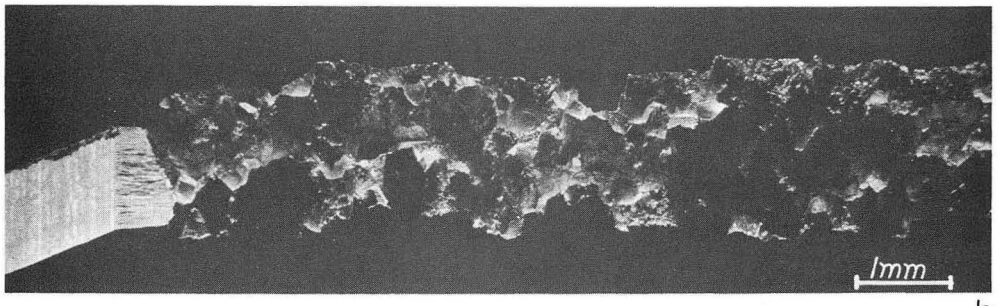

b

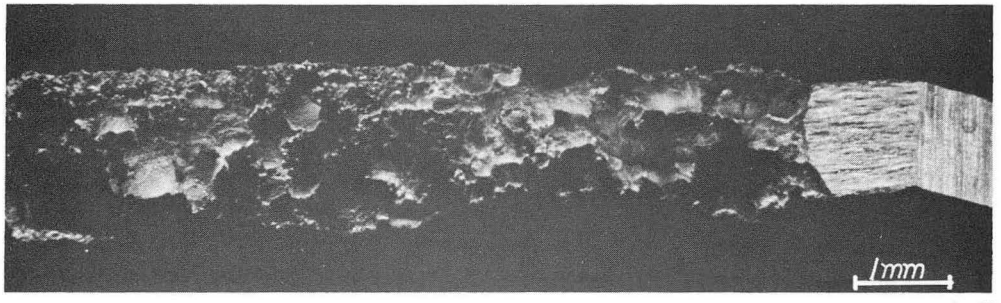

c

XBB 691-888

Fig. 58 Scanning optical fractographs of alloy 26, solution treated and aged:

(a) 30 min. at room temperature.
(b) 1000 min. at 125°C.
(c) 10,000 min. at 125°C.

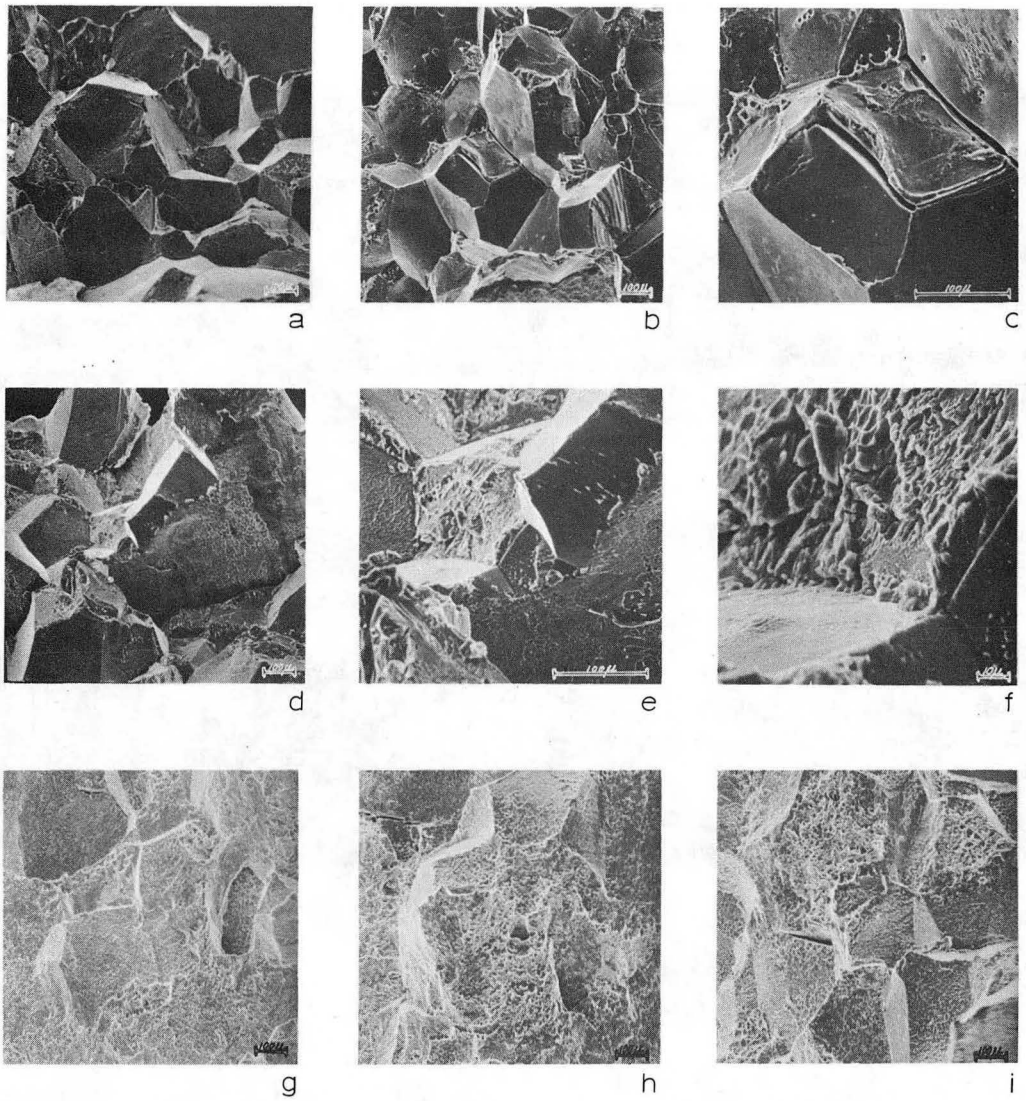

XBB 691-887

Fig. 59 Scanning electron fractographs of alloy 26, solution treated and aged:

(a) to (f) 30 min. at room temperature, (c) same areas as (b), (e) and (f) same area as (d).
(g) to (i) 1000 min. at 125°C.

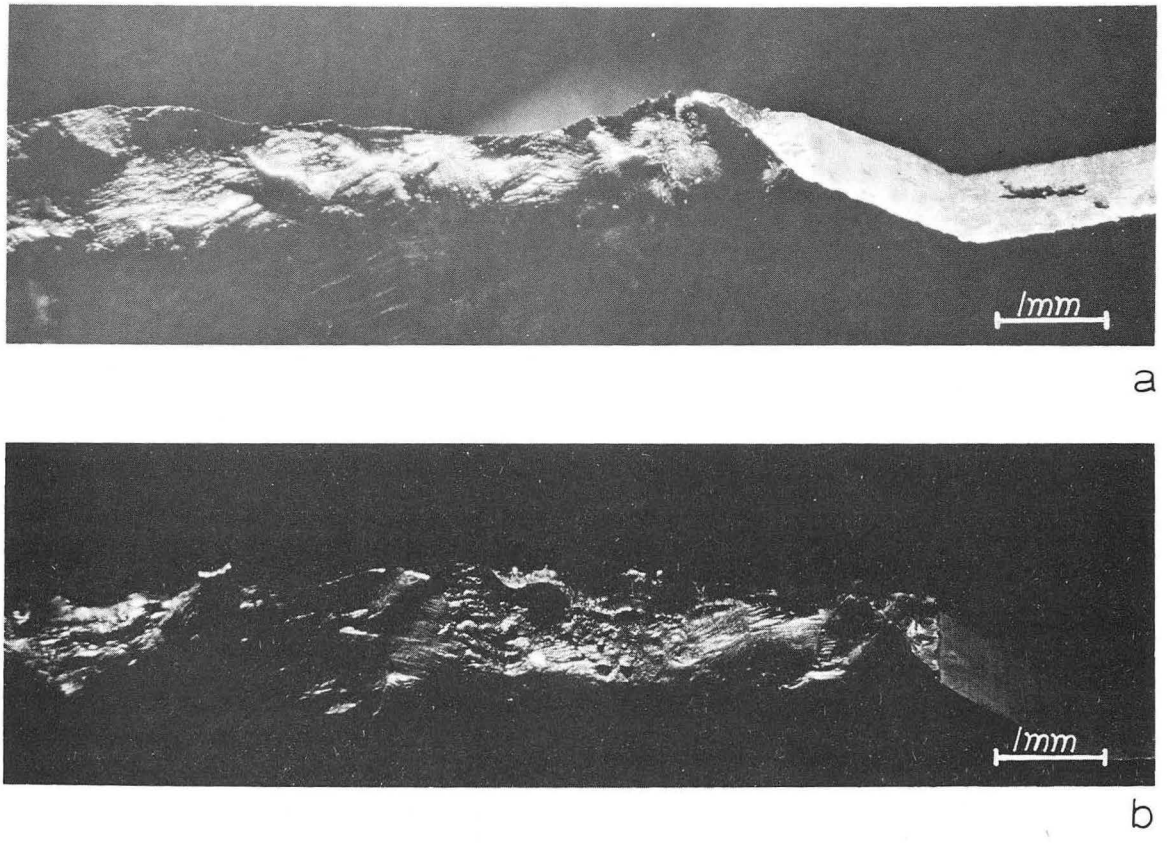

XBB 691-908

Fig. 60 Scanning optical fractographs of alloy 27, solution treated and aged:
(a) 30 min. at room temperature.
(b) 1000 min. at 225°C.

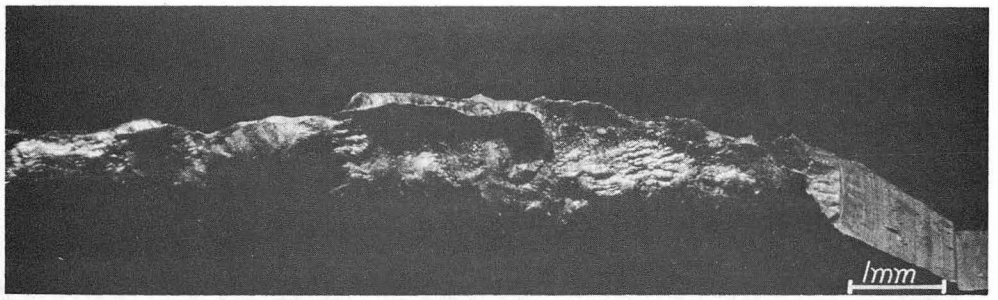

a.

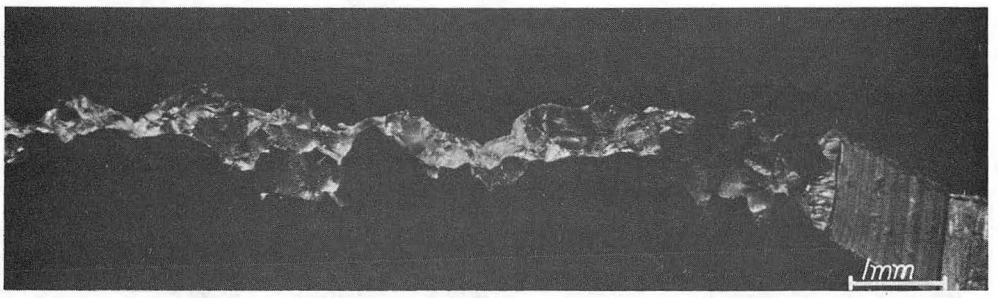

b

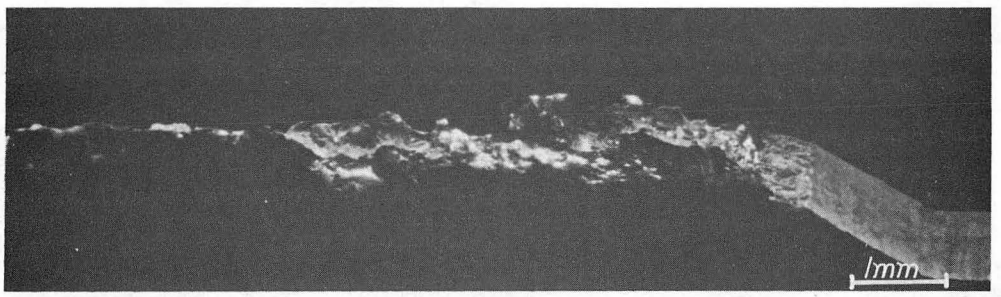

c

XBB 691-889

Fig. 61 Scanning optical fractographs of alloy 28, solution treated and aged:

(a) 30 min. at room temperature.
(b) 1000 min. at 225°C.
(c) 10,000 min. at 225°C.

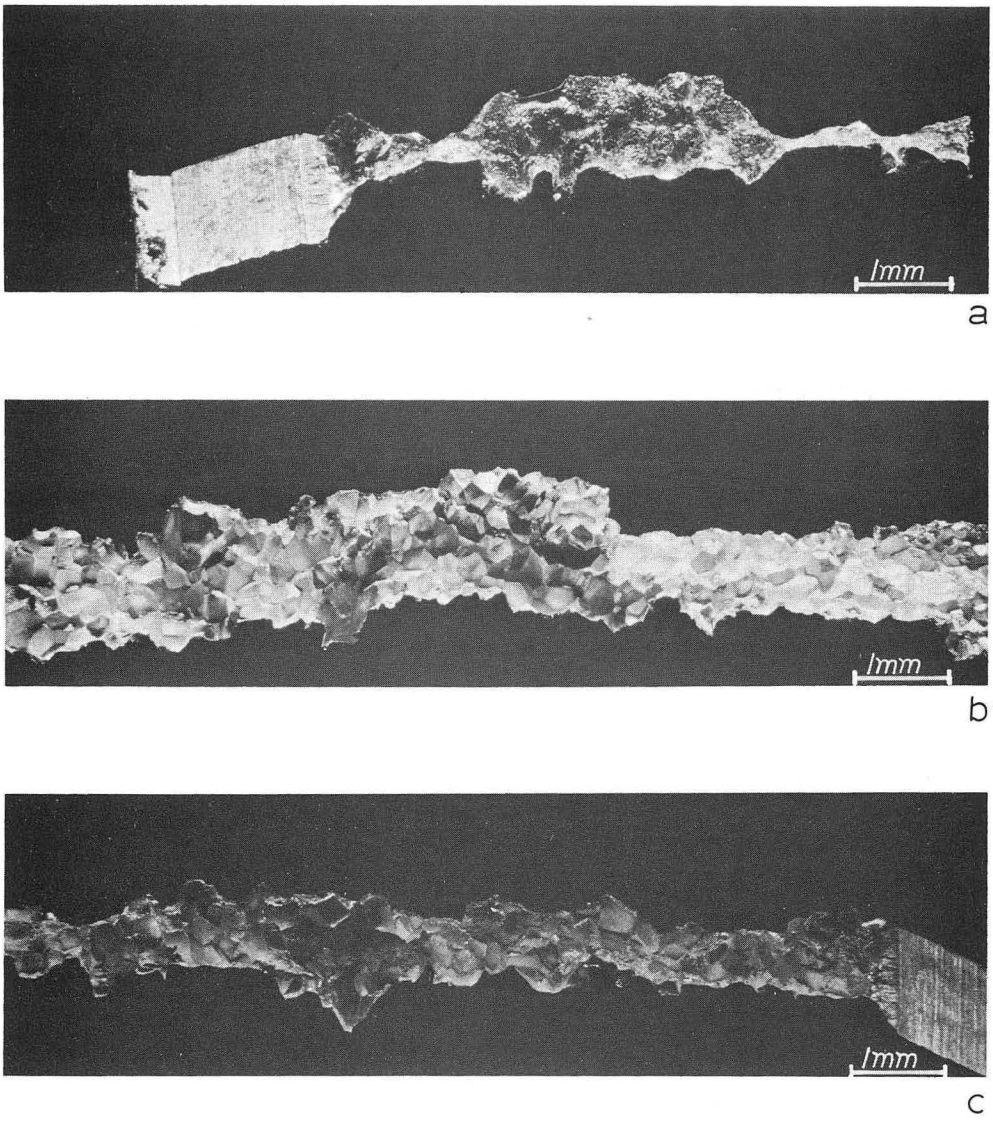

XBB 691-892

Fig. 62 Scanning optical fractographs of alloy 29, solution treated and aged:

(a) 30 min. at room temperature.
(b) 1000 min. at 225°C.
(c) 10,000 min. at 225°C.

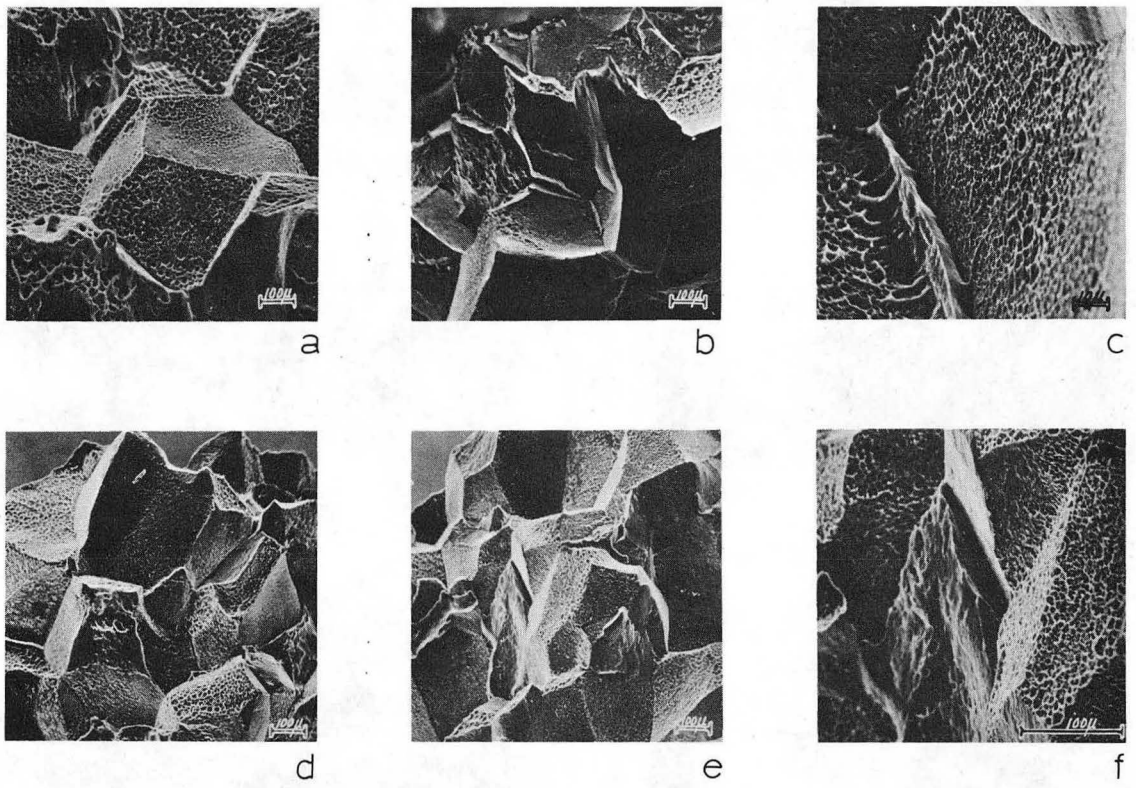

Fig. 63 Scanning electron fractographs of alloy 29, solution treated and aged:
(a) to (c) 100 min. at 225°C. (c) same area as (b).
(d) to (f) 1000 min. at 225°C. (f) same area as (e).

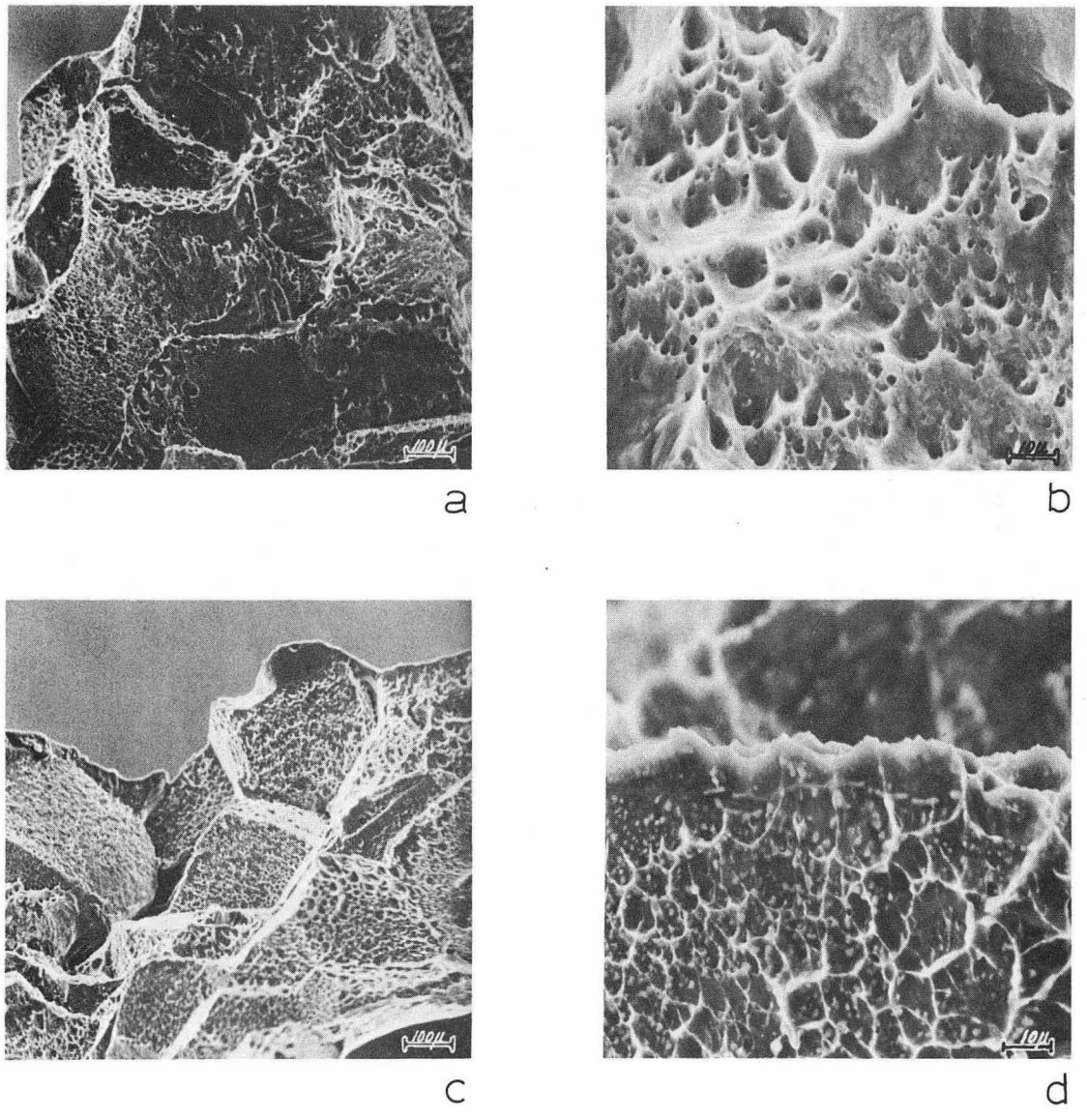

XBB 691-878

Fig. 64 Scanning electron fractographs of alloy 29, solution treated and aged 10,000 min. at 225°C, showing transgranular and intergranular modes of fracture. (b) same area as (a). (d) same area as (c).

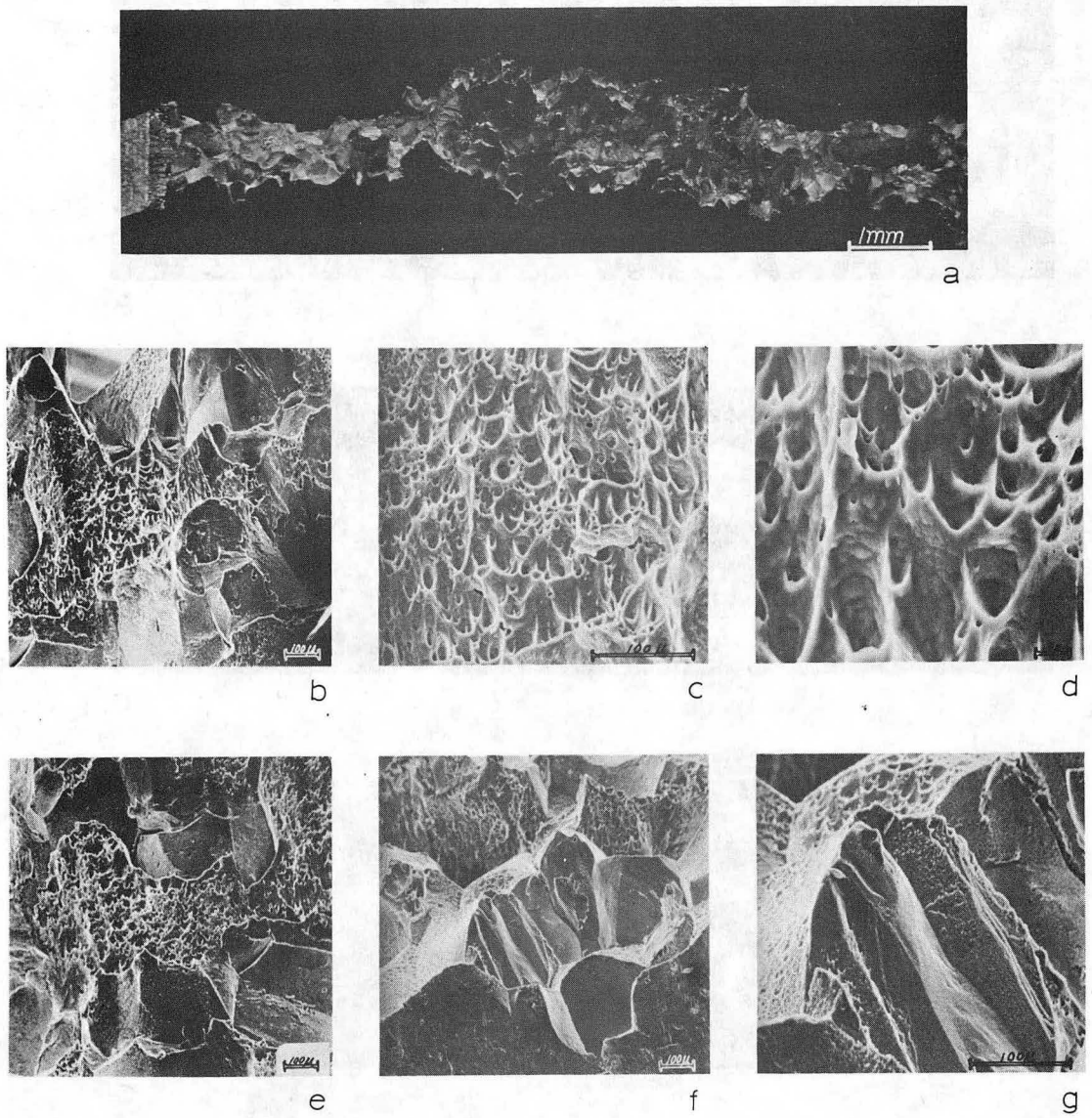

XBB 691-906

Fig. 65 Fractographs of alloy 29, solution treated and aged 100 min. at 225°C (tested under impact conditions). Both transgranular and intergranular fracture modes are found under impact conditions, though only the intergranular mode if found under standard testing conditions. (c) and (d) same areas as (b). (g) same areas as (f).

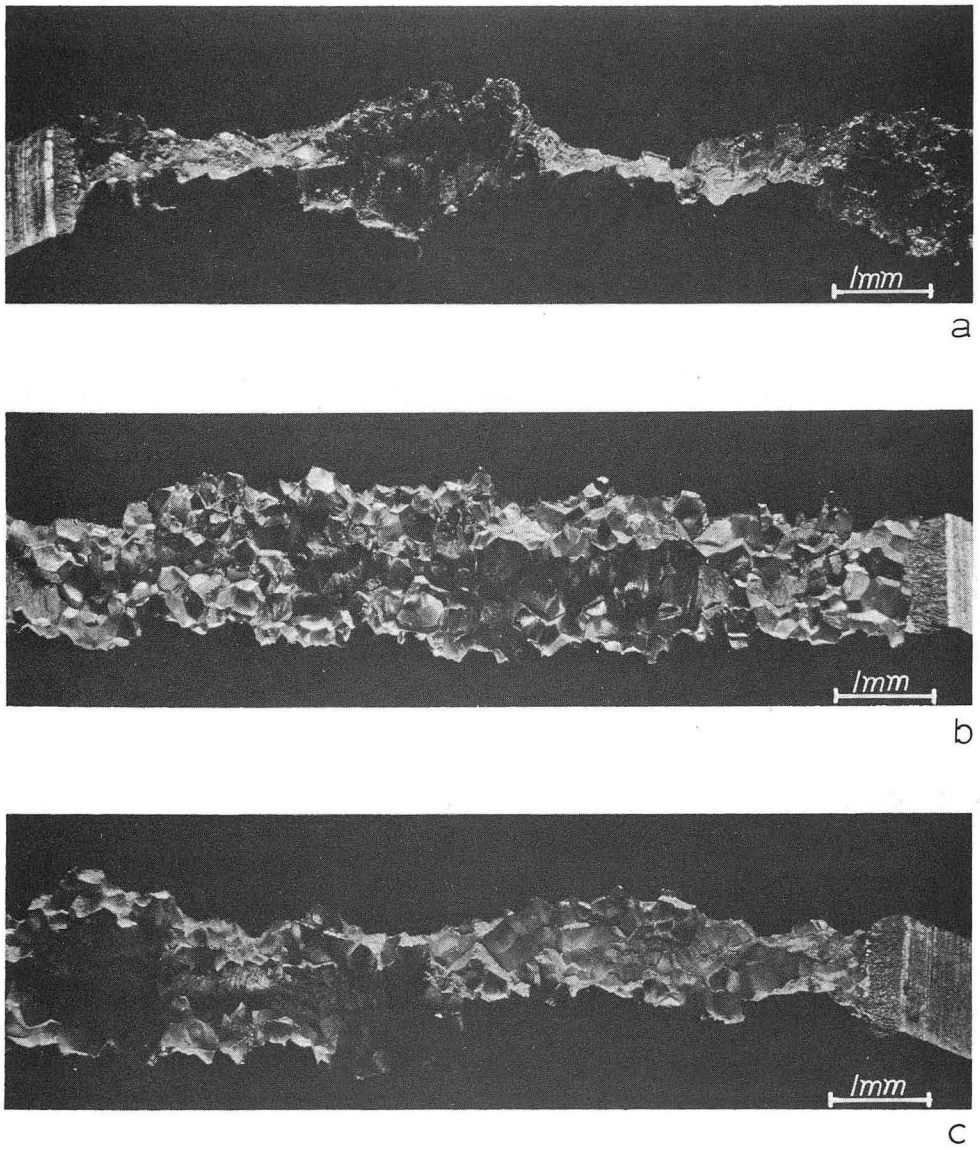

XBB 691-890

Fig. 66 Scanning optical fractographs of alloy 30, solution treated and aged:

(a) 10 min. at 225°C.
(b) 50 min. at 225°C.
(c) 10,000 min. at 225°C.

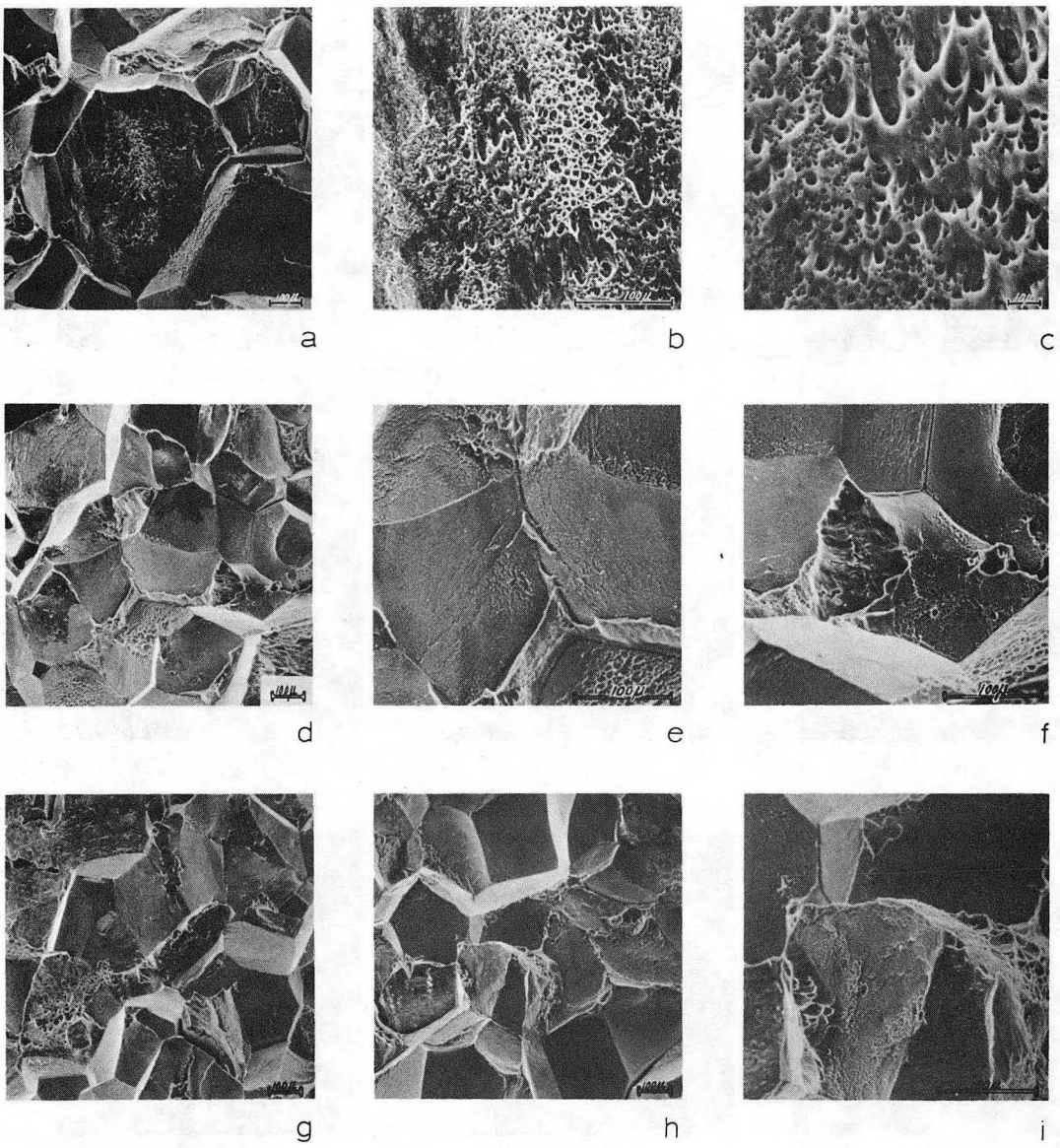

XBB 691-886

Fig. 67 Scanning electron fractographs of alloy 30, solution treated and aged 50 min. at 225°C. (b) and (c) same area as (a). (e) and (f) same areas as (d). (i) same areas as (h).

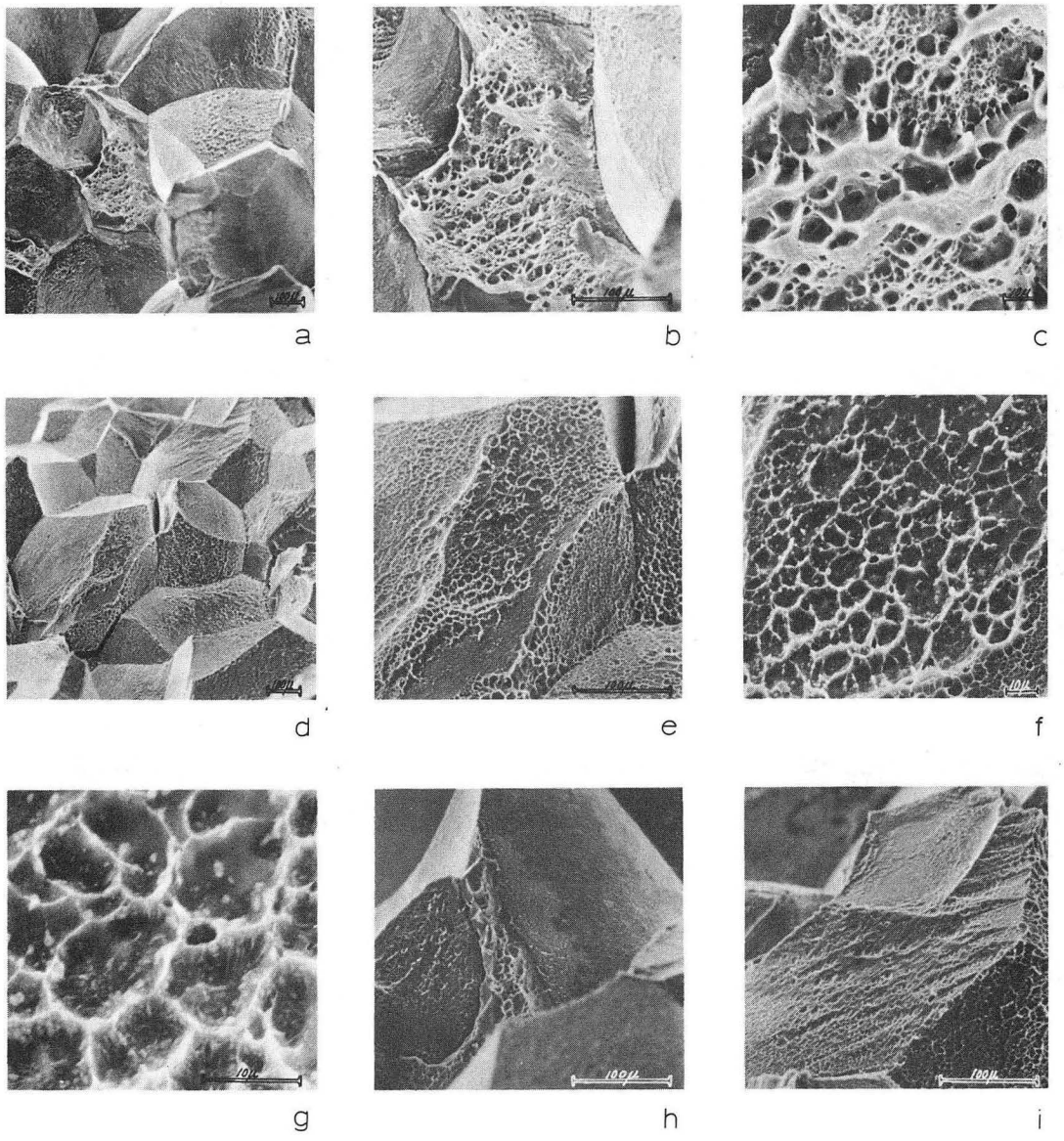

Fig. 68 Scanning electron fractographs of alloy 30, solution treated and aged 100 min. at 225°C. (a) to (c) and (d) to (g) are sequences of increasing magnification.

F. Miscellaneous Results

In analysing the results of the preceding tests it was found that additional observations were needed to help understand the fracture process. These observations, recorded in Figs. 69 to 78, are explained in the next section and the appendix.

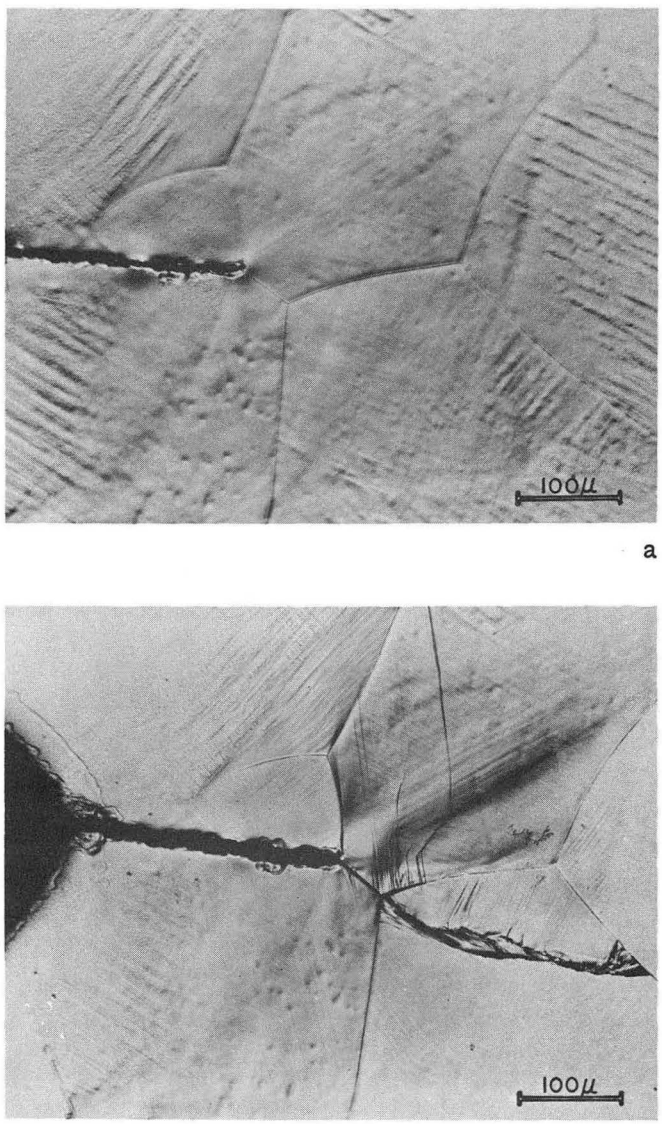

XBB 691-477

Fig. 69 Micrographs of alloy 24, solution treated and aged 30 min. at room temperature, showing crack growth during tension-tension fatigue. Micrograph (a) shows the position of the crack in a pre-cracked SEN fracture specimen before fatiguing. (b) shows the position of the crack after fatiguing for 100 cycles at a stress intensity of 12.5 ksi $\sqrt{\text{in.}}$ (approx.). The cyclic stress applied at 30 Hz.

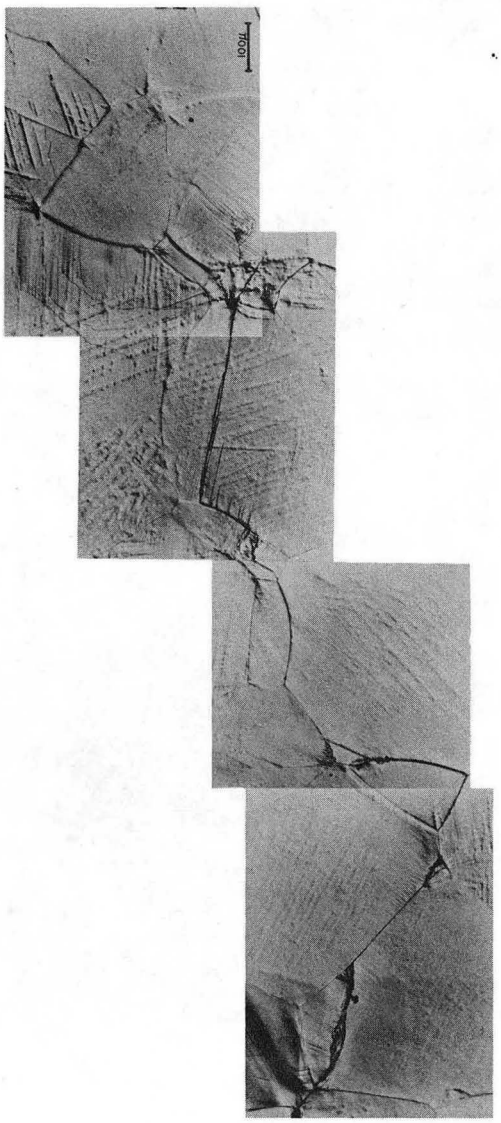

XBB 691-468

Fig. 70 Micrograph corresponding to Fig. 69 showing the position of the crack after 2600 cycles of fatigue (conditions same as given in Fig. 69).

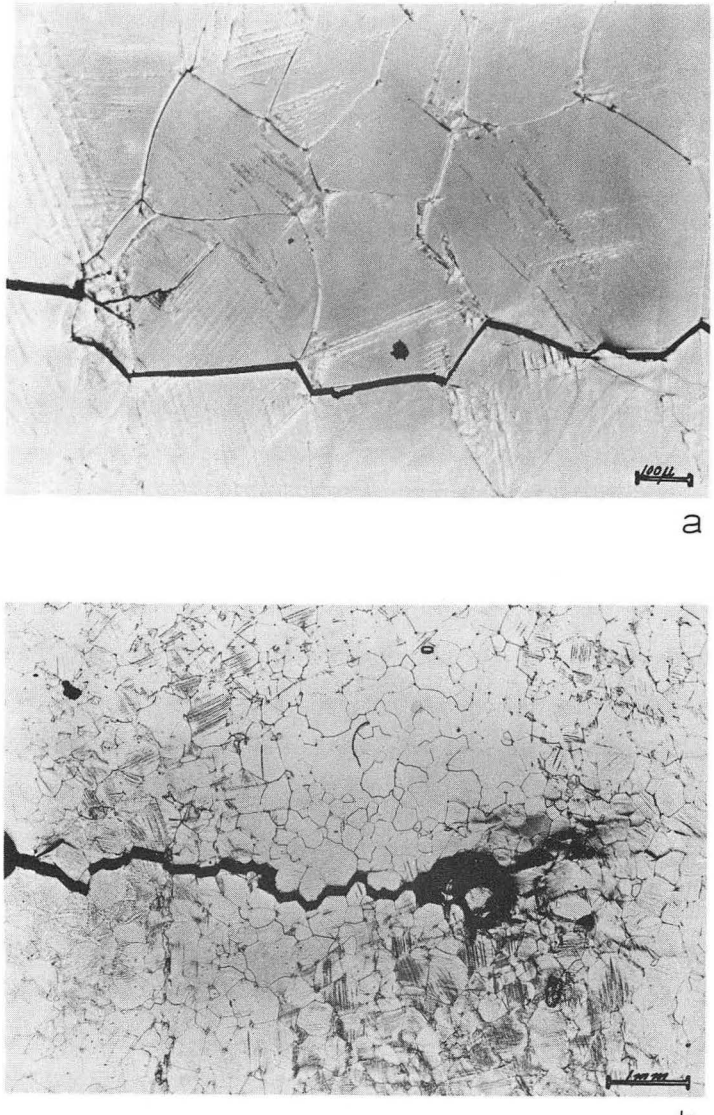

Fig. 71 Micrographs showing the growth of the crack in Fig. 70 under static loading conditions. (a) shows how the crack in Fig. 70 opened up when a small load was applied to the specimen while it was on the microscope state. (b) shows the growth of the above crack after the application of a load equivalent to a stress intensity of 33.8 ksi $\sqrt{\text{in.}}$ (approx.). The dark area at the end of the crack in (b) is a small plastic zone, shown in detail in Fig. 72.

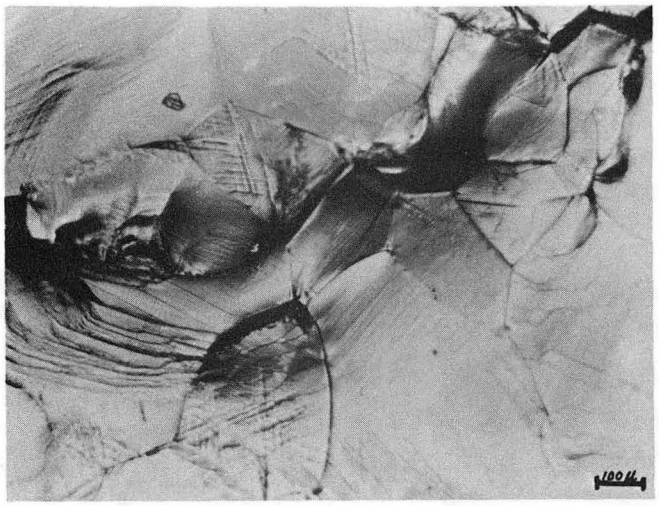

a

b

XBB 691-903

Fig. 72 Micrographs showing the plastic zone (a) and the end of the crack (b) corresponding to Fig. 71.

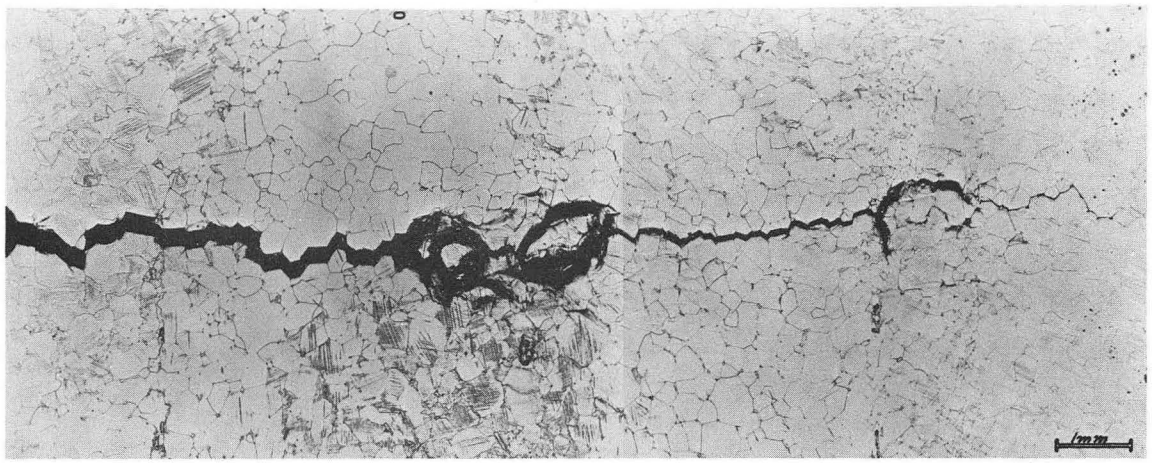

XBB 691-884

Fig. 73 Micrograph showing the growth of the crack in Fig. 71 on reapplication of the static load.

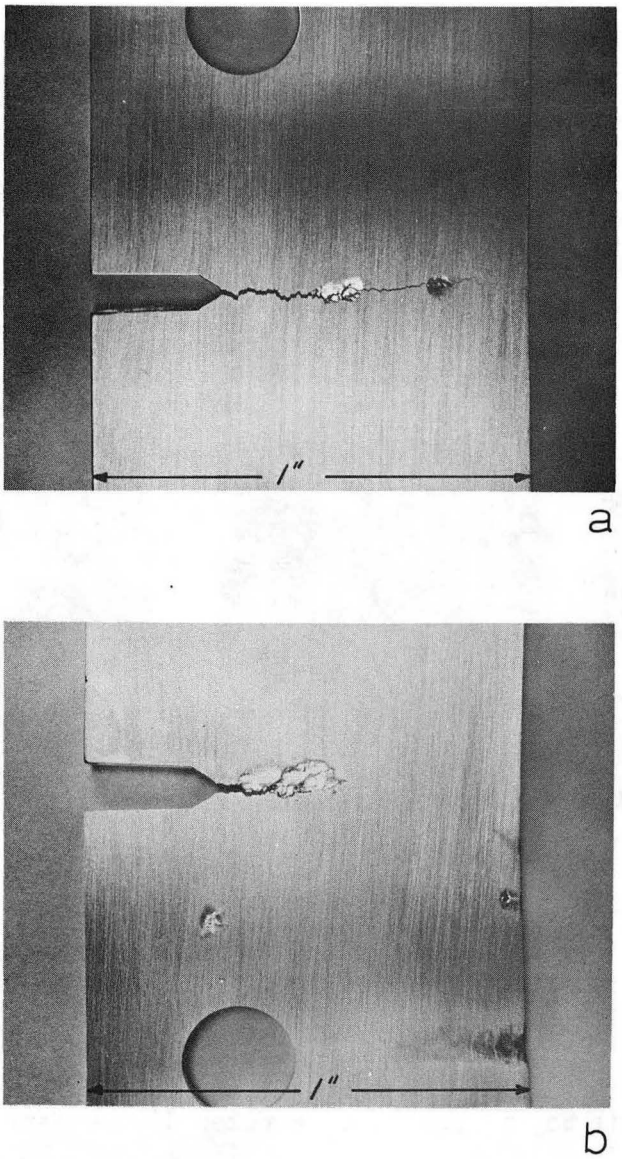

XBB 691-877

Fig. 74 Micrographs showing the plastic zones for two different heat treatments of alloy 24, (a) aged for 30 min. at room temperature and (b) aged for 1000 min. at 125°C.

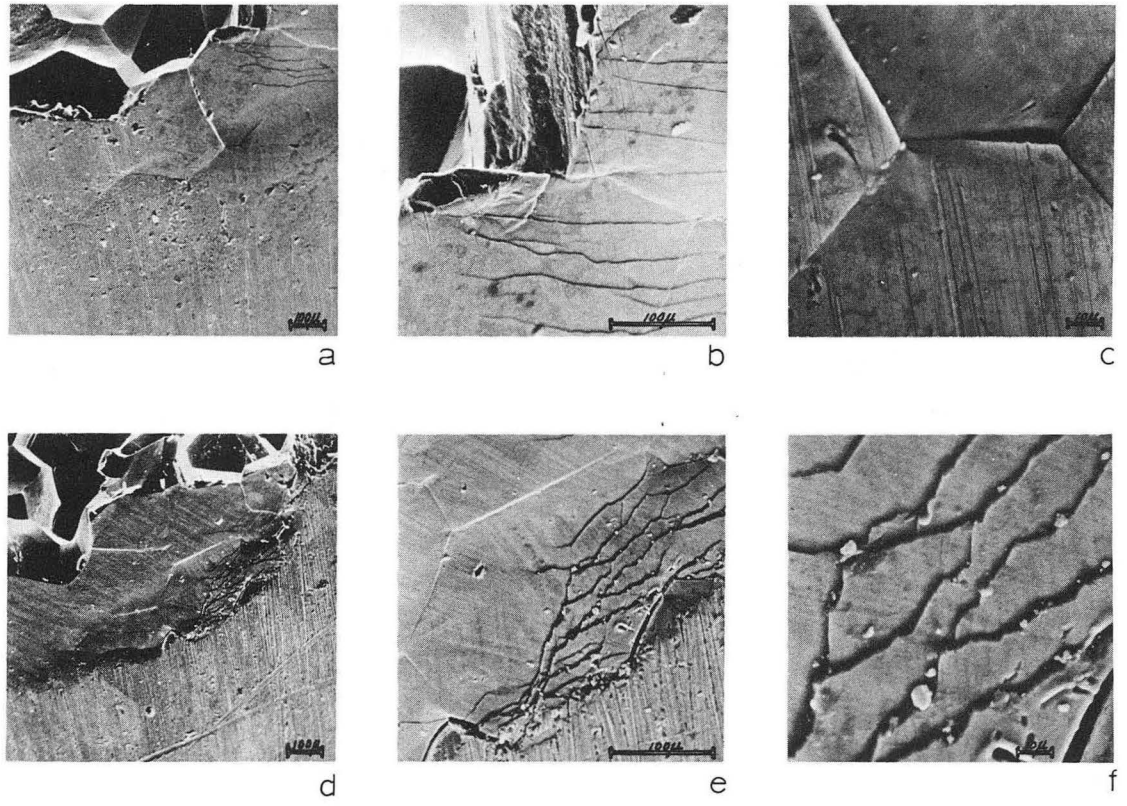

XBB 691-880

Fig. 75 Scanning electron micrographs of the first plastic zone in Fig. 74 (a). (a) to (c) and (d) to (f) form series taken in two separate areas of the plastic zone.

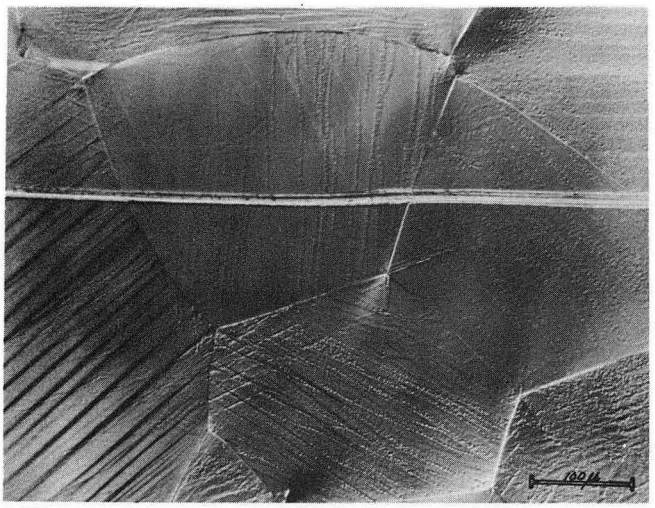

a

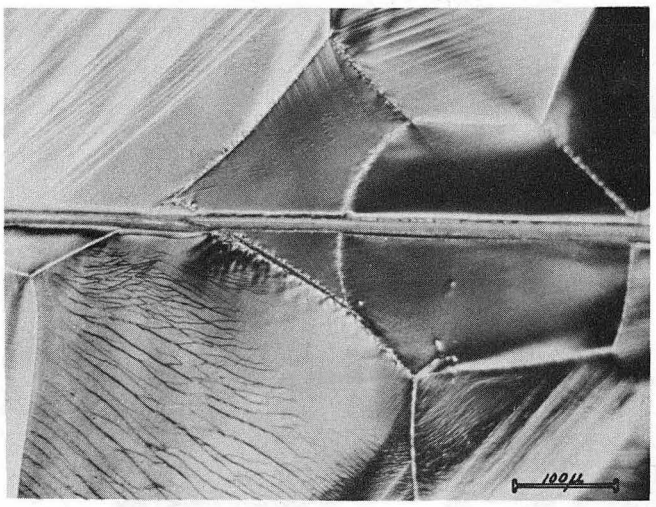

b

XBB 691-901

Fig. 76 Micrographs showing marker off-set and slip-line distribution for tensile samples of alloy 24. (a) solution treated and aged 30 min. at room temperature. (b) solution and aged 1000 min. at 125°C. Tensile specimens pulled to fracture.

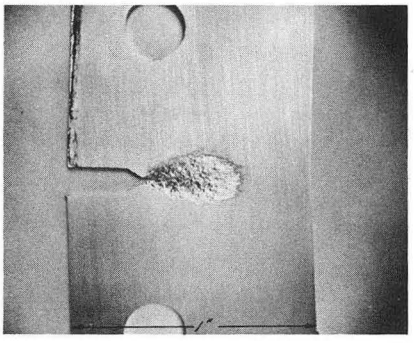

a

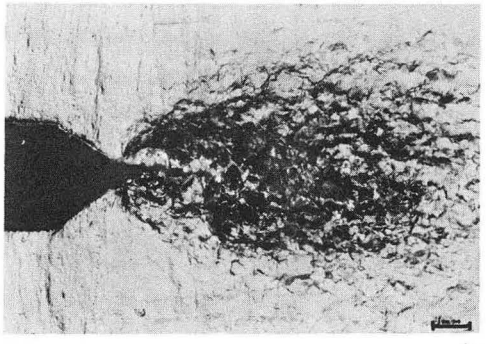

b

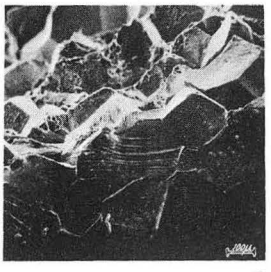

c

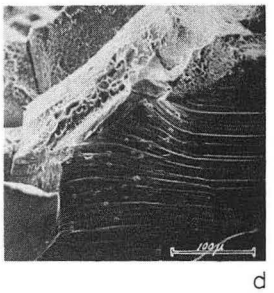

d

XBB 691-896

Fig. 77 Micrographs showing the plastic zone for alloy 29, solution treated and aged 100 min. at 225°C. The optical micrograph (b) and the scanning electron micrographs (c) and (d) are taken from plastic zone shown in (a).

a

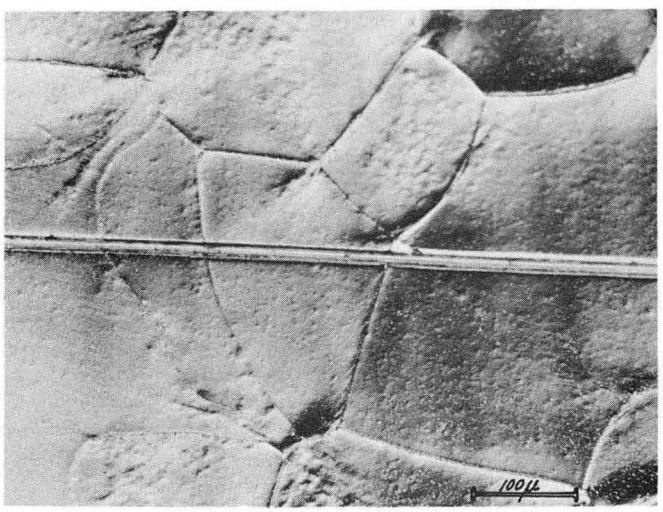

b

XBB 691-902

Fig. 78 Micrograph of a tensile sample of alloy 29, solution treated and aged 100 min. at 225°C, showing slip line distribution (a) and marker off-set (b). Tensile specimen pulled to fracture.

III. DISCUSSION

A. Tensile Properties and Microstructure

1. Aluminum-Zinc Alloys

The yield strength of the binary aluminum-zinc alloys was observed to decrease with increasing aging time (Figs. 4-6, 10, 13) and at first it appeared that this system did not precipitation harden. The work of Polmear[24] also suggested that this system has little or no age hardening potential. More recent work of Garwood and Davis,[25] however has shown that aluminum-zinc alloys (9 to 25% Zn) age harden fully in less than 2 min at room temperature, and retain this hardness for a long period of time. This indicates that the material has attained peak strength when it has been solution treated and aged for 30 min at room temperature. The further aging which followed at 125°C serves to overage the material and lower the yield strength the same as found by Seeman and Dodd.[26] In addition to the general overaging causing a decrease in strength there is a secondary hardening peak which appears at shorter aging times with increasing zinc content. This effect may be explained in terms of microstructure in manner similar to that suggested by Fink and Smith.[27] The alloy solution treated and aged at room temperature for 30 min corresponds to a microstructural condition where zones have been homogeneously formed in the bulk (possibly by a spinodal transformation)[28-30] and with zinc precipitated preferentially in the grain-boundary region.* It is also possible that α' (fcc transition structure) was preferentially precipitated in the grain-boundaries, but this structure was not identified.

---

*In this and future discussions the "grain-boundary region" includes the precipitate-free zones and the material between the precipitate-free zones.

Preferential precipitation may be seen in the plane of the grain-boundary in Fig. 32(b). Note the narrowness of the grain-boundary and the precipitate-free zone. The amount of precipitation in grain-boundaries can be seen to increase with alloy content (Figs. 28 to 30,33 and 34). Alloy 26 in the solution treated condition shows gross precipitation in the grain-boundaries (Fig. 34), which may have occurred during the quench as well as during aging at room temperature and as observed by Thomas.[31] Material in this condition fails intergranularly. Aging causes the zones to transform to either the R (rhombohedrally distorted fcc) transition phase, then to the α' transition phase, or directly to α'.[29] The heterogeneous zinc precipitate in the grain-boundaries has coalesced with aging and the grain-boundary regions have widened, as shown in Figs. 31(a) and 32(c to f). At the same time there is the cellular growth of zinc out of the grain-boundaries into the interior of the grains. Most of the deformation still takes place in the grain-boundary region, but it more easily accomodated because the weak zone is wider. This is illustrated in Fig. 76, where the marker offset along the grain-boundary (0.1μ for (a), 1μ for (b)) can be used to calculate the contribution of shear in the zone shearing grain-boundary region to the overall strain. Using a standard equation for grain-boundary shearing[32] one can account for most of the observed elongation in both cases. The initial decrease in yield strength with increased aging time is soon overcome by a secondary hardening effect due to appearance, in the bulk, of the transition phase. Further aging causes a general decrease in yield strength due to the cellular precipitation of zinc and the overaging of the transition phase.

2. Aluminum-Silver Alloys

The change of tensile properties with aging time shown in Figs. 18

to 21 can be explained in terms of the aging sequence and microstructure present. The accepted aging sequence of this alloy system begins with the homogeneous formation of spherical zones (possibly by a spinodal mechanism). This is followed by the heterogeneous precipitation of γ' (the fcc transition structure) and finally the cellular precipitation of γ (hcp, Ag_2Al) emanating from the grain-boundaries (Figs. 37-39). The initial rise in yield strength with aging time is probably due to the precipitation of γ in the grain boundaries and growth of zones in the bulk. Increasing the aging time brings about overaging at the grain-boundaries, a decreasing density of zones, and a slight drop in the yield strength. This is followed by general hardening due to the formation of the γ' in the bulk (Fig. 39) which leads to peak strength. Final softening comes from cellular precipitation of γ. The fracture is transgranular in the early stages of aging, gradually becoming completely intergranular as the aging approaches peak strength. Overaging causes the fracture to become increasingly transgranular (Figs. 60 to 62, and 66). At peak strength the grain boundary region, and hence the zone for plastic flow, is much wider than for a similar case in the Al-Zn system. (This qualitative explanation assumes that the grain-boundary regions have a lower yield strength than the grains.) Al-Ag alloys still fail intergranularly in the peak strength condition but there is a more homogeneous distribution of strain, as evidenced by Fig. 78. Here the slip lines are of higher density and more uniformly distributed than in Fig. 76 and there is no appreciable marker off-set along the grain boundaries. Thus, the boundary region shear does not account for the majority of the elongation in this case.

B. Crack Growth Processes

1. Al-Zn Alloys

a. Transition in Fracture Process

Macroscopic fracture surface studies of the small SEN fracture specimen revealed that under certain conditions there was a change in surface luster as a crack advanced. A dull surface formed next to the fatigue crack and extended along the fracture path until the transition point was reached, where the surface appearance became bright. Observations of dull and bright fracture surfaces have been made by other investigators[2,4,33] but little has been said about the causes for the different appearances. The routine fracture tests showed that the transition occurred only in alloys 24, 25 and 26 of the Al-Zn series. The fracture transition was found in the peak strength condition where the specimens had been aged at room temperature for 30 min, or aged at 125°C for 6 sec, plus 30 min at room temperature. In alloy 26 the transition was only found in one specimen aged at room temperature, it was not found in the duplicate specimen or in the specimens aged at 125°C for 6 sec. All conditions where a transition was not observed, the fracture surface had a dull appearance.

Large SEN fracture specimen (Fig. 1a) were instrumented with a clibrated COD gage, to determine the progress of the crack with respect to time. An accelerometer was used to detect the stress-waves released and the relative energy involved in the fracture process. These tests were run on alloy 24,25 and 26 in the peak strength (30 min at room temperature) and in the overaged condition (1000 min at 125°C). Only the peak strength condition gave useable results. The overaged lower strength specimens buckled and tore.

The first tests on the larger instrumented specimens was made on peak aged alloy 24 at a crosshead speed of 0.039 in/min. The load versus

time record for the tests is given in Fig. 7. The fracture surface did not show a transition, so the crosshead speed was increased to 0.39 in/min. Specimens of alloy 24 and 25 tested at this crosshead speed showed a fracture surface transition, while specimens of alloy 26 showed patches of dull and bright in the region where only bright was found on the former specimens. A comparison of the COD and load versus time records (Figs. 8, 9, 11, 12 and 14 to 17) show that a substantial amount of slow crack growth had occurred by the time the maximum load occurred at the point of crack instability (pop-in). At this point the crack jumped across the specimen in a catastrophic manner. The relative extension of the crack through the specimen (a/w) at instability, as determined by COD records, corresponded to the measured point of transition on the fracture surface. For the alloy 26 specimens the bright areas occurred at the positions expected from the appropriate COD pop-ins.

The stress intensity factor (K) corresponding to the inititation of fast crack growth was determined from instrumented fracture tests to be approximately 60 ksi $\sqrt{\text{in}}$. At the lower crosshead speed of 0.039 in/min the highest stress intensity reached was 57 ksi $\sqrt{\text{in}}$. This points out that the transition is one where a marginal increase in stress intensity causes a change in the fracture mode. The stress intensity value of 60 ksi $\sqrt{\text{in}}$ was in close agreement with the values observed at the points of instability for alloy 26, (Tables 9 and 10). The fact that there is a correlation between the point of maximum load and fracture transition (Alloy 24 and 25) was used to recalculate stress intensity values for the routine fracture tests. These values tend to be higher than the values obtained with instrumented specimens and apparently the stress intensity associated with instability increases with zinc content. The recalculated values had a good

deal more scatter than the directly measured values. They are believed to be less reliable indicators of notch toughness.

In order to find the relative amount of plastic deformation associated with the slow and fast-crack growth processes a small fracture specimen was electropolished, pulled, then the slip band density surveyed along the crack. This survey showed that slip band density was roughly twice as high in the slow-crack growth region as in the fast-crack growth region. This indicates there was a reduction in the plastic zone size when the crack is on the fast crack growth side of the transition.

b. The Effect of Increasing Zinc Content and Overaging of The Fast-Crack Growth Process

The zinc content, up to about 25% zinc in the Al-Zn alloys aged to peak strength promotes intergranular fracture. (The yield strength of these alloys in the peak strength condition increases linearly with increasing the atomic percent zinc at up to 25 percent due to the increased volume fraction of precipitate.) At this concentration intergranular fracture is most pronounced; fast-crack growth is most easily induced. Further increases in zinc content cause little increase in yield strength but produce a widening of the grain-boundary regions which appears to inhibit the fast-crack growth process. The wider grain-boundary regions may be preventing stress intensity from reaching the level necessary for fast-crack growth. Overaging seems to have the same effect of increasing the width of the grain-boundary region, equalizing the strength of the grain and the grain-boundaries, and thus promoting more ductile behavior.

c. Fractography of Slow and Fast-Crack Growth

The complete fracture surface of a specimen showing a transition will be used to illustrate the most prominent features of the crack growth

processes found in this investigation. In Figs. 47 and 48 there is a sequence of fractographs covering an entire fracture specimen of alloy 24 in the peak strength condition. The crack propagated from left to right in Fig. 47(a) and from right to left in Fig. 48(a). (The specimen had been cut into two pieces in order to place it in the scanning electron microscope.) The series of fractographs in Figs. 47(b) to (d) (a sequence of increasing magnification) shows the fatigue to intergranular crack transition. The fatigue crack for this and other small fracture specimens was grown in the "as rolled" condition and the fatigue failure mode was transgranular.* The main feature of this fatigue to intergranular crack transition is its short length. Apparently the transgranular fatigue crack extended only partly through the last grain to be cracked during fatigue. At this point the crack changed and ran vertically to the closest grain-boundary, (Fig. 47c). The change in crack direction seemed most likely to have occurred with the application of the fracture load, the path followed being one of easy propagation influenced by local conditions. Once the crack reached the grain-boundary no deviation from the grain-boundary path could be found thereafter. The fracture surface up to the point transition is represented by the series of fractographic in Figs. 47(e) to (g). The light incident on the rough surface in the slow-crack growth region was scattered, accounting for the dull appearance. The fast-crack growth surfaces shown in Fig. 48 are almost optically flat (Fig. 48b), accounting for the bright appearance of this region. Figures 48(c) to (e)

---

*For the larger fracture specimens the crack was grown in the heat treated condition and failure was for the most part intergranular.

have the same features one would expect to find in cleavage, such as the changing of the fracture plane (cleavage rivers; Fig. 48(b) and (d).) The fast-crack growth region resembles in appearance, the intergranular cleavage in iron found by Low.[34] However fcc materials are not known to cleave, therefore until it can be proved that the fast-crack growth process is cleavage another (shear) mechanism will be presumed to operate.

The effects of overaging can be seen in Fig. 44. Fractographs (a) and (b) were taken from the fast-crack growth region of a specimen aged to peak strength, while fractographs (c) and (d) were taken from an overaged specimen in the same relative position (a/w) along the fracture surface. In the first case failure was by the fast-crack growth process, but in the second it was by microvoid coalsecence (as it was for all slow-crack growths failures). There was a varying amount of transgranular fracture associated with overaging ranging from zero in the peaks strength condition to almost 100% in the fully overage condition. This is shown in Figs. 43, 52 and 53. The transgranular patch of material left at the grain boundary intersection shown in Figs. 52(e) and (f) appears as though it may be a colony of zinc that has grown out from a grain-boundary intersection, as in Fig. 30(b). Figures 52(c) and (d) show how the grain-boundary has exuded during fracture. The height of the exuded material was greater in the overaged condition (Figs. 52(c) and (d)) than in the peak strength condition (Figs. 45(c) and (d)), as would be expected from the relative widths of the grain-boundary regions.

Alloys 22 and 23 tended to fail intergranularly, but the fracture was always of mixed mode. Intergranular fracture became more pronounced with increasing strength and zinc content, as shown in Figs. 41 and 42. Transgranular fracture in these alloys took place by shear rupture, as was

the case of alloy 24 in the overaged condition. Alloys 25 and 26 with higher zinc contents than alloy 24 showed generally the same fractographic features as the latter. Overaging, with its associated increased amount of transgranular fracture occurred at a more rapid rate in alloys having higher zinc contents.

d. Slow-Crack Growth

In the introduction it was mentioned that one might expect to find that an intergranular crack would grow discontinuously. A careful look at the stress wave patterns, Figs. 9, 12, 15, 17, 23 and 25 shows that during slow-crack growth the crack appears to grow discontinuously from one grain boundary node to another. The average crack growth distance between the minor stress-waves is on the order of 0.001 in. This comes from considering the amount of crack growth between two points on the COD vs time record and correlating this to the number of stress-waves emitted during this time interval. If this procedure is carried out for several points during each test, then an overall picture may be seen. The grain size of these specimens is on the order of 0.010 in. (250μ) or about an order of magnitude larger than the average distance between minor stress waves. The specimens are about twelve grains thick, and it appears that the minor stress waves are representative of individual jumps forward of the crack from one grain node to another across the thickness of the specimen. It may be expected that the crack would grow one grain at a time until only a few grains facets remain to be fractured. Here the crack may be expected to jump across the remaining grain facets in one more or less continuous step. If this is the case, the stress-wave pattern for slow-crack growth should show two superimposed patterns; one for individual jumps and one for the jump of the crack front. There should be approximately 10 or less small stress waves between the slightly larger stress waves representing

the crack front jump.. The actual stress-wave patterns do in fact have a series of small waves in between slightly larger waves. This pattern is not repeated exactly from one period to the next but a variation is conceivable because of local conditions along the grain boundary fracture path.

e. Stress Intensity for Slow-Crack Growth

The stress intensity for initiation of the slow-crack growth process of the aluminum zinc alloys in the peak strength conditions is considerably less than the value needed for the fast-crack growth process (~ 60 ksi$\sqrt{in}$). A reasonable criterion for the initiation of the slow-crack growth process is the stress intensity at the first stress-wave of the discontinuous crack growth pattern. When there are stress-waves preceding the steady state slow-crack growth pattern a different criterion may be employed. The criterion in this case is to use the stress intensity at the first stress-wave with an amplitude equal to that expected if there were a slow crack growth pattern (~ 0.01 g acceleration). The stress intensity for slow crack growth of alloy 24 in the peak strength condition is in the range of 12 to 17 ksi $\sqrt{in}$. This value increases somewhat with zinc content for alloy 25 and 26.

The difference between this intergranular slow-crack growth instability and normal instabilities found in transgranular fracture preceding catastropic failure is important. The normal instabilities associated with the first stress-waves in a fracture tests are generally not of a critical nature. These instabilities may, in the case of a plain stress specimen, be due to plain strain pop-in before plain stress or mixed mode steady state conditions prevail. Other local instabilities may cause stress-waves, but the main feature of these events is that they are not "critical" events. By critical, it is meant that under constant load conditions, the

specimen will fail within a finite time. Generally speaking, the stress intensities associated with local instabilities giving rise to the first stress waves will not be of sufficient magnitude to cause failure under constant load conditions. This is because most materials do not have a preferential easy path of fracture, and the crack will blunt through plastic deformation. In the case of intergranular fracture, however, once the crack in the grain-boundary there is no adequate mechanism for crack blunting. Thus crack may be expected to grow under constant load conditions. The stress intensity necessary for the initiation of slow-crack growth should be a critical stress intensity. In the case of alloy 24 (peak strength) this is of the order of 12 to 17 ksi $\sqrt{\text{in.}}$

Two tests of the above criterion for alloy 24 in the peaks strength condition were made. The first was to calculate the stress intensity expected for slow-crack growth from a plastic energy dissipation model and the second test of this criterion was to subject a specimen to constant load conditions.

In order to calculate the stress intensity factor for slow-crack growth consider that the energy is dissipated by the elongation of a series of parallel tensile specimens whose gage length is the width of the plastic zone. It is assumed that the fracture process is controlled by the plastic energy dissipated in a region confined to one grain on either side of the fracture surface. The plastic zone width in this case is two grains or about 0.02 in. The stress intensity factor is related to the work per unit area W/A,

$$K = (E\, W/A)^{1/2} \qquad (1)$$

where E = modulus of elasticity = 10.4×10^6 psi. The work per unit area

$$W/A = 2r_p \int_0^{\epsilon_f} \sigma_{ys}\, d\epsilon \approx 2r_p\, \sigma_{ys}\, \epsilon_f, \qquad (2)$$

where $2r_p$ = width of plastic zone = 0.02 in.

σ_{ys} = yield strength of the material = 46×10^3 psi

ϵ_f = elongation at fracture = 0.04.

Combining (1) and (2) we have

$$K = (E\, 2r_p\, \sigma_{ys}\, \epsilon_f)^{1/2}, \qquad (3)$$

and using the values for the parameters given above

$$K = 19.5 \text{ ksi}\sqrt{\text{in}}$$

From the close agreement between the calculated and observed stress intensities it consistent to consider the first significant stress-wave to be associated with the initiation of the slow-crack growth process.

To test the criterion for slow-crack growth and the relative value of the stress intensity factor associated with the process a constant load test was run. A constant load equivalent to a stress intensity of 11.4 ksi$\sqrt{\text{in}}$ was first applied to a small fracture specimen for a period of 33 min. There was no detectable crack growth during this length of time. A constant load equivalent to a stress intensity of 13.7 ksi$\sqrt{\text{in}}$ was then applied. The crack grew to failure in a period of 9 min.

The above described constant load test seems to justify the criterion for slow crack growth. An argument could be made for stress corrosion because of the fact that the fracture tests were run in air which contains water. It is thought however that the slow-crack growth process is not one of stress corrosion but rather a mechanical process. This is because of the similarity of stress intensity values between constant load, con-

stant cross-head speed conditions, and the plastic energy dissipation calculations.

2. Comparison of Fracture in Al-Zn and Al-Ag Alloys

The kinetics of the precipitation process in the Al-Ag alloys is considerably slower than in the Al-Zn alloys. The peak strengths of these alloys required aging from 50 min (at 225°C) for alloy 30 to 1000 min (at 225°C) for alloy 27. In the solution treated condition failure of these alloys was by transgranular shear. Aging of Al-Ag alloys to peak strength caused failure to become intergranular, but to a degree that varied with the silver content. At about 20% silver (alloy 29), fracture in the fully aged condition was completely intergranular. The intergranular fracture of Al-Ag differs from that in the Al-Zn alloys in that flat boundary failures characteristic of the fast-crack growth process in Al-Zn alloys were never found. The crack growth was always by microvoid coalesence (Figs. 63,64,67 and 68). This may be due to the fact that the effective grain-boundary width (grain-boundary plus precipitate-free zone) is greater in these alloys. Sedriks et al.[35] found that in the case of stress corrosion cracking the time to failure was inversely related to the precipitate-free zone width. While there is no direct comparison that can be made, it may well be that the wider effective grain-boundary region allows better adjustment of high local stresses. Overaging, which causes widening of the grain-boundary regions and softening of the grains, further enhances local strain accommodation until transgranular fracture prevails. The strength of the grains approaching that of the grain-boundary region.

In general the Al-Ag alloys are tougher than the Ag-Zn alloys because the plastic deformation is more homogeneous. This may be seen by

comparing distribution of slip lines in neighboring grains, Figs. 76(a) and 78(a). The plastic zone size of the Al-Zn alloy in peak aged and overaged condition (Fig. 74) may be compared to that found in alloy 29 in the peaks aged condition (Fig. 77). (Scanning electron micrographs of the first plastic zone in Fig. 74(a) are shown in Fig. 74.) The calculated plastic zone size for the overaged Al-Zn and the peak aged Al-Ag specimens is the same (0.35 in.) and nearly equal to the measured size for peak aged Al-Ag alloy (0.37 1/2 in.).* The micrographs show that the deformation is more uniformly distributed in the case of Al-Ag alloys and as a result these alloys should be expected to be much tougher. (Note: the grain rotation in Fig. 75(c) and the crack at the interface of the plastic zone in Figs. 75(a) and (e).)

Impact tests of small fracture samples, similar to those described in Appendix II for Al-Zn alloys, indicate that Al-Ag alloys are tougher than the Al-Zn alloys. The energy to fracture a sample of peak aged Al-Zn alloy 24 is 2 ft. lbs. as compared to 11 ft. lbs. for peak aged alloy 29. (The energy to fracture the same size sample of commerical 7075-T6 is 4 ft. lbs.) The peak aged alloy 24 failed by the fast-crack growth process and there was little energy absorbed in crack progagtion. In the peak aged alloy 29, there was a large amount of energy absorbed in crack propagation. The high strain rate associated impact conditions has caused the crack to propagate in a mixed intergranular and transgranular mode for the reasons mentioned in Appendix II. In this case the percentage of transgranular character is much greater than for the Al-Zn alloys as shown in Fig. 65. The transgranular crack growth was by shear rupture, as

---

* The plastic zone size is calculated assuming plain stress conditions and using the relationship $2r_p = 1/\pi\ (K/\sigma_{ys})^2$ = width of plastic zone.[36,37]

shown in Figs. 65 (b) to (d). This behavior is in keeping with the idea that there is not as much difference between the grain-boundary and transgranular fracture paths in Al-Ag alloys as in the Al-Zn alloys.

IV. CONCLUSIONS

1. There are two basic intergranular fracture processes, slow-crack growth which takes place by microvoid coalescence and fast-crack growth which takes place through a low energy fracture process. Of the two series of alloys studied, only aluminum-zinc alloys with 25% or more zinc aged to near peak strength have been found to fail by the fast-crack growth process. In general, fast-crack growth only occurs under the conditions where there are narrow grain-boundary regions, relatively high strain rate and/or low temperature. The stress intensity for the initiation of fast-crack growth is several times that for slow-crack growth.

2. In cases where intergranular fast-crack growth occurs, it is generally preceded by slow-crack growth. The transition from slow-crack growth to fast-crack growth can be seen from the change in reflectivity of the fracture surface. The surface of slow-crack growth region is dull while that for fast-crack growth is bright. With the onset of fast-crack growth, the plastic zone decreases in size.

3. Slow-crack growth takes place discontinuously, the crack jumping from one grain-boundary node to another. The slow-crack growth process in specimens of Al-Zn alloys with 25% or more Zn, aged to near peak strength, can lead to failure under a constant load sufficient to initiate the process. This is probably because once the crack is running along the grain-boundary there is no mechanism to blunt it. The calculated stress intensity factor based on the plastic energy dissipated within a region of one grain on either side of the fracture surface is consistent with the measured value.

4. The initiation of slow-crack growth can be detected by the first stress-waves of the discontinuous crack growth pattern. Normally the first stress-waves do not signify a process leading to failure.

5. The observed plastic zone size appears to be in good agreement with calculated values in the case of aluminum-silver alloys but not always in the case of aluminum-zinc alloys.

6. The shear dimple spacing appears to be of the order of the macroscopic slip line spacing.

ACKNOWLEDGEMENTS

The author wishes to express his appreciation to: Professor Earl R. Parker, Mr. William W. Gerberich, and Professor Victor F. Zackay, Department of Materials Science, University of California, for their advice and encouragement; the staff of the Inorganic Materials Research Division of the Lawrence Radiation Laboratory for their support; Professor Thomas L. Hayes of the Donner Laboratories, Lawrence Radiation Laboratory and the Japan Electron Optics Laboratory Co., Ltd. (JEOLCO Inc., U.S.A.) for the use of their respective scanning electron microscopes.

This work was done under the auspices of the United States Atomic Energy Commission through the Inorganic Materials Research Division of the Lawrence Radiation Laboratory

REFERENCES

1. A. Kelly and R. B. Nicholson, Precipitation Hardening, Progress in Material Science, 10 (1963) 149.

2. D. A. Ryder and A. C. Smale, Fracture in Solids, D. C. Drucker and J. J. Gilman, eds., (John Wiley and Sons, New York, 1965), p. 237.

3. G. Thomas, Electron Microscopy and Strength of Crystals, Gareth Thomas and Jack Washburn, eds., (John Wiley and Sons, New York, 1963), p. 793.

4. P. C. Varley, M. K. B. Day and A. Sendorek, J. Inst. Metals, 86 (1957-58) 337.

5. A. H. Geisler, Phase Transformation in Solids, R. Smolvchowski, J. E. Mayer and W. A. Weyl, eds., (John Wiley and Sons, New York, 1951), p. 387.

6. G. Thomas, J. Inst. Metals, 89 (1960-61) 287.

7. H. C. Chang and N. J. Grant, Trans. AIME, 206 (1956) 544.

8. N. J. Grant, Fracture, B. L. Averbach, D. K. Felbeck, G. T. Hahn and D. A. Thomas, eds., (The M.I.T. Press, Cambridge, Mass., 1959), p. 562.

9. R. C. Gifkins, ibid.

10. G. Thomas and J. Nutting, J. Inst. of Metals, 88 (1959-60) 81.

11. P. J. E. Forsyth and D. A. Ryder, Metallurgia 63 (1961) 117.

12. T. E. Orange, Fracture Toughness of Wide 2014-T6 Aluminum Sheet at 320°F (NASA TN D-4017), 1967.

13. S. H. Smith, T. R. Porter and W. D. Sump, Fatigue Crack Propagation and Fracture Toughness Characteristics of 7079 Aluminum Alloy Sheets and Plates in Three Aged Conditions, (NASA CR-99), 1968.

14. J. G. Kaufman and M. Holt, Fracture Characteristics of Aluminum Alloys, Alcoa Research Laboratories Technical Paper, 18, 1965.

15. A. Phillips, V. Kerlings, and B. W. Whiteson, Electron Fractography Handbook, (ML-TDR-64-416), 1965.

16. Y. Katz, P. L. Key, and E. R. Parker, Dimensionless Fracture Toughness Parameters, (UCRL-17895), 1968.

17. J. E. Srawley and B. Gross, Stress Intensity Factors for Crackline Loaded Edge-Crack Specimen, (NASA TN D-3820), 1966.

18. W. F. Brown, Jr. and J. E. Srawley, Plain Strain Crack Toughness Testing of High Strength Metallic Materials, ASTM, STP No. 410, (1966).

19. C. E. Hartbower, W. W. Gerberich, P. P. Crimmins, Monitoring Subcritical Crack Growth by an Acoustic Technique, Welding Journal Research Supplement, January 1968, p. 1.

20. C. E. Hartbower, W. W. Gerberich, and H. Liebowitz, Eng. Fract. Mech. 1 (1968) 291.

21. W. W. Gerberich and C. E. Hartbower, Int. J. Fracture Mechanics, 3 (1967) 185.

22. R. B. Nicholson, G. Thomas, and J. Nutting, Brit. J. Appl. Phys., 9 (1958) 25.

23. D. McLachlan, Jr., Applied Optics, 3 (1964) 1009.

24. I. J. Polmear, J. Inst. Metals, 86 (1957-58) 113.

25. R. D. Garwood and A. L. Davies, J. Inst. Metals, 88 (1959-60) 311.

26. J. M. Seeman and R. A. Dodd, Trans. AIME, 239 (1967) 748.

27. W. L. Fink and D. W. Smith, Trans. AIME, 124 (1938) 223.

28. K. B. Rundman and J. E. Hilliard, Acta Met. 15 (1967) 1025.

29. K. Krishna Rao, L. E. Katz, and H. Herman, Mat. Science and Eng., 1 (1967) 263.

30. J. A. Hren and G. Thomas, Trans. AIME, 227 (1963) 308.

31. G. Thomas, Phil. Mag. 4 (1959) 1213.

32. R. N. Stevens, Trans. AIME, 236 (1966) 1762.

33. P. J. E. Forsyth and D. A. Ryder, Metallurgia, 63 (1961) 117.

34. J. R. Low, Jr., Fracture, B. L. Averbach, D. K. Felbech, G. T. Hahn, and D. A. Thomas, eds. (The M.I.T. Press, Cambridge, Mass.) 1959), p. 68.

35. A. J. Sedriks, P. W. Slattery and E. N. Pugh, Precipitate Free Zones and Stress Corrosion Cracking in a Ternary Al-Zn-Mg Alloy, to be published in Trans. ASM.

36. G. R. Iwin, Trans. ASME, J. Basic Eng., 82 (1960) 417.

37. G. R. Irwin, Plastic Zone Near a Crack and Fracture Toughness, Proc. Seventh Sagamore Ordnance Materials Conference, Syracuse University Research Institute, 1960, p. IV-63.

APPENDIX I

Table 15. Tensile Properties of Zinc and Silver

	t, in.	Condition	Test Temp. °C	$\dot{\epsilon}$, 1/min.	Elong. %	Y.S., ksi	U.T.S., ksi	n
	Zinc							
423	.125	Annealed	LN_2	.0039	1.0	2.6	—	—
424	.125	As Rolled	LN_2	.0039	—	6.9	—	—
422	.125	Annealed	LN_2	.39	2.0	1.6	—	—
440	.125	Annealed	RT	.0039	18	4.1	4.3	.30
439	.125	Annealed	RT	.39	5	4.9	6.3	.24
430	.125	Annealed	180°C	.39	55	3.3	4.0	.09
	Silver							
425	.0625	Annealed	LN_2	.39	120	4.7	35.5	.89
426	.0625	Annealed	LN_2	3.9	124	5.2	36.6	.88
441	.0625	Annealed	RT	.39	70	3.4	22.2	.70
442	.0625	Annealed	RT	3.9	72	7.9	23.4	.57

APPENDIX II

The Effect of High Strain Rates and Low Temperature on the Fracture Process in Alloy 24

It was mentioned in the discussion that, at a low crosshead speed of 0.039 in./min, the large peak aged fracture specimens of alloy 24 did not show a slow-crack to fast-crack growth transition whereas a specimen pulled at 0.39 in./min did. The effect of a further increase in strain rate was investigated by pulling a small fracture specimen under impact conditions. This was accomplished by attaching the specimen at one end to a Charpy hammer and at the other end to a claw which would catch the Charpy anvil as the hammer came by on the downward swing. The entire fracture surface resulting from this test (Fig. 55) showed bright appearing intergranular fracture with traces of transgranular shear rupture [(b) and (c)]. The fractographic appearance of the bright intergranular fracture surfaces was the same as found for the fast-crack growth process. Possibly the small amounts of transgranular shear rupture were caused from dynamic loading effects.

A small fracture specimen was pulsed at liquid nitrogen temperature at a crosshead speed of 0.039 in./min (same as used in the routine tests) to see if the lower temperature might also decrease the amount of slow-crack growth. The fracture surface from this test showed only the fast-crack growth mode of intergranular failure (Fig. 54).

The effect of decreasing the test temperature or increasing the strain rate may be to increase the strength of the grain-boundary and/or precipitate-free zone. The transition from slow-crack to fast-crack growth is one requiring only a small increase in stress intensity which could be allowed by a relative increase in strength of the grain-boundary.

The fact that some transgranular fracture was observed at high strain rates would also point to this type of a mechanism. However, a good deal more work is needed in order to determine what mechanism(s) are controlling.

APPENDIX III

Fatigue of Alloy 24 Aged to Peak Strength

A metallographic fatigue study was carried out on alloy 24 in the peak aged condition in order to obtain a more complete picture of the crack growth process. A small fracture sample was electropolished and then tension-tension fatigued at 30 Hz and K = 12.5 ksi $\sqrt{\text{in.}}$, first for 100 cycles [Fig. 69 (b)] then for 2500 cycles (Fig. 70). After fatiguing at 30 Hz, the specimen was pullsed in two stages to near failure (Figs. 71-73).

Before fatiguing, the crack tip was at a grain-boundary [Fig. 69 (a)]. The crack grew on fatiguing first along the grain boundary, propagated transgranularly. At the next grain-boundary the crack changed mode and followed a grain boundary path for a number of grains then changed back to the transgranular mode (about half way across, Fig. 70, in which the notch is on the left). The fatigue crack ended on the right side of Fig. 70. At this point the crack had branched, following some transgranular, and some intergranular paths. When a non-cyclic load was applied at this point, only the intergranular crack opened [Fig. 71(a)]. As the load was increased up to a predetermined value and then relaxed, the crack grew intergranularly, then stopped after producing a small plastic zone (Fig. 71(b) and 72). On reapplication of the load the crack continued to grow intergranularly producing another small plastic zone. The crack stopped on the relaxation of the load, as shown in Fig. 73. This sample is also shown in Fig. 74 (a) where the plastic zones show clearly. The conclusion to be drawn from this study is that crack growth under both high K level tension-tension fatigue and constant

crosshead speed conditions have several features in common. Mainly, both conditions favor intergranular crack growth, and the appearance of the crack at the surface is influenced by these several factors. The change in fracture from intergranular to transgranular mode may be due to a low resolved shear stress on the active grain boundary preventing further crack propagation along that boundary. It is also possible that the neighboring interior grains effect the fracture path at the surface.

APPENDIX IV

A Comparison of Scanning Electron Microscopy to Conventional Techniques

A. Introduction

The scanning electron microscope (SEM) has existed in concept for sometime but only recently has the instrument been developed to such an extent that it has become a valuable research tool. Investigators are still exploring the uses of the scanning electron microscope in many fields of research. The following comparison of the SEM to conventional techniques is aimed at illustrating some of the benefits of this technique over others.

B. Metallography

Two comparisons are presented in the text; optical micrographs of aluminum, 25.7% zinc in the overaged correlation (10,000 min at 125°C) are given in Figs. 30 (c) and 31 (a). Scanning electron micrographs for a similar area of the same specimen are given in Figs. 31 (b)-(g). A corresponding comparison can be made for a specimen of aluminum, 20% silver in the same overaged condition [Figs. 38 (a) to (c) versus Figs. 38 (d) and (e)]. The general quality of the micrographs from both techniques is comparable. However, the additional depth of field of the SEM and 45° mounting of the specimen gives the investigator information on the relative height of the surface features (i.e. in the grain-boundary and precipitate in this case). This information in many instances, is difficult to obtain optically. In addition, the magnification is slightly higher than the optical microscope.

C. Fractography

The extreme depth of focus of the SEM can be used to full advantage for intergranular fractography. Replica fractography techniques are difficult to use because of the surface roughness. SEM can be compared to scanning optical microscopy, both techniques having a large depth of field. A direct comparison is given in Figs. 46 (a) and (b). (Scanning Optical Micrograph) and Figs. 46 (c) (SEM). The scanning optical technique does not have the clarity and contrast of the SEM. Detail that is present optically would be difficult to interpret without the SEM for reference. The most notable qualities of SEM here are the extended range of magnification and the fidelity of perspective. Standard metallographic techniques do not have the depth of field and the perspective to correctly interpret the fractography of single grain facets. Examples of the added information gained by the SEM over metallographic techniques are given in Figs. 50 and 51.

LEGAL NOTICE

TECHNICAL INFORMATION DIVISION
LAWRENCE RADIATION LABORATORY
UNIVERSITY OF CALIFORNIA
BERKELEY, CALIFORNIA 94720